Wang, Gang, Ph.D., April, 2006 NUCLEAR PHYSICS

CORRELATIONS RELATIVE TO THE REACTION PLANE AT THE RELATIVISTIC HEAVY ION COLLIDER BASED ON TRANSVERSE DEFLECTION OF SPECTATOR NEUTRONS (122 pp.)

Director of Dissertation: Declan Keane

Modern physics is challenged by the puzzle of quark confinement in a strongly interacting system. High-energy heavy-ion collisions can experimentally provide the high energy density required to generate Quark-Gluon Plasma (QGP), a deconfined state of quark matter. For this purpose, the Relativistic Heavy Ion Collider (RHIC) at Brookhaven National Laboratory has been constructed and is currently taking data. Anisotropic flow, an anisotropy of the azimuthal distribution of particles with respect to the reaction plane, sheds light on the early partonic system and is not distorted by the post-partonic stages of the collision. Non-flow effects (azimuthal correlations not related to the reaction plane orientation) are difficult to remove from the analysis, and can lead us astray from the true interpretation of anisotropic flow. To reduce the sensitivity of our analysis to non-flow effects, we aim to reconstruct the reaction plane from the sideward deflection of spectator neutrons detected by the Zero Degree Calorimeter (ZDC). It can be shown that the large rapidity gap between the spectator neutrons used to establish the reaction plane and the rapidity region of physics interest eliminates all of the known sources of non-flow correlations. In this project, we upgrade the ZDC to make it position-sensitive in the transverse plane, and utilize the spatial distribution of neutral fragments of the incident beams to determine the reaction plane.

The 2004 and 2005 runs of RHIC have provided sufficient statistics to carry out a systematic analysis of azimuthal anisotropies as a function of observables like collision system (Au+Au and Cu+Cu), beam energy (62 GeV and 200GeV), impact parameter (centrality), particle type, etc.

Directed flow is quantified by the first harmonic (v_1) in the Fourier expansion of the particle's azimuthal distribution with respect to the reaction plane, and elliptic flow, by the second harmonic (v_2). They carry information on the very early stages of the collision. For example, the variation of directed flow with rapidity in the central rapidity region is of special interest because it might reveal a signature of a possible QGP phase. This flow study using the 1st-order reaction plane (the reaction plane determined by directed flow) reconstructed using the ZDC-SMD has minimal, if any, influence from non-flow effects or effects from flow fluctuations. The experimental results can be compared with different theoretical model predictions such as AMPT, RQMD, UrQMD and hydrodynamic models. We can also use our flow results to test the hypothesis of limiting fragmentation - the effect whereby particle emission as a function of rapidity in the vicinity of beam rapidity appears unchanged over a wide range of beam energy.

CORRELATIONS RELATIVE TO THE REACTION PLANE AT THE RELATIVISTIC HEAVY ION COLLIDER BASED ON TRANSVERSE DEFLECTION OF SPECTATOR NEUTRONS

A dissertation submitted to
Kent State University in partial
fulfillment of the requirements for the
degree of Doctor of Philosophy

by

Gang Wang

April, 2006

Dissertation written by

Gang Wang

B.S., Harbin Institute of Technology, 1999

M.S., Harbin Institute of Technology, 2001

Ph.D., Kent State University, 2006

Approved by

_____ , Chair, Doctoral Dissertation Committee

_____ , Members, Doctoral Dissertation Committee

_____ ,

_____ ,

_____ ,

Accepted by

_____ , Chair, Department of Physics

_____ , Dean, College of Arts and Sciences

Table of Contents

List of Figures vii

List of Tables x

Acknowledgements xi

1 **Introduction** 1

1.1 Quark-Gluon Plasma 1

1.2 Relativistic heavy-ion collisions 2

1.3 Probes for QGP 4

1.3.1 Direct photons and dileptons 4

1.3.2 Thermodynamic variables 4

1.3.3 Charmonium suppression 4

1.3.4 Strangeness enhancement 5

1.3.5 The Hanbury-Brown-Twiss effect 5

1.3.6 High p_t probes 5

1.3.7 Anisotropic flow 6

2 **Anisotropic Flow** 7

2.1 Introduction 7

2.2 Flow components 8

2.2.1 Directed flow 10

2.2.2 Elliptic flow 13

2.3 Flow analysis with event plane 16

2.4 Non-flow effects 16

3 **STAR Experiment** 17

3.1 The layout of the STAR experiment 17

3.2 STAR main TPC 19

3.3 STAR forward TPCs 20

3.4 STAR ZDCs 21

4 **Upgrade of STAR ZDC** 23

4.1 Physics motivation 23

4.1.1 Flow 23

4.1.2 Strange quark matter 25

4.1.3 Ultra-peripheral collisions 26

4.1.4 Spin physics 27

4.2 Simulations 28

4.2.1 Flow 28

4.2.2 Strangelets 30

4.3 Hardware configuration 31

4.4 Impact on STAR 33

5 **Calibration and Performance of ZDC-SMD** 35

5.1 Pedestal subtraction 35

5.2 Gain correction 36

5.2.1 Cosmic ray tests 36

5.2.2 Exponential fit 38

5.3 Location of $p_t = 0$ point 39

5.4 Energy deposition 40

5.5 Beam position sensitivity 42

6 **Estimation of the Reaction Plane** 44

6.1 Estimation of the reaction plane 44

6.1.1 Track-based and hit-based 44

6.1.2 Event plane distribution 46

6.1.3 Event plane resolution 49

6.2 The 1st-order event plane in flow analysis 51

6.2.1 Terms for east, west, and for vertical and horizontal directions in the transverse plane 51

6.2.2 Correction to sub-event plane resolution 52

6.2.3 Acceptance correction 53

6.2.4 Granularity correction in hit-based detectors 55

6.2.5 Before and after corrections 56

6.2.6 Robust test of flow analysis with the ZDC-SMD 57

7 **Flow Results I: Directed Flow** 59

7.1 Introduction of transport models 59

7.1.1 RQMD 59

7.1.2 UrQMD 60

7.1.3 AMPT 60

7.2 Model calculations and previous measurements 61

7.3 62 GeV Au +Au 62

7.4 200 GeV Au +Au 74

7.5 200 GeV Cu +Cu 85

8 **Flow Results II: Elliptic Flow** 91

9 **Summary and Outlook** 95

References 99

A **The Quark Model** 105

B **The QCD Theory** 108

C **Kinematic Variables** 112

D **Author's Contributions to Collaborative Research** 114

E **List of Publications** 116

F **The STAR Collaboration** 121

List of Figures

1.1 Phase diagram of nuclear matter. 1

1.2 Reaction plane. 2

1.3 Space-time diagram of heavy-ion collisions. 3

2.1 Major types of azimuthal anisotropies. 8

2.2 Schematic behavior of the magnitudes of directed flow and elliptic flow as a function of the bombarding kinetic energy per nucleon in the laboratory frame. 9

2.3 Reduction of the directed flow due to phase transition. 10

2.4 Directed flow from tilted, ellipsoidally expanding fluid sources 11

2.5 RQMD prediction of “wiggle” 12

2.6 Elliptic flow as a function of impact parameter in LDL limit and Hydro limit. . . . 14

2.7 v_2 per number of constituent quark (n_q) as a function of p_t/n_q for various particle species. 15

3.1 A perspective view of the STAR detector. 17

3.2 A cutaway view of the STAR detector 2001. 18

3.3 Perspective view of the STAR Time Projection Chamber. 19

3.4 Schematic diagram of a STAR FTPC. 20

3.5 Correlation between pulse heights from the Zero Degree Calorimeters and the Central Trigger Barrel in a minimum bias trigger. 22

4.1 Flow simulation for ZDC upgrade. 29

4.2 Strangelet simulation for ZDC upgrade. 30

4.3 Diagram of the SMD with baseline ZDC modules. 31

4.4 Photo of ZDC-SMD module installed at STAR. 32

4.5 SMD layout. 33

5.1 Example of applying pedestal subtraction. 35

5.2 The signal distributions of vertical ZDC-SMD channels in a cosmic ray test. 36

5.3 A typical panel in Fig. 5.2. 37

5.4 Examplle of applying gain correction. 39

5.5 Spatial distribution of $p_t = 0$ point. 40

5.6 The energy correlation between ZDC-SMD and ZDC. 41

5.7 The relative energy resolution between the ZDC-SMD and the ZDC. 42

5.8 The beam position against time. 43

6.1 Raw distributions of the event planes from the ZDC-SMDs. 47

6.2 Distributions of the flattened event planes from the ZDC-SMDs. 48

6.3 Acceptance correction terms. 55

6.4 4 terms of $v_1(\eta)$ before and after corrections. 57

6.5 $v_1(\eta)$ comparison between the 4-term average and the full ψ analysis. 58

7.1 $v_1(\eta)$ for charged particles, for centrality 10%–70% in 62 GeV AuAu. 64

7.2 A systematic study on the dca-dependence of $v_1(\eta)$. 67

7.3 $v_1(y)$ for protons and pions in 62 GeV AuAu. 68

7.4 A systematic study on the purity-dependence of pion $v_1(\eta)$ and proton $v_1(\eta)$. . . . 69

7.5 $v_1(\eta)$ for charged particles for different centralities in 62 GeV AuAu. 70

7.6 $v_1(\eta)$ comparison between STAR and PHOBOS in Au +Au collisions at 62 GeV. . 71

7.7 $v_1(p_t)$ for charged particles measured in the main TPC and Forward TPCs in 62 GeV AuAu. 72

7.8 v_1 for charged particles as a function of impact parameter in 62 GeV AuAu. 73

7.9 $v_1(\eta)$ for charged particles for 3 centrality bins in 200 GeV AuAu. 74

7.10 $v_1(y)$ for pions from 158A GeV PbPb. 75

7.11 $v_1(y)$ for pions in 200 GeV AuAu. 76
7.12 $v_1(p_t)$ for charged particles measured in the main TPC and Forward TPCs in 200 GeV AuAu. 77
7.13 $v_1(\eta)$ for charged particles measured in the main TPC with different p_t cuts. 78
7.14 Yields of pions, (anti-)protons in 200 GeV AuAu. 79
7.15 Yield ratios between (anti-)protons and pions, and between anti-protons and protons in 200 GeV AuAu. 80
7.16 $v_1(p_t)$ for charged particles, fit with yields in 200 GeV AuAu. 81
7.17 v_1 for charged particles as a function of impact parameter in 200 GeV AuAu. . . . 83
7.18 Limiting fragmentation test. 84
7.19 $v_1(\eta)$ for charged particles, for centrality $10\% - 60\%$ in 200 GeV CuCu. 85
7.20 $v_1(p_t)$ for charged particles, for centrality $10\% - 60\%$ in 200 GeV CuCu. 87
7.21 v_1 for charged particles as a function of impact parameter in 200 GeV CuCu. . . . 88
7.22 v_1 for charged particles as a function of centrality in 200 GeV CuCu. 90
8.1 $v_2(\eta)$ for charged particles, for centrality $20\% - 70\%$ in 200 GeV AuAu. 91
8.2 $v_2(p_t)$ for charged particles measured in the main TPC, for centrality $20\% - 60\%$ in 200 GeV AuAu. 92
8.3 v_2 for charged particles as a function of centrality measured in the main TPC in 200 GeV AuAu. 93
A.1 Meson octet with $J^P = 0^-$ 106
A.2 Baryon octet with $J^P = \frac{1}{2}^+$. 106

List of Tables

6.1 The resolution of the 1st-order full event plane provided by the ZDC-SMDs. 50

7.1 Cuts used in the TPC analysis of 62 GeV Au +Au collisions. 65

7.2 The reference multiplicity and the estimated impact parameter in each centrality bin for 62 GeV Au +Au collisions. 66

7.3 Pion dv_1/dp_t versus centrality in 200 GeV Au +Au. 81

7.4 Proton dv_1/dp_t versus centrality in 200 GeV Au +Au. 82

7.5 The reference multiplicity and the estimated impact parameter in each centrality bin for 200 GeV Au +Au collisions. 82

7.6 The reference multiplicity and the estimated impact parameter in each centrality bin for 200 GeV Cu +Cu collisions. 89

A.1 The six quark flavours and their masses 105

Acknowledgements

I would like to thank my family for their encouragement. Especially, I would like to thank my wife Xiaoying Chen, for the sacrifice she's made in supporting of my Ph.D. work, for her patience and for her love.

I extend my heartfelt thanks first of all to my advisor, Dr. Declan Keane, for his tremendous help covering from the overall guidance and constant encouragement of my Ph.D. research, to making sure my presentations going well. Declan is not only an advisor in physics but also a friend and a mentor in life. Thank you! My gratitude also goes to Zhangbu Xu, Aihong Tang, Sergei Voloshin and Art Poskanzer, with whom I had stimulating discussions at numerous occasions which helped me understand the intricate details of detector techniques and flow physics in heavy ion collisions. It was a wonderful experience working with them. Special thanks to Sebastian White, Bernd Surrow and Jim Thomas for extensive technical support. Thanks are due to Nu Xu and Weiming Zhang for discussions of various physics topics.

Thanks to Yiming Liu, Weining Zhang, Lei Huo, Xiangjun Chen and many other professors in Harbin Institute of Technology for getting me started in the heavy-ion area. Also thanks to the professors in the physics department of Kent State University for the knowledge I learned during the first two years of the Ph.D. program.

Thanks to my pals for the joyful time we had together at Brookhaven National Lab. They are, for example (in no particular order), Mikhail Kopytine, Yuting Bai, Haibin Zhang, Camelia Mironov, Xin Dong, Lijuan Ruan, etc.

I would like to thank all my collaborators, there are hundreds of people who deserve acknowledgment for their part in making this study possible. Appendix F lists the STAR collaboration, whose immeasurable hard work over a decade resulted in the successful construction and operation

of the STAR detector. Not listed in Appendix F are the hundreds of technicians, engineers, and other support personnel who were vital to the outcome of the physics program.

Chapter 1

Introduction

1.1 Quark-Gluon Plasma

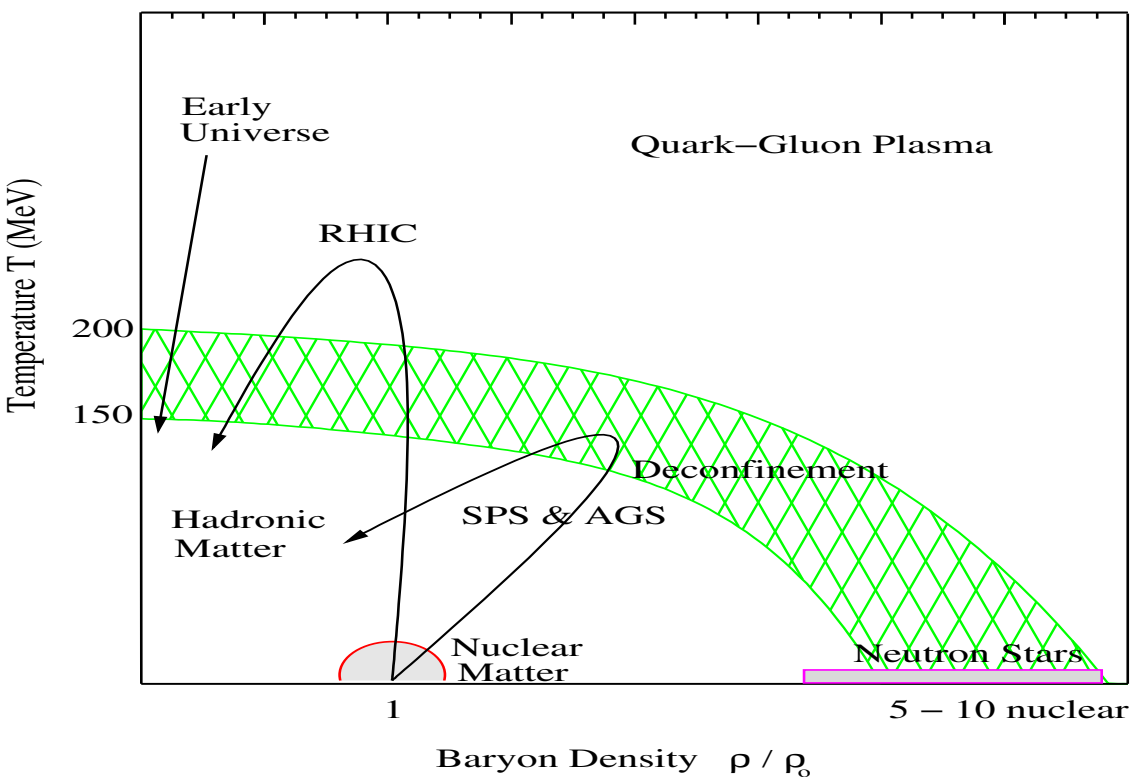

Figure 1.1: Phase diagram of nuclear matter.

Modern physics is challenged by the puzzle of quark (see Appendix A and B) confinement in a strongly interacting system[1]. Displayed in Fig.1.1 is a schematic phase diagram of nuclear matter. The behavior of nuclear matter, as a function of temperature and baryon density, is governed by its equation of state (EOS). Conventional nuclear physics focuses on the lower left portion of the diagram at low temperature and near normal nuclear matter density ρ_0. It is predicted that a

hadron-quark phase transition occurs (across the hatched band in Fig.1.1) in heavy-ion collisions at ultrarelativistic energies, and leads to the formation of a Quark-Gluon Plasma (QGP)[2], a deconfined state of quarks and gluons. QGP is believed to have existed on the order of ten micro-seconds after the Big Bang (the high temperature case in Fig.1.1), and may be present in the cores of neutron stars (the high density case in Fig.1.1).

To experimentally provide the high energy density for generating such an excited state of matter, the Relativistic Heavy-Ion Collider (RHIC) at Brookhaven National Laboratory (BNL) has been constructed and is currently taking data. RHIC provides significantly increased particle production (thousands of particles produced) over any previous machine, and opens the possibility to investigate quark matter as well as the early universe.

1.2 Relativistic heavy-ion collisions

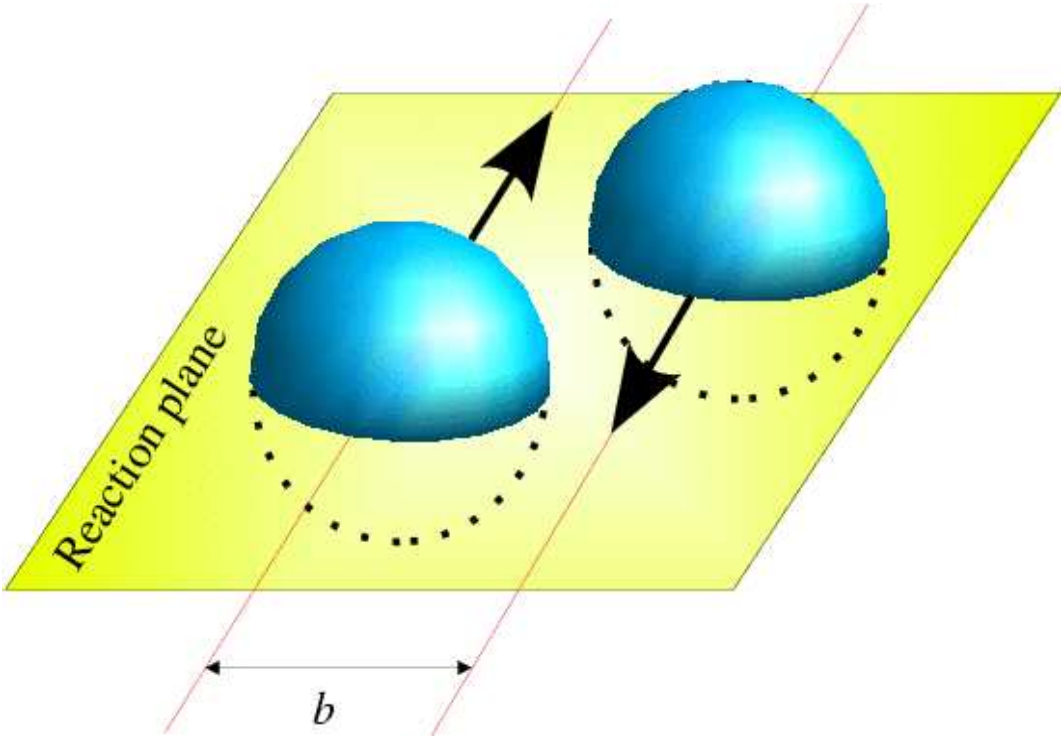

Figure 1.2: Reaction plane is defined by the initial direction of two colliding nuclei and the impact parameter (b).

RHIC collides two beams of heavy ions (such as gold ions) head-on after they are accelerated to relativistic speeds (close to the speed of light). The beams, with energy per nucleon up to 100 GeV, travel in opposite directions around RHIC's 2.4-mile "two-lane racetrack." At six intersections, the beams cross, leading to the collisions. In each heavy-ion collision event, where two ions collide at other than zero impact parameter (b) (known as a "non-central collision"), the beam direction and the impact parameter define a plane, called the reaction plane (see Fig. 1.2). Event-by-event analyses of the kind studied here need to estimate the reaction plane. The estimated reaction plane we call the event plane.

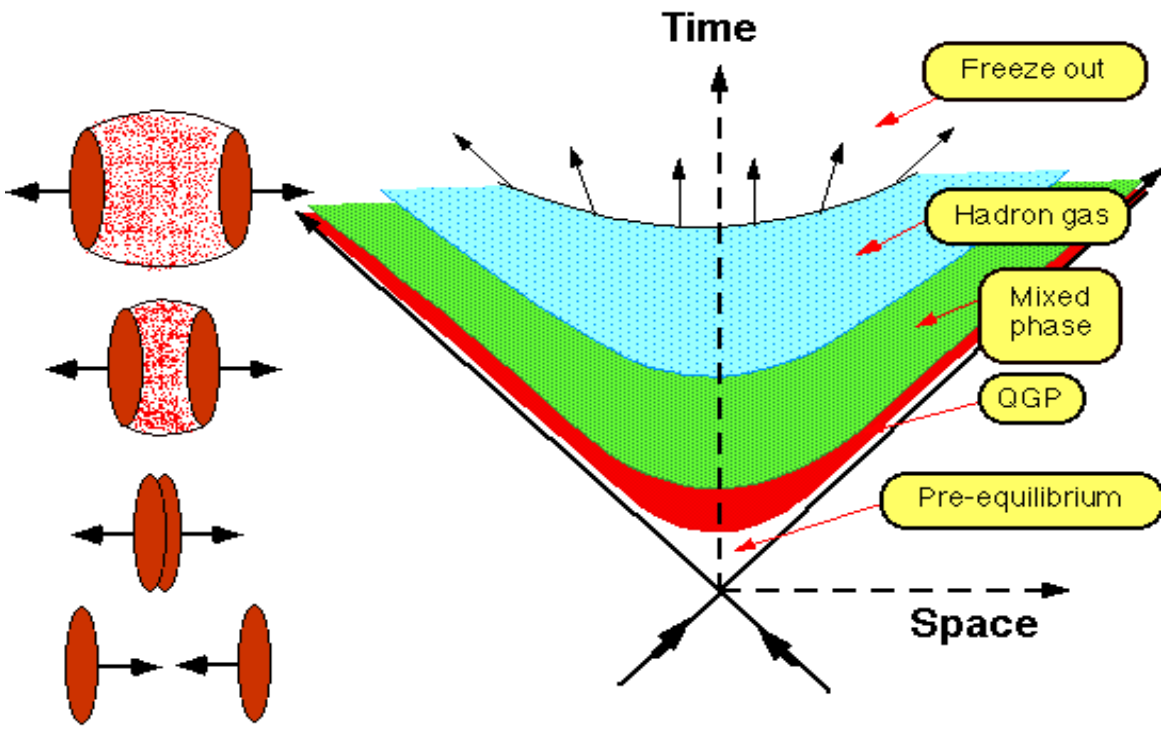

Figure 1.3: Space-time diagram of relativistic heavy-ion collisions.

Fig.1.3 shows a space-time diagram of heavy-ion collsions. The two ions first approach each other like two disks, due to the relativistic length contraction. Then they collide, smashing into and passing through one another. Some of the energy they carried before the collision is deposited

into the region of midrapidity (see Appendix C for the definition and discussion of rapidity). If conditions are right, the collision triggers a phase transition from the hadronic state of matter to a QGP. Then the partons[3] that make up the QGP quickly cool, expand and coalesce into hadrons. When the final state particles stop interacting with each other, we speak of thermal freeze-out. Experimenters can determine if a QGP was produced, not by observing it directly — its lifetime is too brief — but by looking at the information provided by the particles that shower out from the collision.

1.3 Probes for QGP

1.3.1 Direct photons and dileptons

Electromagnetic probes like direct photons and dileptons are little affected by the post-partonic stages of the collision (they only interact electromagnetically), and may provide a measure of the thermal radiation from a QGP[4, 5].

1.3.2 Thermodynamic variables

The transverse kinetic energy distribution of particles observed in relativistic heavy-ion collisions can be represented by a simple exponential function : $e^{-m_T/T}$, where T is the slope parameter, and m_T is the transverse mass (see Appendix C). Kinetic equilibration or thermal equilibrium is thought to be visible predominantly in the transverse degrees of freedom; therefore, transverse mass distributions are used to extract temperatures from the spectral slopes. A group of QGP signatures can be classified as thermodynamic variables, involving determination of the energy density ϵ, pressure P, and entropy density s of the interacting system as a function of the temperature T and baryon density ρ.

1.3.3 Charmonium suppression

The J/ψ makes a good probe for the very early stages of the collision. Its lifetime is long enough that it decays into dileptons only when far away from the collision zone. The production

of J/ψ particles in QGP is predicted to be suppressed[6], due to the effect of Debye screening[7] and quark deconfinement. Less tightly bound excited states of the $c\bar{c}$ system such as $\psi^{'}$ and χ_c are expected to dissociate more easily, and thus their yields will be suppressed even more than the J/ψ.

1.3.4 Strangeness enhancement

In hadronic reactions, the production of particles containing strange quarks is strongly suppressed as compared with the production of particles with only u and d quarks [8, 9], due to the higher mass of the $s\bar{s}$ quark pair. In relativistic heavy-ion collisions, if a QGP is formed at thermal and chemical equilibrium, the occupation probabilities of the quarks obey the Fermi-Dirac distribution, and the yields of multi-strange baryons and strange anti-baryons are predicted to be strongly enhanced as compared with a purely hadronic scenario at the same temperature[10, 11].

1.3.5 The Hanbury-Brown-Twiss effect

The interference of two particles emitted from chaotic sources was first applied by Hanbury-Brown and Twiss to measure the angular diameter of a star based on the correlation between two photons[12]. In heavy-ion collisions, the HBT measurements of particles emitted from the colliding system yield the longitudinal and transverse radii as well as the lifetime of the emitting source at the moment of thermal freeze-out[13, 14, 15, 16, 17].

1.3.6 High p_t probes

High transverse momentum (p_t) particles, emerging from hard scatterings, encounter energy loss and angular deflection while traversing and interacting with the medium produced in heavy-ion collisions. The stopping power of a QGP is predicted to be higher than that of hadronic matter[18, 19, 20], and this results in jet quenching[21, 22] – suppressions of high p_t hadron yield relative to the expectation from p+p collisions scaled by the number of elementary nucleon-nucleon interactions. Jet quenching also involves angular deflection that destroys the coplanarity of two jets with the incident beam axis[23], and changes the azimuthal pattern in the particle distribution.

1.3.7 Anisotropic flow

Anisotropic flow describes the azimuthal momentum distribution of particle emission with respect to the reaction plane [24, 25, 26, 27]. This topic will be discussed in later chapters.

Chapter 2

Anisotropic Flow

2.1 Introduction

Anisotropic flow provides indirect access to the EOS of the hot and dense matter formed in the reaction zone and helps us understand processes such as thermalization, creation of the QGP, phase transitions, etc., since the flow is likely influenced by the compression in the initial stages of the collision. It is thus one of the important measurements in relativistic heavy-ion collisions, and has attracted attention of both theoreticians and experimentalists[28].

It is convenient to quantify anisotropic flow by the Fourier coefficient of the particle distribution in emission azimuthal angle, measured with respect to the reaction plane, which can be written as:

$$E\frac{d^3N}{d^3p} = \frac{1}{2\pi}\frac{d^2N}{p_t dp_t dy}(1+\sum_{n=1}^{\infty} 2v_n \cos n\phi), \tag{2.1}$$

where the definition of p_t and y can be found in Appendix C, and ϕ denotes the angle between the particle's azimuthal angle in momentum space and the reaction plane angle. The sine terms in Fourier expansions vanish due to the reflection symmetry with respect to the reaction plane. It follows that $\langle \cos n\phi \rangle$ gives v_n:

$$\begin{aligned}
\langle \cos n\phi \rangle &= \frac{\int_{-\pi}^{\pi} \cos n\phi E \frac{d^3N}{d^3p} d\phi}{\int_{-\pi}^{\pi} E \frac{d^3N}{d^3p} d\phi} \\
&= \frac{\int_{-\pi}^{\pi} \cos n\phi (1+\sum_{m=1}^{\infty} 2v_m \cos m\phi) d\phi}{\int_{-\pi}^{\pi} (1+\sum_{m=1}^{\infty} 2v_m \cos m\phi) d\phi} \\
&= \frac{\int_{-\pi}^{\pi} 2v_n \cos^2 n\phi d\phi}{2\pi} \\
&= v_n \ , \qquad (2.2)
\end{aligned}$$

where the orthogonality relation between Fourier coefficients $\int_{-\pi}^{\pi} [\cos n\phi \cos m\phi]_{m\neq n} d\phi = 0$ has been used.

2.2 Flow components

The first and second harmonic, and higher even-order harmonics are of interest. The first two flow components are called directed flow and elliptic flow, respectively. The word "directed" (also called sideward flow) comes from the fact that such flow looks like a sideward bounce of the fragments away from each other in the reaction plane, and the word "elliptic" is due to the fact that the azimuthal distribution with non-zero second harmonic deviates from isotropic emission in the same way that an ellipse deviates from a circle. Fig. 2.1[29] is a schematic diagram illustrating directed and elliptic flow, viewed in the transverse plane (ϕ denotes the azimuthal angle with respect to the reaction plane).

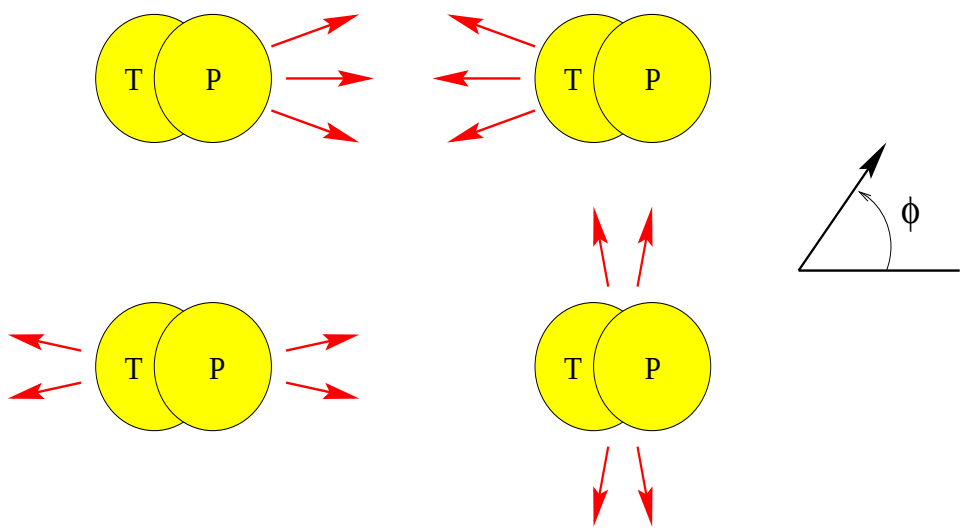

Figure 2.1: Major types of azimuthal anisotropies, viewed in the transverse plane. The target is denoted by T, and the projectile by P. Top: Directed flow on the projectile side of midrapidity, positive (left) and negative (right). On the target side of midrapidity, the left and right figures are interchanged. Bottom: elliptic flow, in-plane or positive (left) and out-of-plane or negative (right).

In the projectile rapidity region, if we follow the coordinate conventions of Fig. 2.1, then directed flow is $positive$ if $\langle \cos\phi \rangle > 0$, and $negative$ if $\langle \cos\phi \rangle < 0$. For mass-symmetric collisions (i.e., projectile and target nuclei are the same), $\langle \cos\phi \rangle$ is an odd function of rapidity, and signs are therefore reversed in the target rapidity region. For elliptic flow, we speak of in-plane elliptic flow if $\langle \cos 2\phi \rangle > 0$, and out-of-plane elliptic flow if $\langle \cos 2\phi \rangle < 0$. Elliptic flow has the same sign in the

projectile and target rapidity regions for mass-symmetric systems.

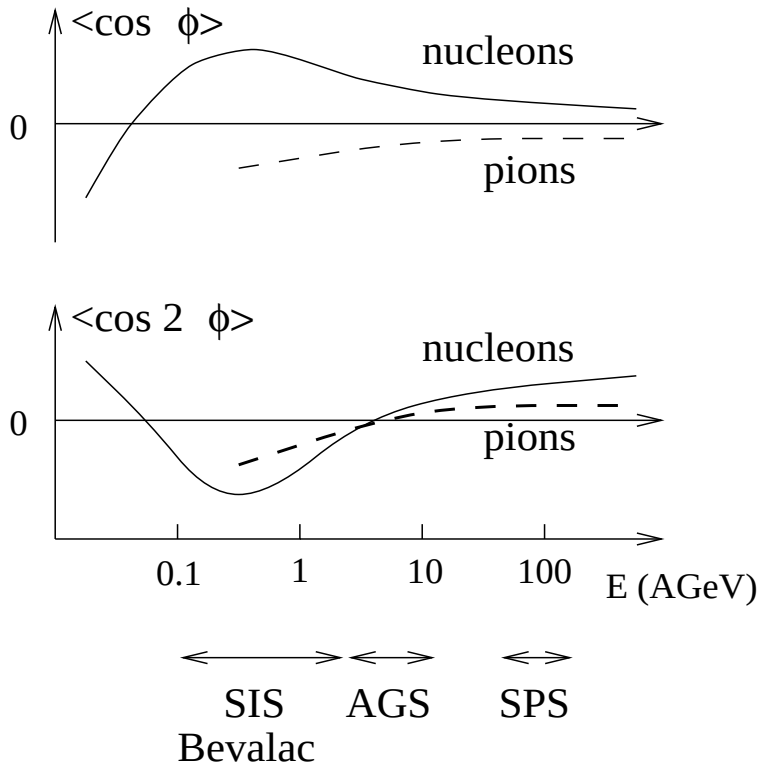

Figure 2.2: Schematic behavior of the magnitudes of directed flow (top) and elliptic flow (bottom) as a function of the bombarding kinetic energy per nucleon in the laboratory frame. Full lines: proton flow; dashed lines: pion flow. The plot is from [29].

At low energies (below about $100A$MeV in fixed target collisions), the interaction is dominated by the attractive nuclear mean field, which has two effects: first, projectile nucleons are deflected towards the target, resulting in negative directed flow [30]; second, the projectile and target form a rotating system, and the centrifugal force ejects particles in the rotation plane[31], producing in-plane elliptic flow[32, 33]. At higher energies, individual nucleon-nucleon collisions dominate over mean field effects. They produce a positive pressure, which deflects the projectile and target fragments away from each other in the center of mass frame ("bounce-off" and "sidesplash" effects [26]), resulting in positive directed flow. Furthermore, the participant nucleons, which are compressed in the region where the target and the projectile overlap (see Fig. 2.1), cannot escape in

the reaction plane due to the presence of the spectator nucleons ("squeeze-out effect" [34]), producing out-of-plane elliptic flow.

2.2.1 Directed flow

At RHIC energies, as the collision energy goes higher and higher, directed flow decreases and becomes relatively difficult to detect (Fig. 2.2). The first evidence of directed flow at the SPS accelerator at the CERN laboratory was reported by the WA98 collaboration[35]. Further measurements were made by NA49[36] and CERES[37]. The strength of directed flow at SPS is significantly smaller than at lower energies, especially in the mid-rapidity region.

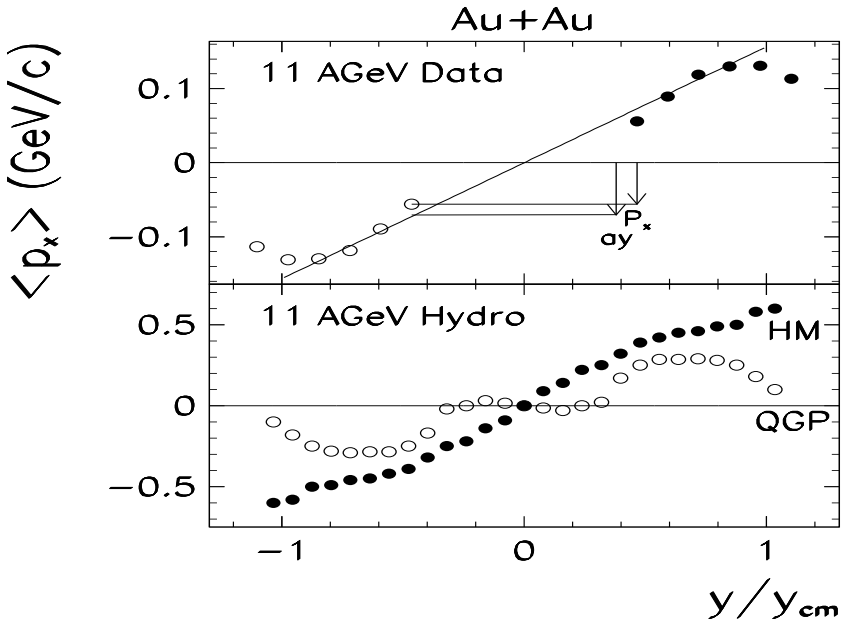

Figure 2.3: Upper part: Definition of the measure *softening*, S, describing the deviation of $P_x(y)$ or $v_1(y)$ from the straight line behavior, ay, around midrapidity. S is defined as $|ay - P_x(y)|/|ay|$. The lower figure shows a typical example for fluid dynamical calculations with Hadronic and QGP EOS. QGP leads to strong softening, $\sim 100\%$. The plot is from [40].

It has been argued that the increased entropy density at the onset of QGP production should lead to a "softest point" in the nuclear equation of state [38]. In Ref[39], this softening was predicted to lead to a reduction of the directed flow, making the phase transition visible as a minimum in its beam energy dependence. A different manifestation of softening due to possible QGP formation was discussed by Csernai and Rohrich [40] (see Fig. 2.3). As shown by the hydrodynamic calculation with QGP in Fig. 2.3, directed flow as a function of rapidity crosses zero three times in the neighborhood of mid-rapidity, and displays a $wiggle$ shape. The wiggle here is predicted to occur in close-to-central collision events. A follow-up study [41] demonstrates that the wiggle structure

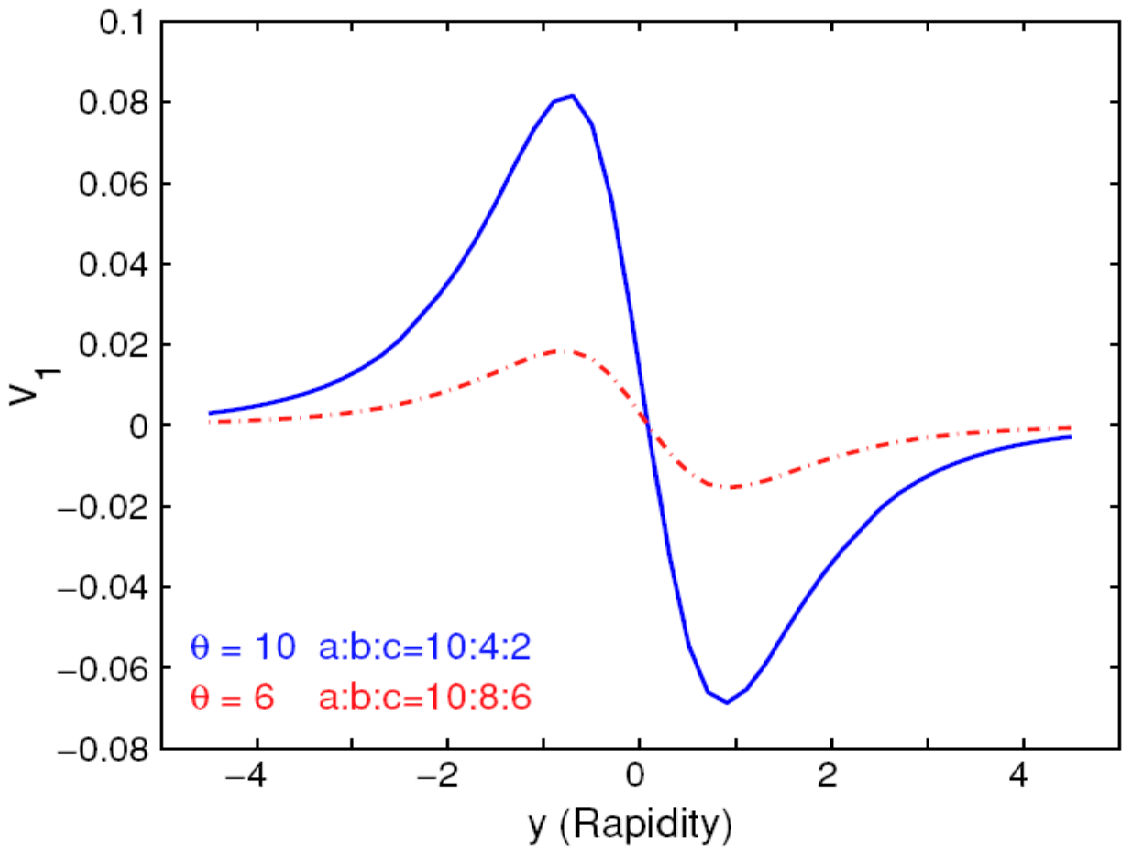

Figure 2.4: Directed flow, as a function of rapidity, from tilted, ellipsoidally expanding fluid sources. The chain curve refers to a source with tilt angle, $\Theta = 6°$, and half-axes $a = 10$ fm, $b = 8$ fm and $c = 6$ fm, while the full curve refers to a source with tilt angle, $\Theta = 10°$, and half-axes $a = 10$ fm, $b = 4$ fm and $c = 2$ fm. The plot is from [41].

in $v_1(y)$ could be produced by a tilted, ellipsoidally expanding fluid source with QGP. Fig. 2.4

[41] shows the hydrodynamic calculation of $v_1(y)$ from tilted fluid sources. The magnitude of v_1 becomes larger when the source is more tilted.

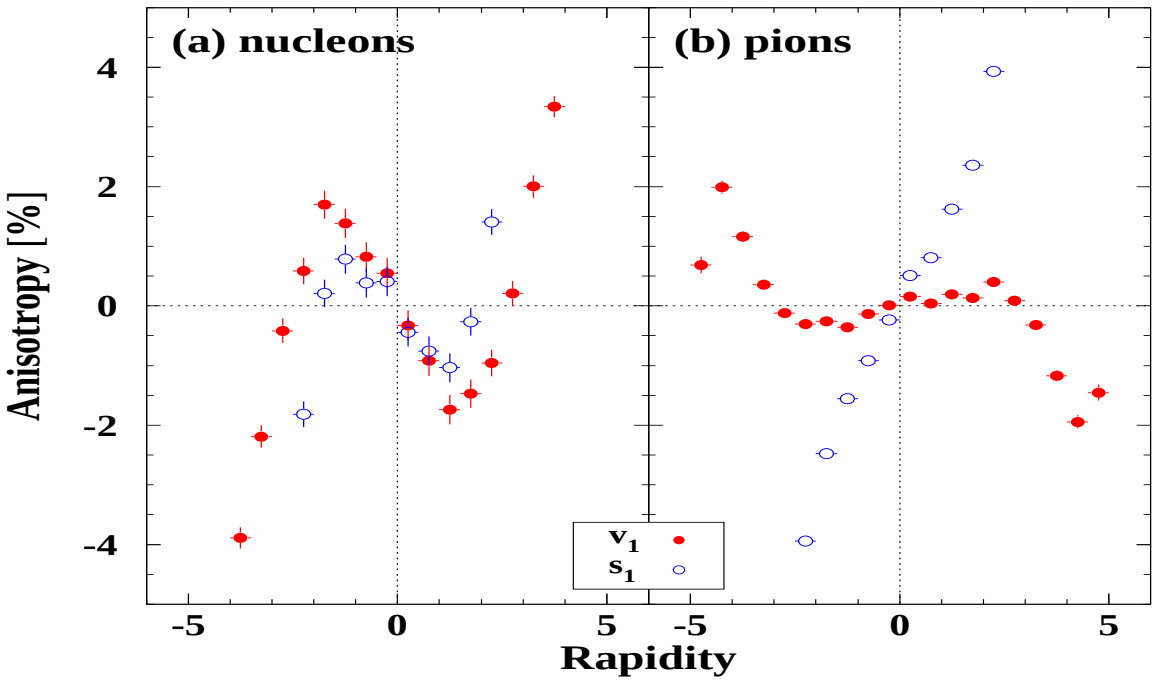

Figure 2.5: RQMD calculations of v_1 (filled circles) and s_1 (open circles) for nucleons (left panel) and pions (right panel) in Au + Au collisions at RHIC energies. The plot is from [42]

The wiggle structure in the rapidity dependence of directed flow is also predicted by RQMD [42] calculations (see Fig. 2.5). RQMD (Relativistic Quantum Molecular Dynamics) is a microscopic nuclear transport model and does not assume formation of a QGP. In this simulation, the wiggle results from the combination of space-momentum correlations characteristic of radial expansion, together with the correlation between the position of a nucleon in the nucleus and how much rapidity shift it experiences during the collision.[42] The wiggle predicted by this mechanism appears in peripheral or mid-peripheral collision events.

An investigation of possible wiggle structures at RHIC is among the main goals of this dissertation.

2.2.2 Elliptic flow

Elliptic flow results from the initial geometric deformation of the reaction region in the transverse plane. At RHIC energies, elliptic flow tends to preferentially enhance momenta along the direction of the smallest spatial extent of the source [43, 44], and thus the in-plane (positive) component of elliptic flow dominates. In general, large values of elliptic flow are considered signatures of hydrodynamic behavior, while smaller signals can have alternative explanations.

The centrality dependence of elliptic flow is of special interest[45, 46]. In the low density limit(LDL), the mean free path is comparable to, or larger than, the system size, and the colliding nuclei resemble dilute gases. The final anisotropy in momentum space depends not only on the initial spatial eccentricity ϵ (defined below), but also on the particle density, which affects the number of rescatterings. In this limit, the final elliptic flow (see a more detailed formula in [47]) is

$$v_2 \propto \frac{\epsilon}{S}\frac{dN}{dy}, \tag{2.3}$$

where dN/dy characterizes density in the longitudinal direction and $S = \pi R_x R_y$ is the initial tranverse area of the overlapping zone, with $R_x^2 \equiv \langle x^2 \rangle$ and $R_y^2 \equiv \langle y^2 \rangle$ describing the initial geometry of the system in the x and y directions, respectively. (The $x - z$ axes determine the reaction plane). The averages include a weighting with the number of collisions along the beam axis in a wounded nucleon [48] calculation. The spatial eccentricity is defined as

$$\epsilon = \frac{R_y^2 - R_x^2}{R_x^2 + R_y^2}, \tag{2.4}$$

and for hard spheres is roughly proportional to the impact parameter over a wide range of that variable.

As follows from Eq. 2.3, the elliptic flow increases with the particle density. Eventually, it saturates [29] at the hydro limit. In a hydrodynamic picture, where the mean free path is much less than the geometrical size of the system, the ratio of v_2 to ϵ is expected to be approximately constant [24].

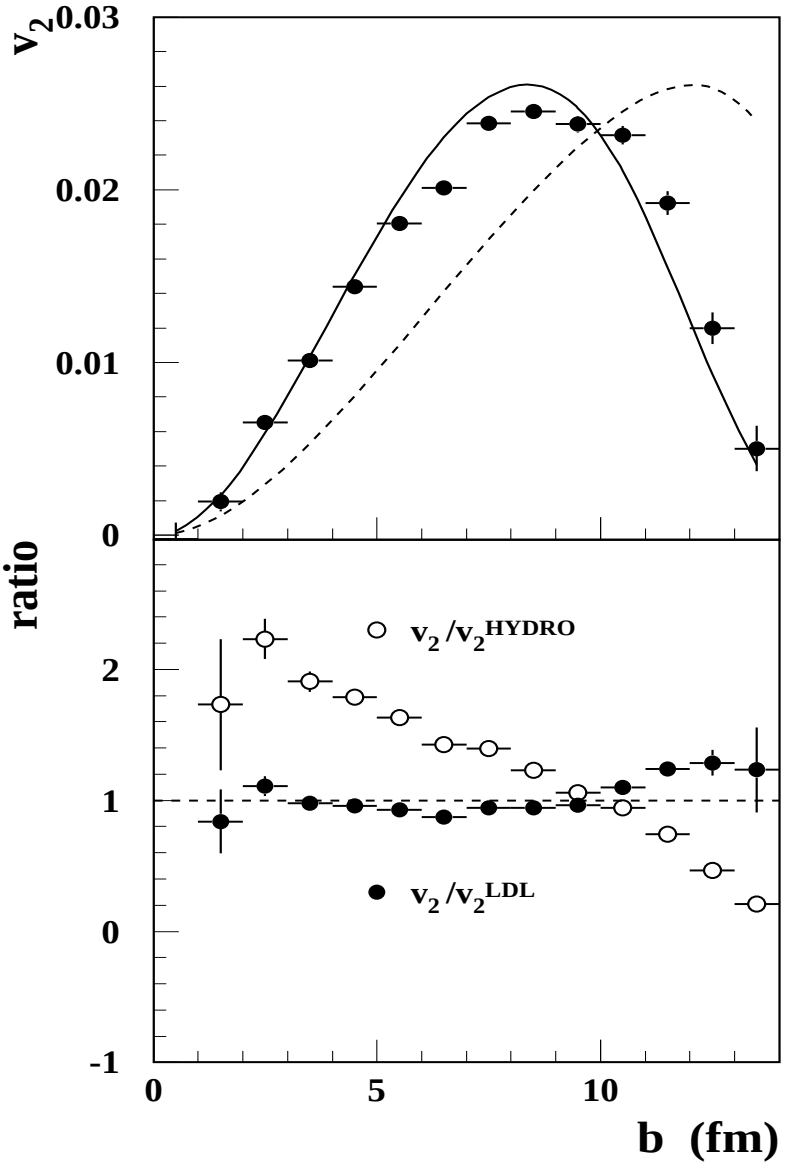

Figure 2.6: Top: comparison of elliptic flow, v_2 as a function of impact parameter, for pions from RQMD version 2.3 (filled circles) with the dependence expected for the low-density limit (solid line) and that expected for the hydro limit (dashed line). Bottom: ratios of $v_2^{\mathrm{RQMD}}/v_2^{\mathrm{LDL}}$, and $v_2^{\mathrm{RQMD}}/v_2^{\mathrm{HYDRO}}$. The plot is from [45].

Fig. 2.6[45] shows that the position of the maximum in $v_2(b)$ shifts towards peripheral events going from an LDL calculation to a hydrodynamic calculation.

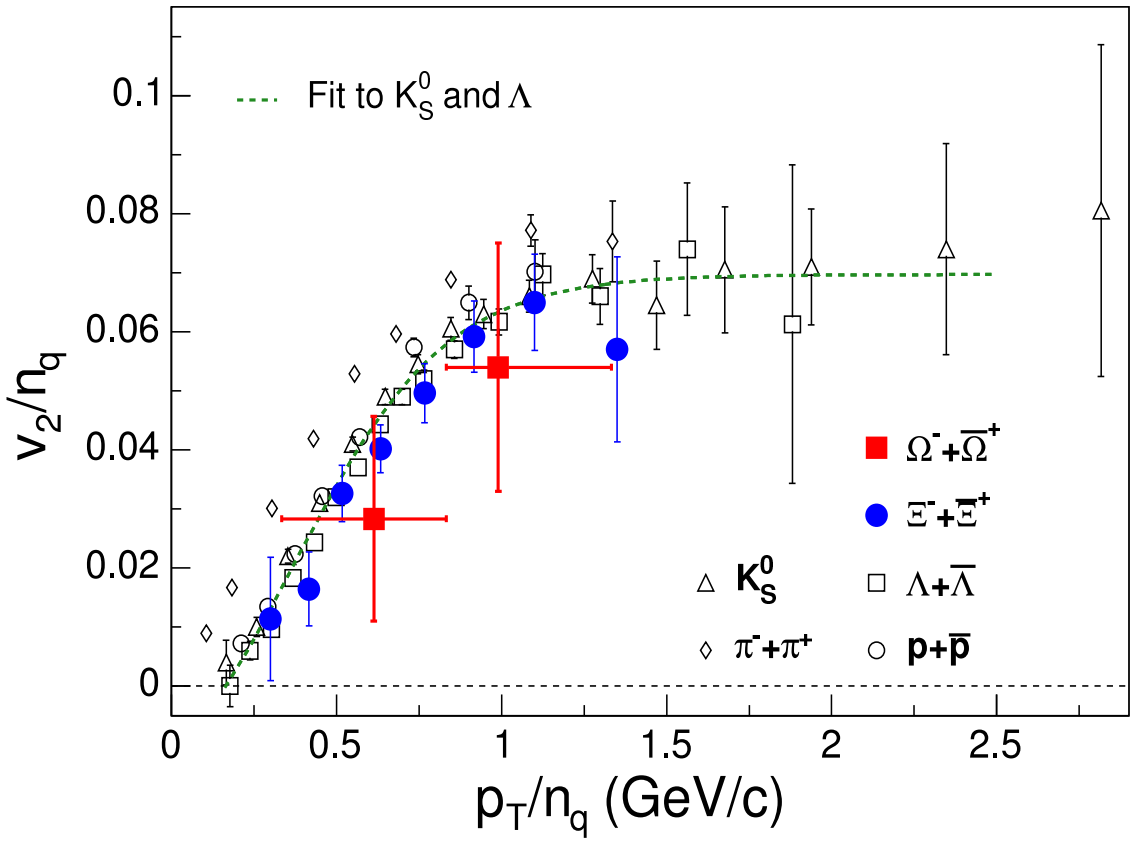

Figure 2.7: v_2 per number of constituent quark (n_q) as a function of p_t/n_q for $\Xi^- + \bar{\Xi}^+$ (filled circles) and $\Omega^- + \bar{\Omega}^+$ (filled squares). [49] The quantities are also shown for $\pi^+ + \pi^-$ (open diamonds), $p + \bar{p}$ (open triangles) [50], K^0_S (open circles), $\Lambda + \bar{\Lambda}$ (open squares) [51]. All data are from 200 GeV Au+Au minimum bias collisions. The dot-dashed-line is the scaled result of the fit to K^0_S and Λ [52]. The plot is from [49].

The differential momentum anisotropy $v_2(p_t)$ is also of interest, especially for different hadron species. Fig. 2.7 shows v_2 per number of constituent quark (n_q) as a function of p_t/n_q for various particle species [49, 50, 51, 52]. All hadrons, except pions, fall into the same curve within statistics, and there are plausible reasons to expect the pions to deviate [51]. This universal scaling behavior lends strong support to the finding that collectivity is developed in the partonic stage at RHIC[49].

2.3 Flow analysis with event plane

Eq. 2.2 provides a way to evaluate flow components using the reaction plane. The estimated reaction plane is called the event plane. If the event plane is estimated from the m-th order of flow component, then we speak of the m-th order event plane. With the observed event plane instead of the ideal reaction plane, Eq. 2.2 becomes

$$v_n = \langle \cos n\phi \rangle = \langle \cos[n(\varphi - \psi_r)] \rangle = \frac{\langle \cos[n(\varphi - \psi_m)] \rangle}{\langle \cos[km(\psi_m - \psi_r)] \rangle}, \tag{2.5}$$

where φ denotes a particle's azimuthal angle, ψ_r represents the azimuthal angle of the reaction plane, and ψ_m the m-th order event plane. The numerator of Eq. 2.5 is considered to be the observed flow value, and the denominator characterizes the $event\ plane\ resolution$ [53]. In general, better accuracy for determination of v_n is obtained with the event plane (ψ_n) estimated from the same harmonic (m = n, k = 1). That is because the resolution deteriorates as k increases (see detailed discussion on event plane resolution in Chapter 6 and [28]).

2.4 Non-flow effects

There are sources of azimuthal correlation, known as non-flow effects, which are not related to the reaction plane orientation. Examples include correlations caused by resonance decays, (mini) jets, strings, quantum statistics effects, final state interactions (particularly Coulomb effects), momentum conservation, etc. To suppress the sensitivity of flow analysis to non-flow effects, the multi-particle cumulant method [54, 55] and the mixed harmonic event plane method [56] have been developed, and the results of these two methods for Au+Au collisions at $\sqrt{s_{NN}}$ = 200 GeV are discussed in [57]. It is one of the goals of this dissertation to use a new detector subsystem, plus a new method of flow analysis to minimize the influence from non-flow effects. As discussed in Chapter 4, this new detector and its associated method of flow analysis offers some unique advantages over the previous approaches for studying anisotropic flow.

Chapter 3

STAR Experiment

3.1 The layout of the STAR experiment

The Solenoidal Tracker at RHIC (STAR) is one of the two large detector systems constructed at RHIC. The perspective view of the STAR detector is shown in Figure 3.1. STAR was designed primarily to measure hadron production over a large solid angle, featuring detector systems for high precision tracking, momentum analysis, and particle identification at mid-rapidity. The large acceptance of STAR makes it particularly well suited for event-by-event characterizations of heavy ion collisions [58].

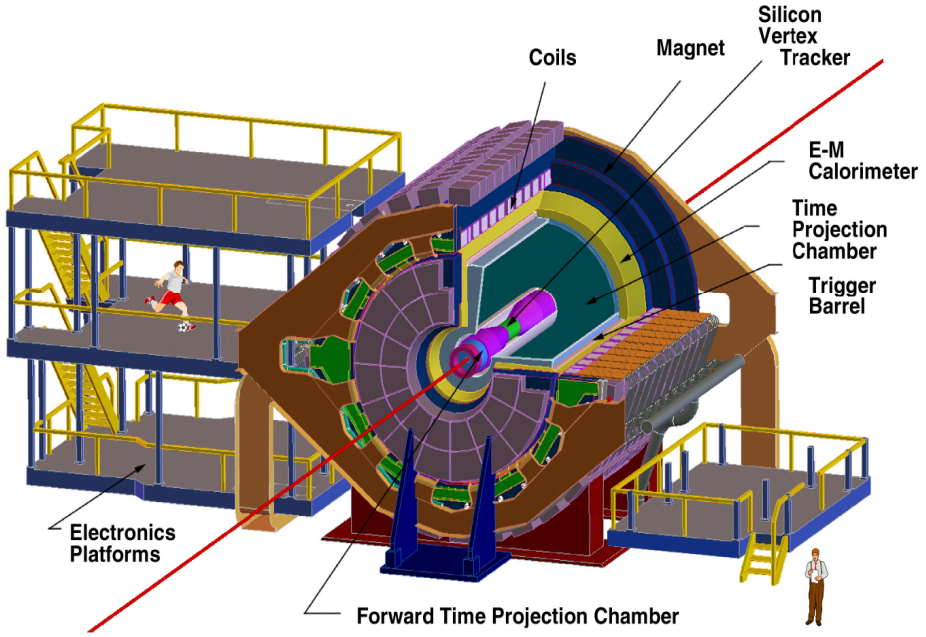

Figure 3.1: The perspective view of the STAR detector, with a cutaway for viewing inner detector systems. The figure is from [58].

A cutaway side view of the STAR detector as configured for the RHIC 2001 run is displayed

in Figure 3.2. A room temperature solenoidal magnet [59] provides a uniform magnetic field of maximum strength 0.5 T for charged particle momentum analysis. A large volume Time Projection Chamber (TPC) [60] for charged particle tracking and particle identification is located at a radial distance from 50 to 200 cm from the beam axis. The TPC is 4.2 meters long, and covers a pseudo-rapidity range $|\eta| < 1.8$ for tracking with complete azimuthal symmetry. To extend the tracking to the forward region, a radial-drift TPC (FTPC) [61] is installed covering $2.5 < |\eta| < 4$, also with complete azimuthal coverage and symmetry. Charged particle tracking close to the interaction region is accomplished by a Silicon Vertex Tracker (SVT) [62].

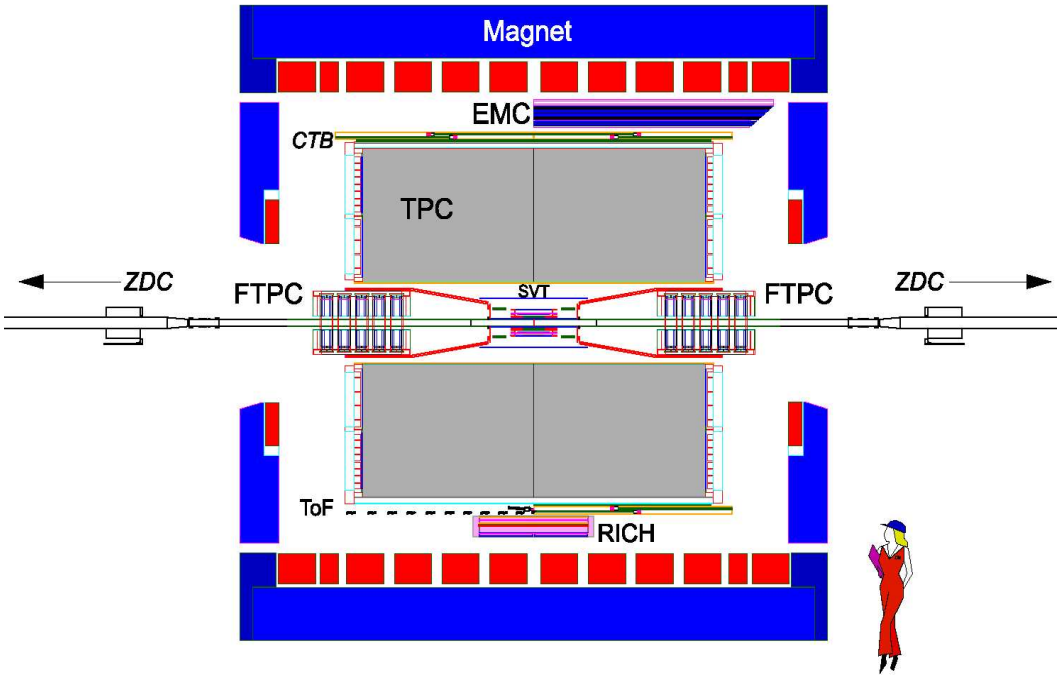

Figure 3.2: The cutaway side view of the STAR detector as configured in 2001. The figure is from [58].

The fast detectors that provide input to the trigger system [63] are a central trigger barrel(CTB) at $|\eta| < 1$ and two zero-degree calorimeters (ZDC) [64] located in the forward directions at $\theta < 2$ mrad. The CTB surrounds the outer cylinder of the TPC, and triggers on the flux of charged particles at mid-rapidity. The ZDCs are used for determining the energy of spectator neutrons.

3.2 STAR main TPC

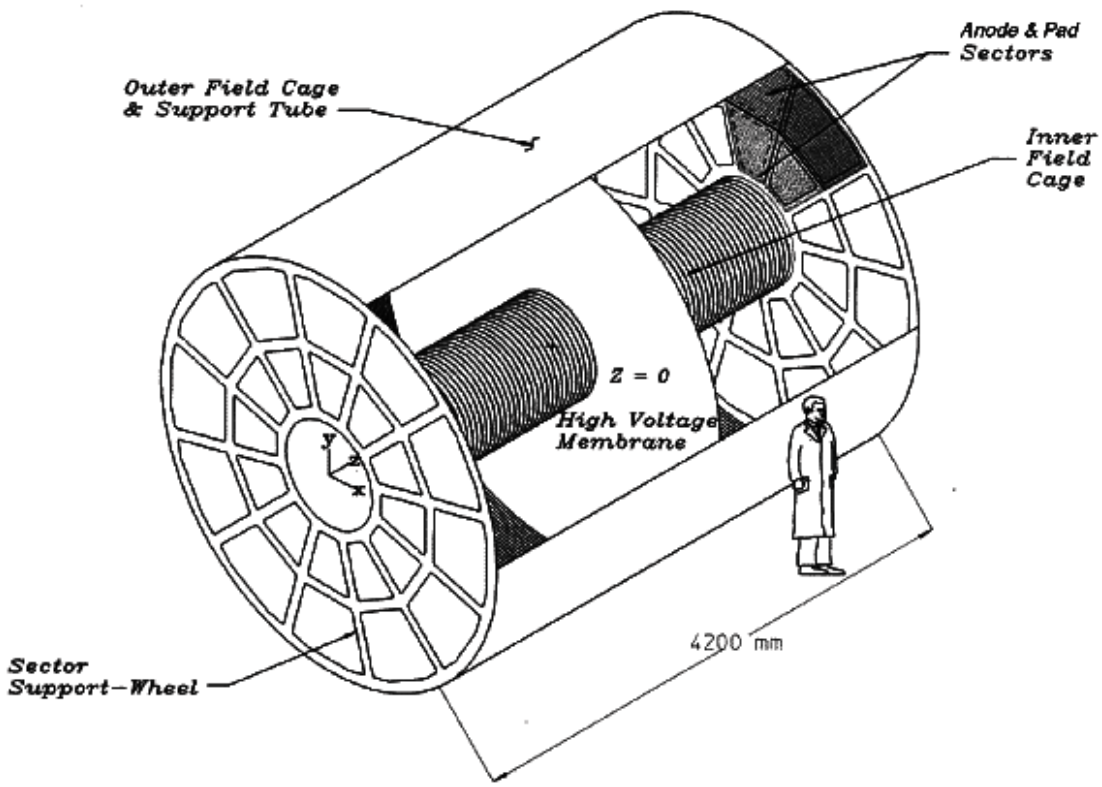

Figure 3.3: Perspective view of the STAR Time Projection Chamber. The figure is from [60].

The TPC is a continuous tracking detector capable of handling events with thousands of tracks [65]. It determines the momenta of individual particles by tracing them through a solenoidal magnetic field and identifies many of them by making multiple energy loss measurements.

The major mechanical components of the TPC (Fig. 3.3) consist of the outer field cage (OFC), the inner field cage (IFC), the high voltage central membrane (CM) and some other support devices. The CM is located in the middle of the TPC and is held at high voltage ($\sim$ 31 kV). The OFC and the IFC define the active gas volume (see below), while their major function is to provide a nearly uniform electric field along the axis of the cylinder in which electrons drift to the anode plane. The TPC is filled with a mixture of 90% Ar and 10% CH_4 gas. When a charged particle traverses the

TPC volume, it ionizes gas atoms every few tenths of a millimeter along its path and leaves behind a trail of electrons. The paths of primary ionizing particles are reconstructed with high precision from the trails of the released secondary electrons which drift to the readout end caps at the ends of the chamber.

The performance of the TPC meets the original design specifications[66]. For reference, the standard deviation of the position resolution for points along a track traversing the TPC parallel to the pad plane was found to be 0.5 mm. The momentum resolution was determined to be $\delta p/p < 2\%$ for tracks with momentum $p = 500$ MeV$/c$. The resolution in ionization energy loss (dE/dx) was found to reach 8% for tracks measured over the entire radial dimension of the TPC.

3.3 STAR forward TPCs

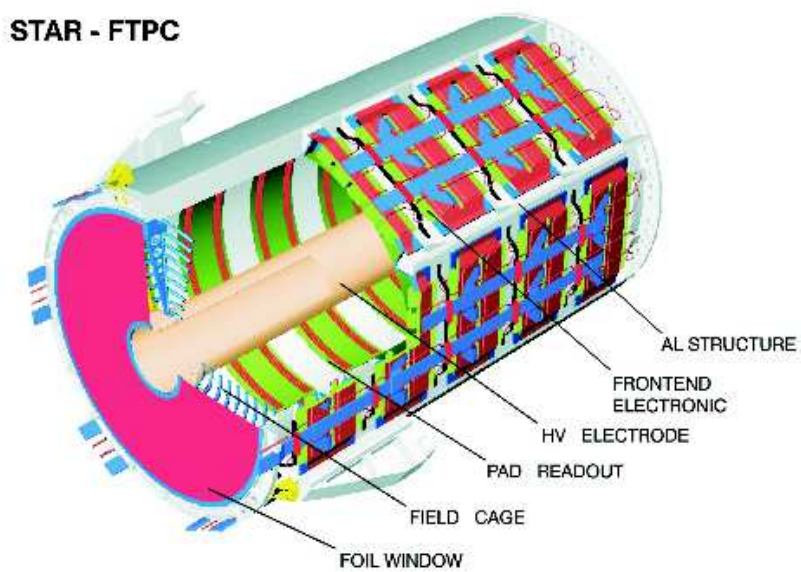

Figure 3.4: Schematic diagram of a STAR FTPC. The figure is from [61].

The two FTPCs in STAR cover the pseudorapidity range $2.5 < |\eta| < 4.0$, correspond to track

angles from 2° to 9.3° with respect to the beam axis. To get good momentum resolution for the tracks in this region of high particle density, a high spatial resolution is needed, and a two-track separation on the order of 2 mm is necessary. [61] To meet both of these criteria, a drift toward the detector endcaps, as in STAR's main TPC, is not practical. A radial drift design was adopted to achieve the desired performance.

In Fig. 3.4, a schematic diagram of a STAR FTPC is shown, including the field cage with potential rings at the endcaps, the padrows on the outer surface of the gas volume and the front end electronics. In this geometry, the clusters originate from near the inner radius of the detector, drift radially towards the outer surface, and spread apart, which improves the two-track separation. The short drift distance in the radial direction allows the use of $\mathrm{Ar/CO_2}$ ($50\%/50\%$), a gas mixture with small diffusion. [61]

Based on the prototype measurements and simulations, the FTPCs achieve a position resolution of 100 μm, a two-track separation of 1 mm, a momentum resolution between 12$\%$ and 15$\%$, and an overall reconstruction efficiency between 70$\%$ and 80$\%$. [61]

3.4 STAR ZDCs

STAR ZDCs are placed at ± 18 m from the center of the intersection, and each consists of 3 modules containing a series of tungsten plates. [63] The ZDCs measure the energy of neutrons associated with the spectator matter, and are used for beam monitoring, triggering, and locating interaction vertices. A minimum bias trigger was obtained by selecting events with a pulse height larger than that of one neutron in each of the ZDCs, which corresponds to 95 percent of the geometrical cross section. [58]

Fig. 3.5 shows the correlation between the ZDC and the CTB. For large impact parameters, the signals in both the ZDC and the CTB are small because only a few spectator neutrons are produced and multiplicity is relatively low. The CTB signal decreases continuously as the impact parameter decreases while the ZDC signal increases to saturation, then decreases eventually for small impact

parameters. The combined information can be used to provide a trigger for collision centrality.

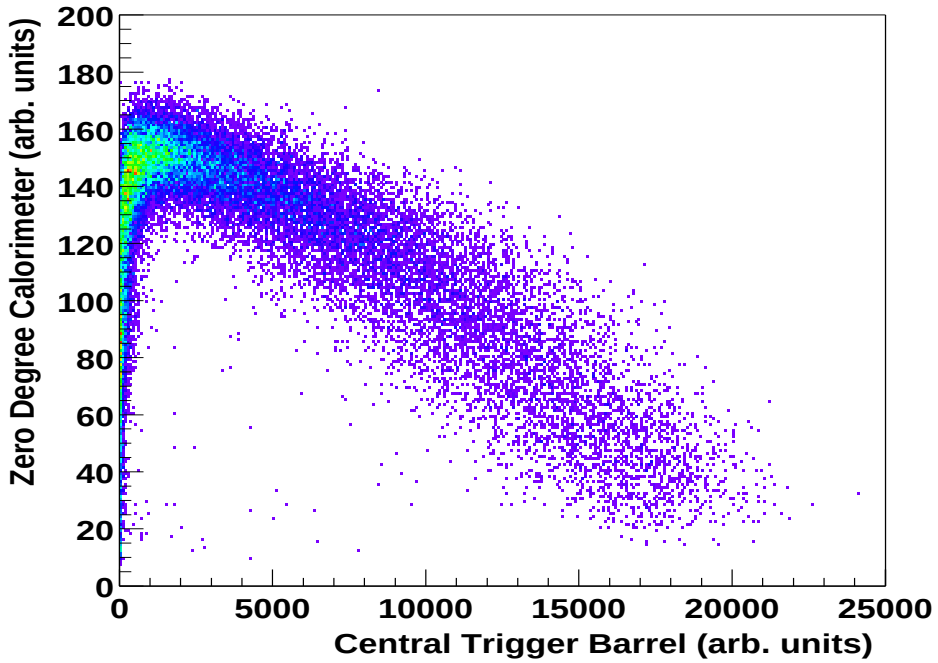

Figure 3.5: Correlation between pulse heights from the Zero Degree Calorimeters and the Central Trigger Barrel in a minimum bias trigger. The figure is from [58].

Baseline ZDCs only measure the event-by-event energy deposition of spectator neutrons, and have no transverse segmentation. To study the spatial distribution of the neutron hits on the transverse plane of the ZDCs, a Shower Maximun Detector (SMD) was installed between the first and second modules of each existing STAR ZDC during the early stage of RHIC run IV (2004). The details of this upgrade will be discussed in later chapters.

Chapter 4

Upgrade of STAR ZDC

In October 2003, we proposed the addition of a Shower Maximum Detector (one plane of 7 vertical slats and another of 8 horizontal slats) to the STAR Zero Degree Calorimeters, closely resembling the ZDC-SMD already used by PHENIX in RHIC run III. The SMD was installed on Feb 4 2004, and since then has added significant capability to STAR in four areas of physics: anisotropic flow, strangelet searching, ultra-peripheral collisions, and spin physics.

4.1 Physics motivation

The STAR ZDCs in their baseline form provide a signal that is correlated with the number of spectator neutrons produced in the collision. An upgrade that provides some information about the event-by-event pattern of transverse momentum among these neutrons opens up enhanced physics capabilities. In the subsections below, we discuss four areas of STAR physics where this new information is of significant value.

4.1.1 Flow

Besides the opportunity to study directed flow of nucleons in the nuclear fragmentation region, a new rapidity region for STAR, the addition of the SMD provides new information on the reaction plane, and can enhance the full range of anisotropic flow studies in the central TPC and the FTPCs. The main advantages of using the reaction plane from the ZDC-SMD compared to the techniques previously used are:

- New knowledge concerning *the direction of the impact parameter vector*, since the reaction plane is determined from the first harmonic flow. Besides other benefits mentioned below,

this makes possible some measurements that were totally excluded before, like HBT measurements with respect to the first order reaction plane (to measure the source tilt with respect to the beam axis).

- *Minimal, if any, non-flow effects*. Non-flow azimuthal correlations originate mostly from various kinds of cluster decays and jet-like correlations. These effects span a rapidity region of at most a few units. The ZDC, located in the projectile fragmentation region, is at least 6 units away from midrapidity.

- *Minimal, if any, effects from flow fluctuations*. The possibly large effects of flow fluctuations in previous measurements are due to the fact that, for example, elliptic flow was measured with respect to the reaction plane determined from the same second harmonic flow, and in the same pseudorapidity region. Measurements of the nth harmonic signal v_n from some methods are of the form $\langle v_n^k \rangle^{1/k}$ etc rather than being the desired quantity $\langle v_n \rangle$, averaged over a certain set of events, and event-by-event fluctuations can cause these two observables to differ. The use of the reaction plane determined from the directed flow, and furthermore, from directed flow of spectator neutrons (as opposed to produced particles) drastically suppresses these undesired effects.

In the previous STAR configuation, only the FTPCs provided information on the directed flow (v_1). Unfortunately, the directed flow among charged particles at FTPC pseudorapidities is very small, and $v_1(\eta)$ possibly changes sign within the region covered by the FTPCs. Both of these factors result in the FTPCs not being suitable to substitute in the role of the ZDC-SMD detector as explained above.

It is not required that the reaction plane resolution from the ZDC-SMD be as good as the 2nd-order reaction plane resolution obtained from the main TPC. In a typical analysis that is limited by systematic uncertainties rather than statistics, a decrease in the reaction plane resolution may not

adversely affect the result. The reaction plane resolution that the ZDC-SMD provides depends on the magnitude of v_1 among spectator neutrons, which had not yet been measured at RHIC before the installation of the ZDC-SMD. The best available indications suggested that spectator v_1 is quite large. WA98 has measured a 20% v_1 signal among spectators at the SPS and $\langle p_t \rangle \approx$ 25 MeV [67]. STAR measurements of v_1 among charged particles at FTPC pseudorapidities are remarkably close to the v_1 for pions in NA49 at the same pseudorapidity relative to the beam [68]. This observation is consistent with limiting fragmentation [69] and is supportive of the conclusion that v_1 among spectators is independent of beam energy between SPS and RHIC.

4.1.2 Strange quark matter

Strange Quark Matter (SQM) is matter with about equal numbers of u, d and s quarks, existing in one QCD bag. It has been predicted to be metastable or stable [70]. It can be as small as the A=2 H-Dibaryon, or as large as a strange star with $A = 10^{57}$. Strange quark matter has many fascinating properties, and its existence would have major impacts on physics, astrophysics, cosmology, and possibly on technology as well [70]. Strange Quark Matter has been searched for among pulsars, stars and cosmic rays, as well as in the earth's soil, and in heavy ion collisions. An extensive review of experimental results is provided in Ref. [71]. In heavy ion collisions, there have been several experiments dedicated to strangelet searches: E864 and E896 at the AGS, and NA52 at the CERN/SPS. Further strangelet searches has been proposed to be carried out by AMS, ALICE and CMS. The ZDC-SMD allowed us to search for strangelets with $10 \lesssim$ mass $\lesssim 100$ GeV/c^2 in STAR. The basic idea is to search for a large energy deposition with a narrow tansverse profile in the ZDC in central AuAu collisions. Central AuAu collisions provide violent compression of the nucleus and large numbers of baryons at forward rapidity, and is ideal for strangelet searching. Since the DX magnets sweep away the beam particles and other charged particles, the ZDCs are only sensitive to neutral particles or matter with abnormally small charge-to-mass ratio, like strangelets.

4.1.3 Ultra-peripheral collisions

Adding an SMD to the STAR ZDCs qualitatively expands the STAR UPC program, by allowing the study of photoproduction with polarized photons. The SMDs can be used to tag photon polarization, in a similar manner to how ZDC neutrons are used to tag the impact parameter vector. The neutron tagged samples have different impact parameter distributions from untagged events.

Position sensitive ZDCs are sensitive to the direction of the impact parameter vector. Most UPC single neutron tags come from giant dipole resonances (GDRs). GDRs decay in a simple dipole transition. In the transverse plane, the angle θ between the neutron p_t and the photon polarization is distributed as $\cos^2\theta$. The photon polarization is parallel to the electric field vector. In a photonuclear interaction, the electric field parallels the impact parameter (b). The neutron p_t thus tags the direction of b [72]. Any additional photons in the reaction will also be polarized along b. When the ZDC is used to measure a neutron p_t , it provides information about the polarization of other photons that participate in the reaction, tagging the photon polarization. The linearly polarized tagged beam can be used to study a variety of photonuclear interactions. Here, we mention 3 possible studies:
(1) Mutual GDR Excitation. Single neutrons are observed in each ZDC. The two neutron p_t vectors should have an angular correlation:

$$C(\Delta\phi) = 1 + \frac{1}{2}\cos 2\Delta\phi \tag{4.1}$$

where $\Delta\phi$ is the angle between the two neutrons. For more complicated events, one could use mutual GDR as a double-tag, for even better determination of the photon polarization.
(2) Polarized ρ^0 Photoproduction. In ρ^0 decay, the π^+ and π^- directions follow the photon polarization. In the simplest models, the plane formed by the π^+ and π^- directions follows a $\cos^2\theta$ distribution with respect to the photon polarization. This has been studied with low energy photons, with very limited precision. STAR could look for violations from this simple diffractive prediction.

Less is known about heavier mesons; polarized J/ψ photoproduction has not yet been studied

experimentally. It may be sensitive to the polarized gluon content of nuclei. Inelastic J/ψ photoproduction is of interest as a test of quarkonium production models [73].

(3) The polarization will be useful for further studies of wave function collapse. There should be no *a priori* knowledge of the direction of b, so in a mutual GDR excitation, the two excited nuclei form an entangled system of spin 1 particles; the neutrons from the decay act as spin analyzers. This system might be useful for tests related to Bell's inequality.

More speculatively, we could study polarized photoproduction of open charm.

4.1.4 Spin physics

The first collisions of transverse polarized protons at $\sqrt{s} = 200$ GeV at RHIC from December 2001 until January 2002 (run II) at BNL were the beginning of a multi-year experimental program which aims to address a variety of topics related to the nature of the proton spin such as:

1. spin structure of the proton (gluon contribution of the proton spin, flavor decomposition of the quark and anti-quark polarization and transversity distributions of the proton),
2. spin dependence of fundamental interactions,
3. spin dependence of fragmentation and
4. spin dependence of elastic polarized proton collisions.

A recent review and status of the RHIC spin program can be found in Ref. [74].

The first collisions of longitudinal polarized protons at $\sqrt{s} = 200$ GeV have been achieved during RHIC run III in May 2003 with the successful commissioning of the STAR and PHENIX spin rotator magnets to allow for the precession from transverse to longitudinal polarization.

The underlying mechanism for non-zero transverse-single spin asymmetries for forward neutron production has not been understood. It likely requires a forward hadronic calorimeter system with larger acceptance to understand the origin of the measured forward neutron asymmetries in transverse polarized pp collisions. ZDC-SMD is an upgraded detector system as an additional local polarimeter system besides the STAR FPD and STAR BBC detector system. It also has the potential

to provide a means of relative luminosity measurement which is crucial for any asymmetry measurement in longitudinal polarized proton collisions, e.g., the measurement of A_{LL}, which is the principal measurement to access the gluon polarization.

4.2 Simulations

4.2.1 Flow

The simulations described in this section were carried out in 2003 and were an essential part of the proposal for construction and installation of the ZDC-SMD. Now that the proposal was approved and we have real data from the ZDC-SMDs, the simulation results are of interest maily as a check on the dependability of our simulation methods. The simulations mainly address the question of how well resolved would be the expected neutron v_1 signal over a range of centralities.

The simulations are based on a number of assumptions or approximations:

- In each event, up to 30 neutrons are incident upon each ZDC. We consider three cases: 5, 15 and 30 neutrons.

- Spectator neutrons are generated with a random p_t distribution according to Fermi momentum. Each event is assigned a random reaction plane azimuth, and a v_1 correlation is then imposed.

- We assume v_1 = 20% as the most likely value to be found among spectators at RHIC (see section 4.1.1). In order to probe the response to a much smaller v_1 signal, we also investigate v_1 = 2% and 2.5%. These values allow us to verify sensitivity to small signals.

- We assume that the shower produced by each neutron deposits light in more than one slat in each of the two layers, according to a Gaussian profile in the transverse plane. We assume a standard deviation of 1.8 cm in each of x and y. This parameter comes from work oriented to this project using a GEANT-based simulation code first developed when the ZDCs were being

designed [75]. This GEANT-based ZDC code has since been verified as being in excellent agreement with real data.

- For each simulated event, we sum the shower signals for the individual neutrons in each plane of slats. We assume the signal amplitude fluctuates like the absolute value of a Gaussian random number (with mean $= 0$ and rms $= 1$), according to another GEANT-based simulation. The mean position along each axis defines a centroid point in the transverse plane for each event.

- The azimuth of the centroid relative to the point that corresponds to p_t = 0 is the estimated reaction plane azimuth. Computing this quantity is not necessarily the most useful way to extract physics in practice, but it is an intuitive observable and is well-suited for illustrating the expected performance of the device.

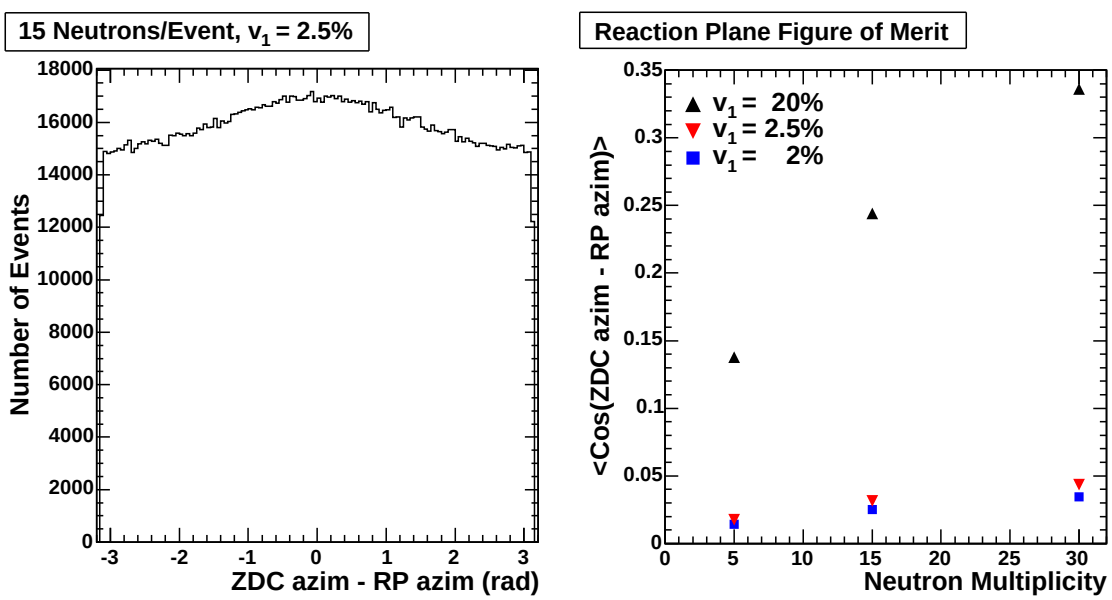

Figure 4.1: Flow simulation.

The left-hand panel of Fig. 4.1 illustrates a typical distribution of the difference between the input reaction plane azimuth and the azimuth reconstructed as per the simulation above. The relative

strength of the signal, i.e., the extent to which the distribution is peaked at zero angular difference, can be characterized by the mean cosine of the angular difference. The right-hand panel summarizes this correlation strength (essentially a figure of merit for how well the azimuth of the reaction plane is resolved) for all 9 cases studied — 3 different values for v_1 and 3 different spectator neutron multiplicities. Even in the case of the smallest v_1 and lowest neutron multiplicities, the plotted quantity $\langle \cos(\psi_{\mathrm{ZDC}} - \psi_{\mathrm{RP}}) \rangle$ still lies above 0.02, and this figure of merit would still be adequate to extract useful physics. For the reasons discussed at the beginning of this section, the black triangles correspond to what was expected to be observed in the ZDC-SMD, and has since then been verified by real data (see section 6.1.3).

4.2.2 Strangelets

A strangelet would initiate a large shower in the ZDC since it carries a large mass, much as a normal nucleus. A cluster of neutrons can give a large energy signal in ZDCs as well, but the signals from neutron clusters are more dispersed in the perpendicular dimensions due to the Fermi motion of spectator neutrons. The shower from a strangelet will originate in a single point in the ZDC, while a cluster of neutrons will have showers originating from each of the neutrons dispersed over the surface of the detector.

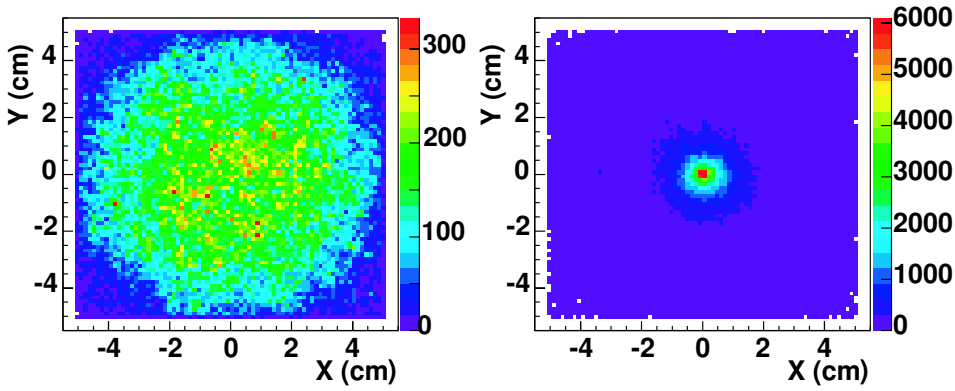

Figure 4.2: Simulation of the shower profile of neutron clusters (left) and strangelets (right). This plot shows the simulated shower profiles with far higher transverse resolution than can be obtained with our ZDC-SMDs.

This is shown by the Geant simulation in Fig. 4.2, in which the shower profile in the X-Y plane (X and Y axes are perpendicular to the beam direction) is plotted for neutron clusters (left) and strangelets (right). For neutron clusters, the hits are dispersed due to the normal p_t distribution among spectator neutrons. The simulation for a strangelet shows a prominent peak and less dispersion. Thus one can distinguish a strangelet event from normal events if, in addition to the total energy deposition in the ZDCs, the transverse distribution of energy deposition at the ZDCs can be obtained. The ratio of the transverse rms width of strangelets to that of neutron clusters is 0.69 $\pm$ 0.12. This ratio and its error applies to the relatively coarse transverse resolution of the 7-slat by 8-slat ZDC-SMD.

4.3 Hardware configuration

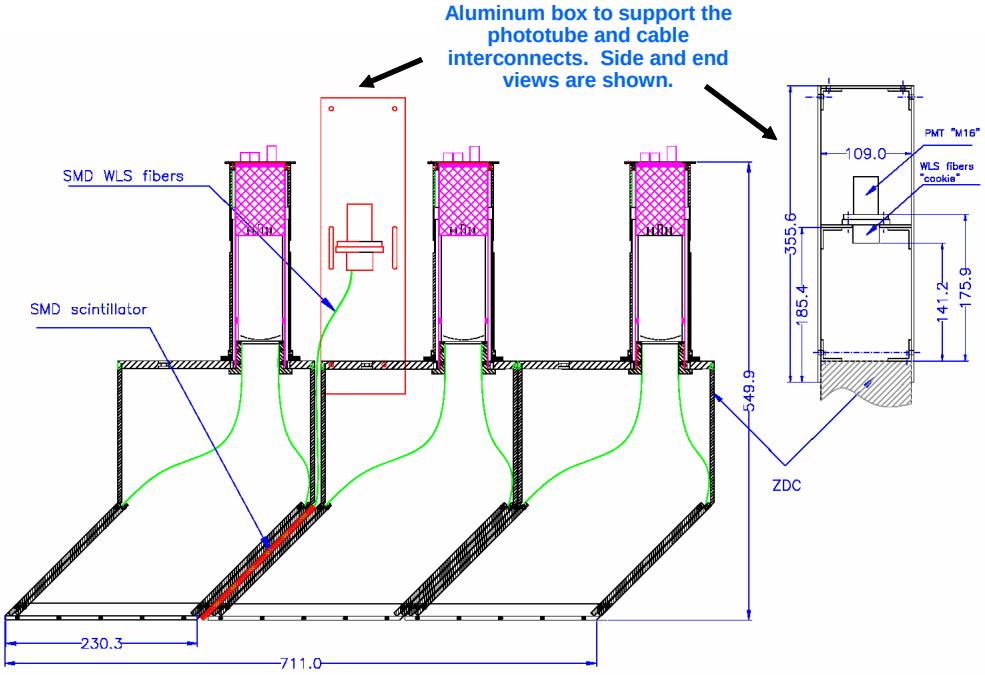

Figure 4.3: The SMD fits between the baseline ZDC modules.

The ZDC-SMDs were be placed between the first and second modules of the ZDCs (see Fig. 4.3).

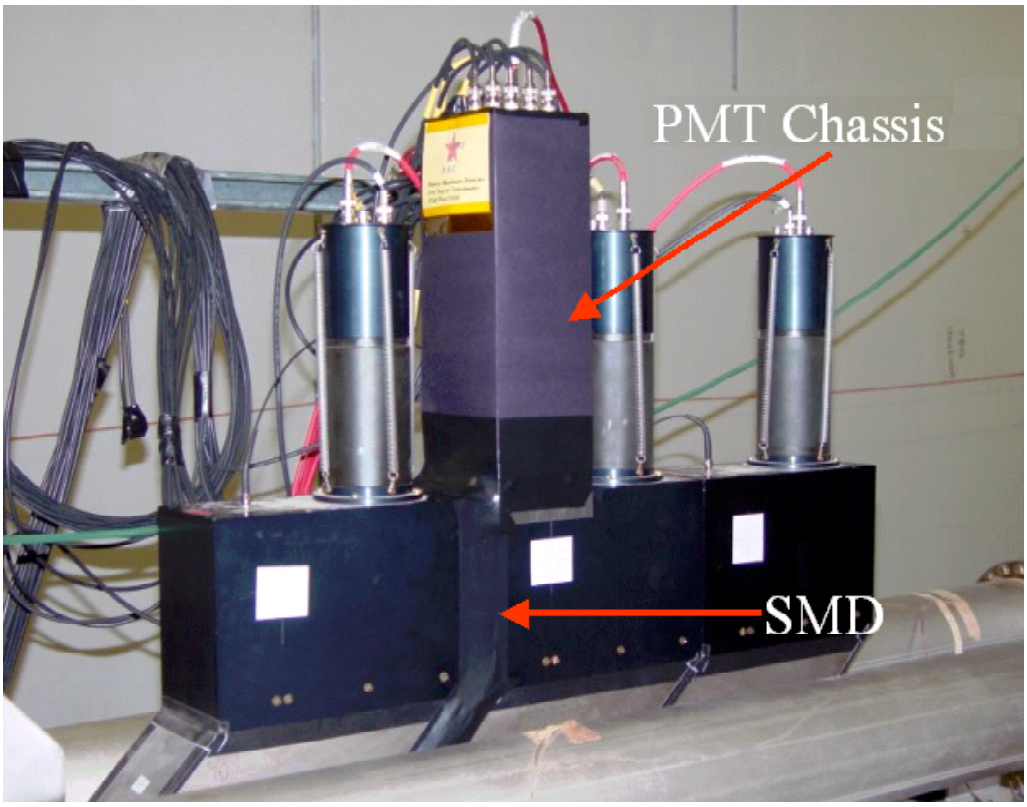

Figure 4.4: A ZDC-SMD module shown installed at STAR.

The SMD is an 8 channel by 7 channel hodoscope that sits directly on the face of the 2nd ZDC module (see Fig. 4.4). The hodoscope is made with strips of scintillating plastic that are laid out in an X-Y pattern, with 21 strips having their long axes vertical and 32 strips having their long axes horizontal. The cross section of each strip is approximately an equilateral triangle with an apex-to-base height of 7 mm; see Fig. 4.5. A hole running axially along the center of each triangle allows the insertion of a 0.83 mm wavelength-shifting fiber which is used to collect and transport the scintillation light. Individual triangular strips are wrapped with 50 μm aluminized mylar to optically isolate them from their neighbors. The wrapped scintillator strips are then epoxied between two G-10 sheets to form a plane. Each slat aligned in the vertical direction consists of three strips, and the corresponding three fibers are joined to make one channel, and routed to the face of a 16-channel segmented cathode phototube conveniently located in a chassis above the SMD. The slats aligned

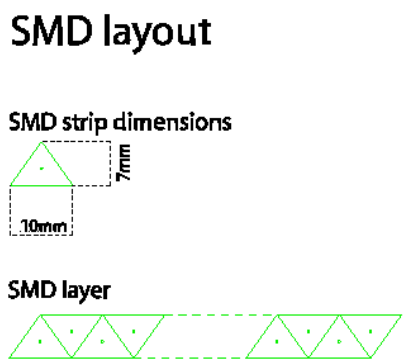

Figure 4.5: The SMD planes are built-up from scintillator strips with triangular cross section.

in the horizontal direction are each made up of four strips and their fibers. The overall dimensions of the hodoscope are approximately 2 cm $\times$ 11 cm $\times$ 18 cm.

The chassis to support the phototube is a simple aluminum structure that is designed to be sturdy and to bear the load of the phototube and the 16 cables hanging off the tube. It also supports the weight of the HV and BNC cables that go to the electronics racks on the STAR detector. The design of the chassis, hodoscope, and phototube mounting are identical to the design that was used in PHENIX by Sebastian White and his collaborators during run III.

The phototube is a 16-channel multi-anode PMT with a conventional resistive base (Hamamatsu H6568-10 [76]). The tube requires DC at -0.75 kV and it uses sixteen 50 ohm BNC cables for output. The sixteenth channel is a “sum” output. The electronics for the readout of the phototube were taken from spares for the STAR Central Trigger Barrel.

4.4 Impact on STAR

The possible impact on STAR was an important consideration at the time of the ZDC-SMD proposal. The primary change to the existing apparatus was that the 2nd and 3rd ZDC modules were moved away from STAR by about 2 cm in order to create a gap between modules 1 and 2. All other ZDC locations and the alignment with the beam stayed the same.

The gap was used for the installation of the SMD. The SMD itself is approximately 1.5 cm of

plastic and 2 mm of G-10 tilted on a 45 degree angle. This puts about 3 g/cm^2 of material in the path of neutrons coming from the interaction point. This amount of material is negligible compared to the $>$270 g/cm^2 of Tungsten and plastic in each ZDC module which comes before and after the SMD.

Perhaps more important is the fact that ZDC modules 2 and 3 have moved away from module 1. This means they will be sampling the neutron-induced showers at a slightly greater depth in the shower. This change was insignificant because the ZDCs are calibrated annually and the change in performance of the ZDCs was below the rms of the calibration error.

Chapter 5

Calibration and Performance of ZDC-SMD

The sensitivity and precision of measurements using the ZDC-SMD depend on the calibration. Apart from the absolute calibration (pedestal subtraction) and the relative calibration (gain correction), we also determine the location of the $p_t = 0$ point from time to time, and study the performance of the ZDC-SMD, such as the energy resolution and the beam position sensitivity.

5.1 Pedestal subtraction

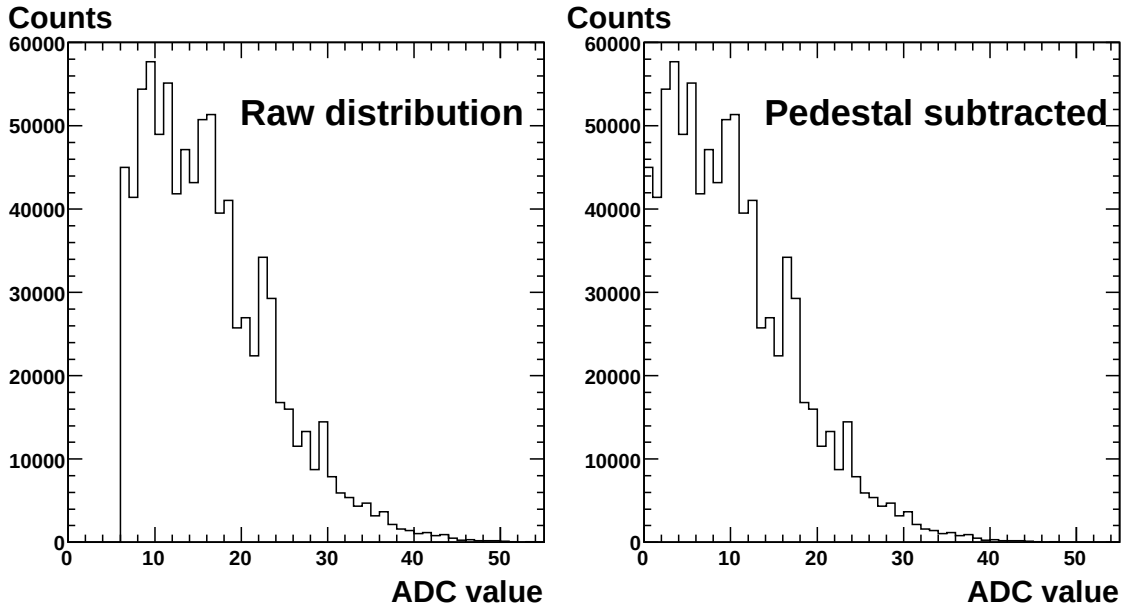

Figure 5.1: The signal distribution of a typical ZDC-SMD channel: raw distribution (left) and pedestal subtracted (right).

Each ZDC-SMD has 15 ADC (analog-to-digital converter) channels. The left panel of Fig. 5.1 shows the raw signal distribution of a typical ZDC-SMD channel, in which the measured ADC value

has a non-zero minimum due to electronic pedestal. The pedestal is a normal “feature” of any design of ADC with high sensitivity. It should not be dependent on the event type used for calibration, and is measured in the standard pedestal run in which all others STAR subsystem detectors are included. The right panel of Fig. 5.1 shows the pedestal-subtracted signal distribution of the same channel as in the left panel.

5.2 Gain correction

We need to adjust the gain parameters between different SMD channels so that the response of the detector becomes uniform. The following sections decribe how this has been accomplished.

5.2.1 Cosmic ray tests

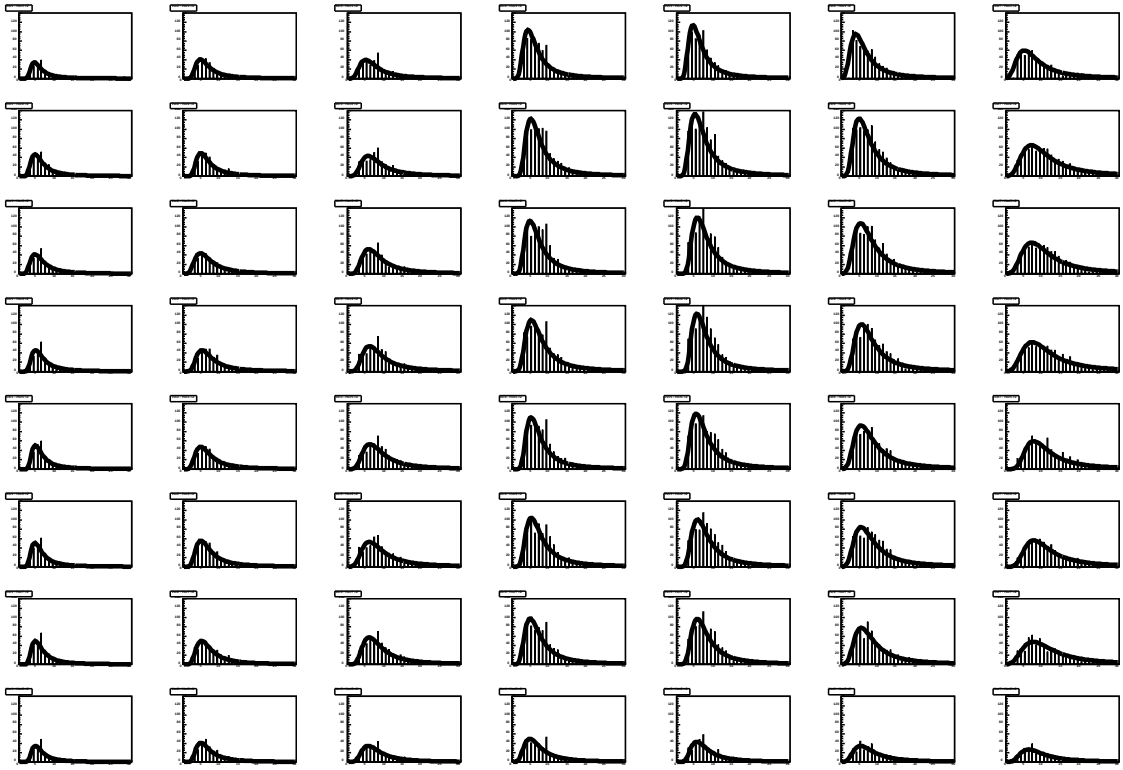

Figure 5.2: The signal distributions of vertical ZDC-SMD channels on the west side in a cosmic ray test, after pedestal subtraction.

Before the installation of each ZDC-SMD, cosmic ray tests were carried out. The SMD with

plastic scintillator cosmic ray trigger counters above and below it was placed in a black box, with the three modules aligned to detect vertical cosmic rays. The signal threshold of the trigger counters was set so that the coincidence rate of the two trigger counters was about 30 events per minute. Since the cosmic rays were uniformly distributed over the face of the ZDC-SMD, we expect the same integrated signal triggered in each strip.

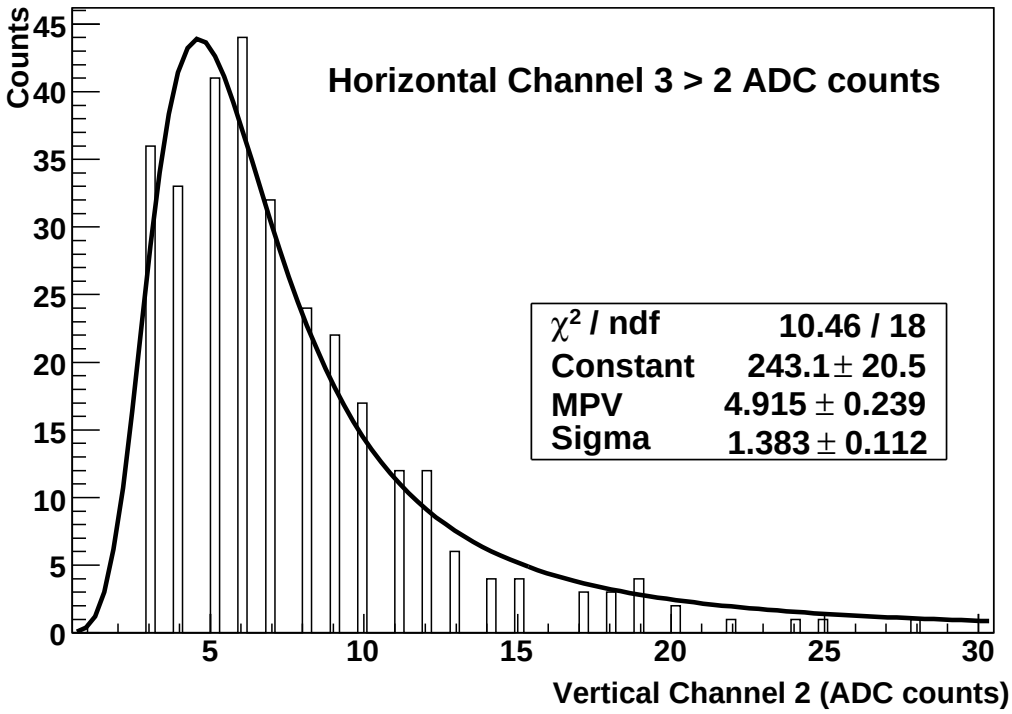

Figure 5.3: A typical panel in Fig. 5.2, located at (2, 3).

As shown in Fig. 5.2, we can divide the SMD into 56 (8×7) small squares, and examine the signal distribution of each channel on each square. For example, in Fig. 5.2 each column represents a vertical channel, and each row imposes a constraint from a horizontal channel. In each event, when the signal of the ith horizontal channel is bigger than 2 ADC counts, the signal of the jth vertical channel is filled into the distribution histogram at the square (i, j). Then each distribution can be fitted by a parametrized Landau function with the most probable value (MPV) representing

the peak. Fig. 5.3 shows a typical panel in Fig. 5.2, located at (2, 3). The vertical average of the MPVs over the 6 middle histograms (with the histograms at the top and bottom removed to reduce fluctuation) gives the mean response of each vertical channel, and the ratios between the responses of the channels serve as the gain correction factors.

5.2.2 Exponential fit

After the installation of the ZDC-SMD, there exist some known and possibly unknown factors that may influence the gain correction parameters of the slats. For example, the high voltage applied to the SMD PMTs needs to be independently optimized for each collision energy (62 GeV or 200 GeV) and collision system (AuAu or CuCu or pp), and a different voltage generally leads to a new set of parameters for gain correction. Also, the scintillating plastic of the SMD may show aging effects, and thus change the gain factors. So we need to repeat the relative calibration with trigger data after the physics run.

As seen in Fig. 5.1 and Fig. 5.2, the signal distribution of each channel has a high-ADC tail, a few σ away from the peak. This tail can be fitted with an exponential function $A \cdot \exp(-B \cdot \mathrm{ADC})$. We assume that if the response of the detector is uniform, then the high-ADC tail should have the same behavior for all the channels. Then after the exponential fitting, the parameter B can be used as the gain correction factor. Fig. 5.4 shows an example of the signal measured along the vertical dimension (8 channels) in a physics run. The left panel is the slat response before gain correction, and the right panel is after. On the whole, the signal is strongest in the middle channels, and decreases at both edges. This pattern corresponds to the energy deposition of spectator neutrons with Fermi momentum, as expected. By comparing the two panels, we see that after the gain correction, the slat response changes more smoothly with channel number than before the correction, especially for the 5th and 6th channels in this example.

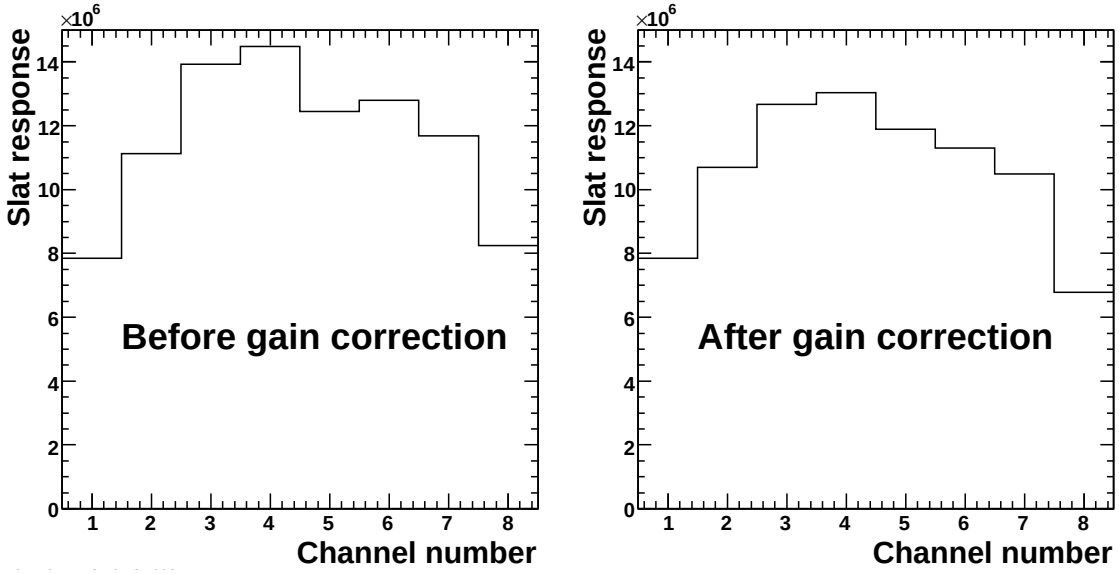

Figure 5.4: The slat response along ZDC-SMD's vertical dimension before (left panel) and after (right panel) gain correction.

5.3 Location of $p_t = 0$ point

As described in the last chapter, the shower produced by each neutron deposits light in more than one slat in each of the two layers of the ZDC-SMD, and for each event, we can sum the shower signals for the individual neutrons in each plane of slats. The mean position along each axis defines a centroid point in the transverse plane for each event. In this centroid calculation, we use the ADC value as the weight. The average of the centroids of many events gives us a location of the $p_t = 0$ point, i.e, the point where all the neutrons would hit the detector in the hypothetical limit where the beam spot is indefinitely small and the spectator neutrons are emitted with zero transverse momentum. In practice, the $p_t = 0$ point is usually different from the geometric center of the ZDC-SMD, and it keeps changing with time, since normal level of drifting of the RHIC beams can easily be detected by the ZDC-SMDs.

The calibration of $p_t = 0$ point has to be carried out more frequently than the pedestal run. Fig. 5.5 shows an example of the spatial distribution of $p_t = 0$ points in AuAu collisions at 62 GeV

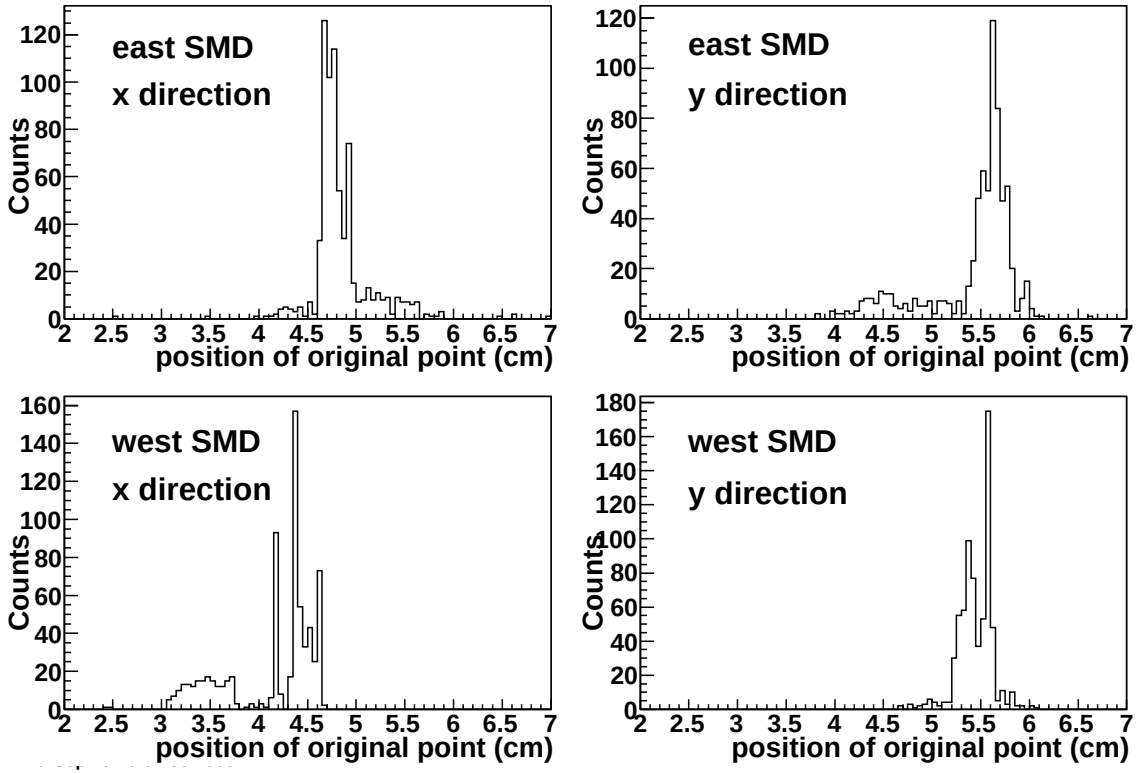

Figure 5.5: Spatial distribution of $p_t = 0$ point.

and 200 GeV in the year 2004. The dispersion of such a distribution is on the order of 1 cm, to be compared with the dimension of the ZDC-SMD itself (11cm$\times$18cm).

5.4 Energy deposition

Since the ZDC-SMD is sandwiched beween the first and second ZDC module, it can be regarded as a slice of the baseline ZDC, and thus the total energy deposited in the ZDC-SMD should be proportional to that in the ZDC modules. Fig. 5.6 shows the energy correlation between ZDC-SMD and ZDC, for both east and west sides. In both cases, the correlation can be fitted with a straight line. With this plot, we can also test for saturation in the SMD channels. If the correlation curve bends down at high ZDC signal, it may be a sign of SMD saturation, in which case we need to lower the high voltage for the ZDC-SMD until the correlation curve becomes straight.

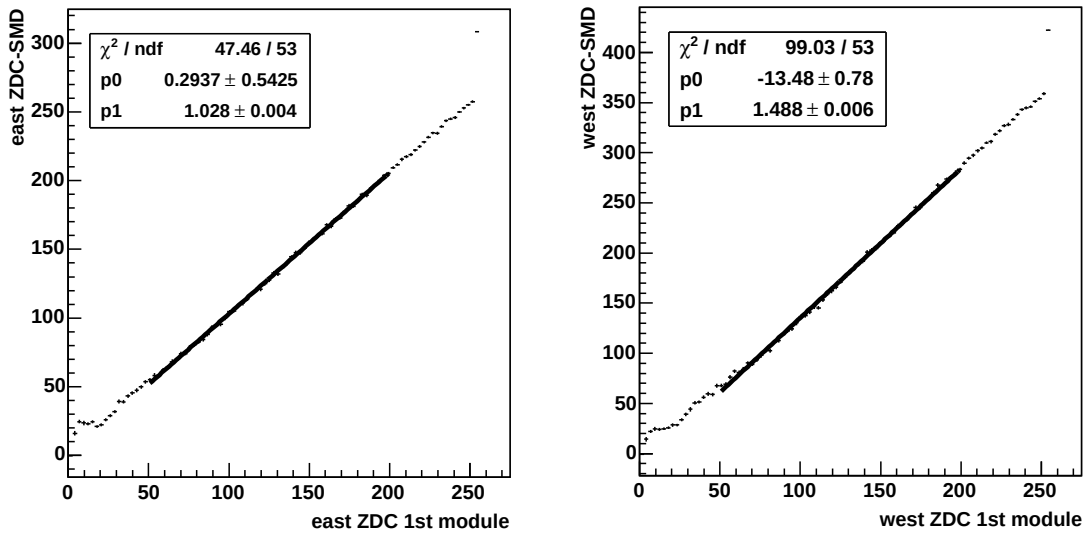

Figure 5.6: The energy correlation between ZDC-SMD and ZDC.

From the fitting in Fig. 5.6, we can parameterize the energy correlation between the ZDC-SMD and the ZDC with

$$E_{\text{ZDC-SMD}} = A + B \cdot E_{\text{ZDC}} \tag{5.1}$$

where $E_{\text{ZDC-SMD}}$ and E_{ZDC} are the total energy deposition in the ZDC-SMD and the ZDC, respectively, and A and B are the fitting parameters. Then we can define an energy ratio R_E between the ZDC-SMD and the ZDC with

$$R_E = ((E_{\text{ZDC-SMD}} - A)/B - E_{\text{ZDC}})/E_{\text{ZDC}} \tag{5.2}$$

The distribution of this ratio is plotted in Fig. 5.7, where the labels on the horizontal axes are simplified for clarity. If we fit the distribution with a Gaussian function, the σ is considered to be the relative energy resolution between the ZDC-SMD and the ZDC. This relative resolution is about 35% for both east and west sides, and this is quite reasonable if we note that the energy resolution of the ZDC itself is about 20% [64]. If we assume that the energy correlation between the ZDC-SMD and the ZDC is solely due to the fact that the ZDC-SMD and the ZDC respond to the same

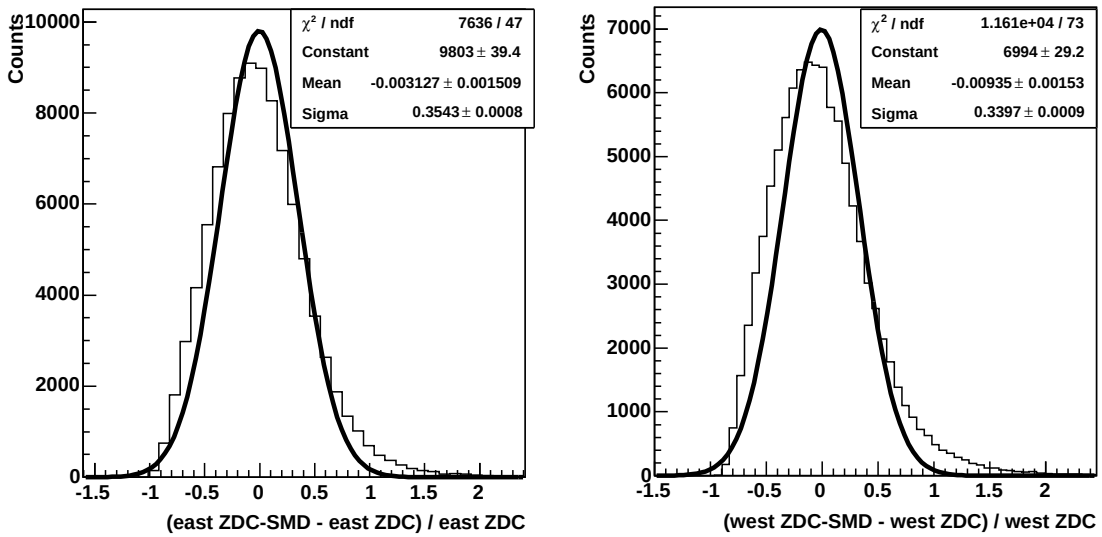

Figure 5.7: The relative energy resolution between the ZDC-SMD and the ZDC.

energy source (spectator neutrons), then a rough estimation gives about 29% energy resolution for ZDC-SMD ($\sqrt{(0.35)^2 - (0.20)^2} = 0.287$).

5.5 Beam position sensitivity

As mentioned in earlier sections, the beam is not stable, and the ZDC-SMD centroid moves from minute to minute, as well as over longer time scales. By plotting the centroid position against event sequence (or time), we can have some idea of the beam position sensitivity of the ZDC-SMD. Fig. 5.8 shows the mean of centroid positions of every 10000 events against event sequence, for both east and west SMDs, for both x and y directions.

In Fig. 5.8, the point-to-point fluctuation is at the level of 100 μm for each panel, which corresponds to the beam position sensitivity. From this plot, we can also study the beam movement. For example, between event 100k and event 140k, east and west SMDs share the same pattern in the x direction, with the beam position going from positive to negative. Since the local coordinates used in the east and west SMDs have opposite x direction, we conclude that the beam was rotating in x

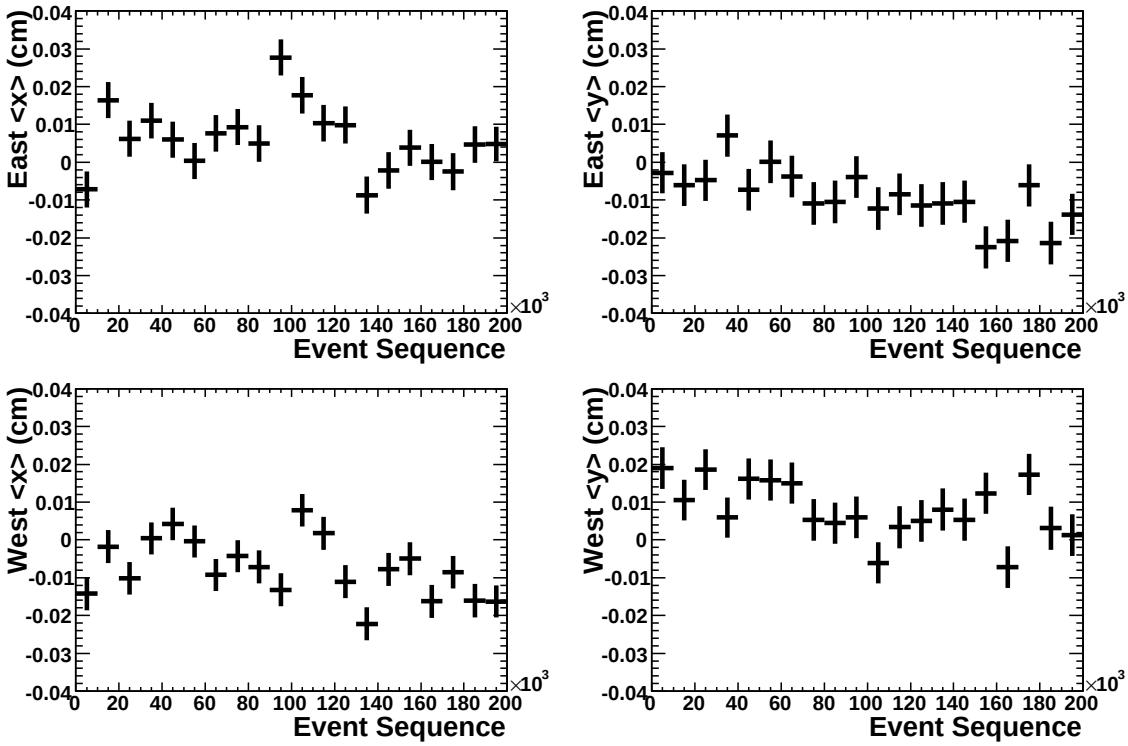

Figure 5.8: The beam position against time.

direction during that time period, with the vertex position roughly constant. For another example, between 50k and 90k, the beam position shows the same behavior in the y direction for both east and west SMDs. This should be related to a shift of the beam in the y direction.

Chapter 6

Estimation of the Reaction Plane

The reaction plane is defined by the impact parameter vector and the beam direction, and plays an important role in event-by-event analysis in high-energy heavy-ion collisions. The estimated reaction plane we call the event plane. In this chapter, the estimation of the reaction plane is discussed, especially the 1st-order event plane from spectator bounce-off. The application of the 1st-order event plane in anisotropic flow analysis is studied.

6.1 Estimation of the reaction plane

Usually the event plane can be determined independently for each harmonic of the anisotropic flow. [28] Thus we have the 1st-order event plane if it is determined from directed flow, and the 2nd-order event plane, based on elliptic flow.

6.1.1 Track-based and hit-based

In the STAR experiment, detectors can be classified into two categories: track-based detectors such as the TPC and FTPCs, and hit-based detectors like the ZDC-SMD. Correspondingly, the estimation of the reaction plane has different approaches, depending on which detector is involved.

In track-based detectors, the event plane vector $\overrightarrow{Q}_n$ and the event plane angle ψ_n from the nth harmonic of the particle's azimuthal distribution are defined by the equations [28]:

$$Q_n \cos(n\psi_n) = X_n = \sum_i w_i \cos(n\varphi_i) \tag{6.1}$$

$$Q_n \sin(n\psi_n) = Y_n = \sum_i w_i \sin(n\varphi_i) \tag{6.2}$$

or

$$\psi_n = \left(\tan^{-1} \frac{\sum_i w_i \sin(n\varphi_i)}{\sum_i w_i \cos(n\varphi_i)} \right) \tag{6.3}$$

where φ_i denotes the azimuthal angle of the ith particle (a track detected by a track-based detector) in the event plane determination, and the w_i are weights, optimized to make the reaction plane resolution as good as possible. Sometimes we can optimize the event plane estimation by selecting the particles of one particular type, or weighting with transverse momentum of the particles, etc. In general, the weights for the odd and even harmonic planes are different. Optimal weights are discussed in footnote 2 of Ref. [77]. For symmetric collisions like Au +Au or Cu +Cu, reflection symmetry requires that particle distributions should be the same in the forward and backward hemispheres of the center of mass, if the azimuthal angles of all particles in one of the hemispheres are shifted by π. Thus, for the odd harmonics, the signs of the weights are opposite in the different hemispheres, while for the even harmonics, the signs of the weights are the same. Note that the nth-order event plane angle ψ_n is in the range $0 \leqslant \psi_n < 2\pi/n$. For the case of $n = 1$, Eqs. 6.1-6.3 are equivalent to obtaining ψ_1 for number flow from Ref. [53]:

$$\overrightarrow{Q} = \sum w \cdot \overrightarrow{p}_t / |p_t| \tag{6.4}$$

where the sum is over all the particles. The case of $n = 2$ is equivalent to the event plane determined from the transverse sphericity matrix [24].

In a hit-based detector, if the detector elements have a cylindrically symmetric arrangement around the beam axis, then the event plane vector $\overrightarrow{Q}_n$ and the event plane angle ψ_n can be formulated in the same way as Eqs. 6.1-6.3, except that now φ_i denotes the fixed azimuthal angle of the ith element of in the detector, and the w_i are the energy depositions (ADC signals) in the ith element. In the case of the ZDC-SMD, since it is located at $|\eta| > 6.3$ where directed flow is dominant over other harmonics, we only consider the 1st-order event plane. In each ZDC-SMD (east and west), the

1st-order event plane vector $\overrightarrow{Q}$ and the 1st-order event plane angle ψ are defined by the equations:

$$Q\cos\psi = X = \sum_{i=1}^{7} w_i x_i \tag{6.5}$$

$$Q\sin\psi = Y = \sum_{i=1}^{8} w_i y_i \tag{6.6}$$

or

$$\psi = \left(\tan^{-1} \frac{\sum_{i=1}^{7} w_i x_i}{\sum_{i=1}^{8} w_i y_i} \right) \tag{6.7}$$

where x_i and y_i are the fixed positions (with the $p_t = 0$ point subtracted) for the 7 vertical slats and the 8 horizontal slats, respectively. Note that the term "vertical slat" means a slat with its long axis vertical; then of course this slat provides information only about the horizontal position of the shower. In practice, the w_i are calculated from ADC_i (the signal in the ith slat, either vertical or horizontal) in the following way:

$$w_i = \mathrm{ADC}_i / \left(\sum_{i=1}^{7 \text{ or } 8} \mathrm{ADC}_i \right) \tag{6.8}$$

As there are ZDC-SMDs on both the east and west sides of the STAR intersection region, and each of them can determine a 1st-order event plane, we consider the event plane obtained from a single ZDC-SMD to be a sub-event plane, and the combination of the east and west event plane vectors provides the full event plane.

6.1.2 Event plane distribution

The reaction plane in heavy-ion collisions should be randomly distributed. However, the rectangular shape of the ZDC-SMD leads to an uneven distribution of the 1st-order event plane, as shown in Fig. 6.1. Such raw event planes can not be applied directly in a flow analysis, since they have some preference in the orientation, which will introduce non-flow correlations. One way to solve

this problem is to apply weights to events with different event plane angles. The weight can be determined with the inverse of the bin content in the raw event plane distribution, so that the events with more probable event plane angles get less weight, and vice versa.

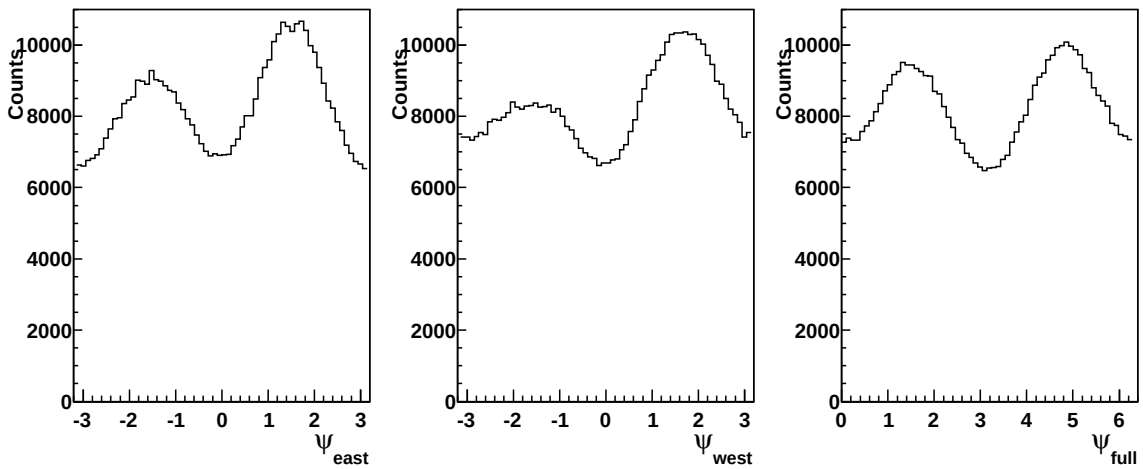

Figure 6.1: Raw distributions of the 1st-order event planes from the ZDC-SMDs: east sub-event plane (left panel), west sub-event plane (middle panel) and full event plane (right panel).

Another way is to make corrections to the event plane angle itself, and flatten the event plane distribution. The raw event plane distribution $\frac{dN}{d\psi}$ can be expanded in a Fourier series:

$$\frac{dN}{d\psi} = \frac{a_0}{2} + \sum_n (a_n \cos n\psi + b_n \sin n\psi) \tag{6.9}$$

where

$$\begin{aligned} a_n &= \frac{1}{\pi}\int_{-\pi}^{\pi} \frac{dN}{d\psi} \cdot \cos n\psi \cdot d\psi \qquad n = 0, 1, 2... \\ b_n &= \frac{1}{\pi}\int_{-\pi}^{\pi} \frac{dN}{d\psi} \cdot \sin n\psi \cdot d\psi \qquad n = 1, 2, 3... \end{aligned} \tag{6.10}$$

We make a new angle ψ' after adding a correction term $\Delta\psi$ to the raw event plane angle ψ.

$$\psi' = \psi + \Delta\psi = \psi + \sum_n (A_n \cos n\psi + B_n \sin n\psi) \tag{6.11}$$

By requring the new angle to be uniformly distributed, we have

$$\frac{dN}{d\psi'} = \frac{N}{2\pi} = \frac{a_0}{2} \tag{6.12}$$

Now the raw distribution can be rewritten as

$$\frac{dN}{d\psi} = \frac{dN}{d\psi'} \cdot \frac{d\psi'}{d\psi} = \frac{a_0}{2} \cdot (1 + \sum_n (-n \cdot A_n \sin n\psi + n \cdot B_n \cos n\psi)) \tag{6.13}$$

Comparing Eq. 6.9 and Eq. 6.13, we can evaluate the coefficients from the raw distribution

$$\begin{aligned} A_n &= -\frac{2}{n} \cdot \frac{b_n}{a_0} = -\frac{2}{n}\langle \sin n\psi \rangle \\ B_n &= -\frac{2}{n} \cdot \frac{a_n}{a_0} = \frac{2}{n}\langle \cos n\psi \rangle \end{aligned} \tag{6.14}$$

Thus the corrected event plane angle is

$$\psi' = \psi + \sum_n \frac{2}{n}(-\langle \sin n\psi \rangle \cos n\psi + \langle \cos n\psi \rangle \sin n\psi) \tag{6.15}$$

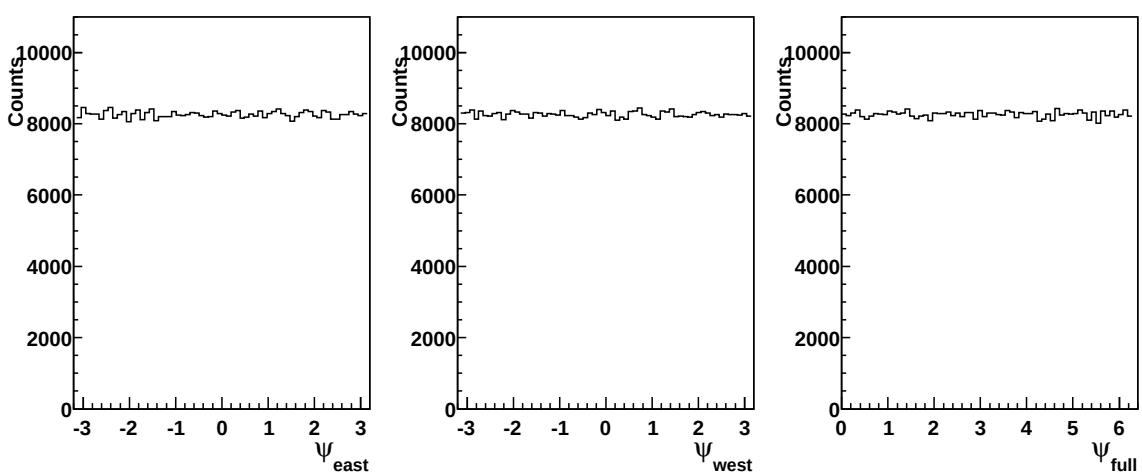

Figure 6.2: Distributions of the flattened 1st-order event planes from the ZDC-SMDs: east sub-event plane (left panel), west sub-event plane (middle panel) and full event plane (right panel).

In practice, we flatten the event plane distribution up to the fourth harmonic ($n = 4$), as shown in Fig. 6.2. Note that due to the small values of A_n and B_n (typically of the order of a few percent), such a flattening of the distribution does not have any effect on the event plane resolution. It can also be shown that the same flattening procedure removes possible trigger biases (due to imperfect calibration, dead channels, or any other asymmetry) at least up to the second order. [78]

6.1.3 Event plane resolution

The event plane resolution was introduced in Chapter 2 as the denominator $\langle\cos[km(\psi_m - \psi_r)]\rangle$ in Eq. 2.5. For the case of the 1st-order event plane from the ZDC-SMD, $m = 1$ and the event plane resolution for the k-th harmonic calculation reduces to $\langle\cos[k(\psi - \psi_r)]\rangle$. Since we have two independent sub-event planes from the two ZDC-SMDs, the correlation between these two event plane angles can be expressed as

$$\langle\cos[k(\psi_{\text{east}} - \psi_{\text{west}})]\rangle = \langle\cos[k(\psi_{\text{east}} - \psi_r)]\rangle \cdot \langle\cos[k(\psi_{\text{west}} - \psi_r)]\rangle \tag{6.16}$$

If we assume that the two sub-event planes have the same resolution, then the sub-event plane resolution is

$$\begin{aligned} \langle\cos[k(\psi_{\text{sub}} - \psi_r)]\rangle &= \langle\cos[k(\psi_{\text{east}} - \psi_r)]\rangle \\ &= \langle\cos[k(\psi_{\text{west}} - \psi_r)]\rangle \\ &= \sqrt{\langle\cos[k(\psi_{\text{east}} - \psi_{\text{west}})]\rangle} \end{aligned} \tag{6.17}$$

The term inside the square-root should always be positive, if the sub-events are correlated. However, for small amounts of flow, fluctuations and/or nonflow correlations can cause this term to be negative. When the sub-event plane resolution is low, we can approximate the full event plane resolution as

$$\langle\cos[k(\psi_{\text{full}} - \psi_r)]\rangle \approx \sqrt{2} \cdot \langle\cos[k(\psi_{\text{sub}} - \psi_r)]\rangle \tag{6.18}$$

A more detailed and accurate estimation of the event plane resolution is stated in Ref. [28], where I_ν, the modified Bessel function of order υ is employed:

$$\langle\cos[k(\psi_{\text{full}} - \psi_r)]\rangle = \frac{\sqrt{\pi}}{2\sqrt{2}}\chi \exp(-\chi^2/4) \cdot [I_{(k-1)/2}(\chi^2/4) + I_{(k+1)/2}(\chi^2/4)] \tag{6.19}$$

where χ can be obtained from the sub-event plane resolution as shown in Fig. 1 in Ref. [28].

Centrality	62 GeV Au +Au	200 GeV Au +Au	200 GeV Cu +Cu
$70\% - 80\%$	0.179 ± 0.005	0.296 ± 0.003	
$60\% - 70\%$	0.185 ± 0.004	0.348 ± 0.003	
$50\% - 60\%$	0.176 ± 0.005	0.382 ± 0.002	0.135 ± 0.007
$40\% - 50\%$	0.167 ± 0.005	0.397 ± 0.002	0.139 ± 0.007
$30\% - 40\%$	0.138 ± 0.006	0.390 ± 0.002	0.150 ± 0.006
$20\% - 30\%$	0.110 ± 0.008	0.365 ± 0.002	0.130 ± 0.008
$10\% - 20\%$	0.081 ± 0.010	0.309 ± 0.003	0.105 ± 0.009
$5\% - 10\%$		0.220 ± 0.006	
$0 - 5\%$		0.127 ± 0.011	

Table 6.1: The resolution of the 1st-order full event plane provided by the ZDC-SMDs, as determined from the sub-event correlation between east and west SMDs. The errors in the table are statistical.

Table 6.1 shows the resolution of the 1st-order full event plane provided by the ZDC-SMDs, as determined from the sub-event correlation between east and west SMDs. In 200 GeV Au +Au collisions, the resolution is between 30% and 40% for most centralities, which corresponds to the best case in the flow simulation result in Fig. 4.1 (spectator $v_1 = 20\%$ and neutron multiplicity $= 30$). In 62 GeV Au +Au and 200 GeV Cu +Cu collisions, the lower resolutions correspond to the case where spectator $v_1 = 20\%$ and neutron mulplicity $= 5$, for different reasons. In 62 GeV Au +Au collisions, the beam energy is one-third that of 200 GeV collisions, so neutrons with Fermi momentum disperse in a solid angle about nine times as big as in 200 GeV collisions and many of them miss the ZDC transverse plane. In 200 GeV Cu +Cu collisions, since Cu is much smaller than Au, naturally a smaller number of spectator neutrons appear in the beam direction. Note that in some cases in Table 6.1 , the resolution can not be obtained because the term inside the square-root in Eq. 6.17 becomes negative. The resolution for elliptic flow calculation or even higher order harmonics can be calculated with Eq. 6.19 in a similiar way.

6.2 The 1st-order event plane in flow analysis

There are several physics areas where the ZDC-SMD can contribute, as mentioned in Chapter 4. In this work, we focus on the application of the 1st-order event plane in flow analysis.

6.2.1 Terms for east, west, and for vertical and horizontal directions in the transverse plane

Each ZDC-SMD provides us with a 1st-order sub-event plane, and the flow components can be evaluated as:

$$\begin{aligned} v_{n_\text{sub}} &= \frac{\langle \cos[n(\varphi - \psi_{\text{sub}})] \rangle}{\langle \cos[n(\psi_{\text{sub}} - \psi_r)] \rangle} \\ &= \frac{\langle \cos[n(\varphi - \psi_{\text{sub}})] \rangle}{\sqrt{\langle \cos[n(\psi_{\text{east}} - \psi_{\text{west}})] \rangle}} \\ &= \frac{\langle \cos n\varphi \, \cos n\psi_{\text{sub}} + \sin n\varphi \, \sin n\psi_{\text{sub}} \rangle}{\sqrt{\langle \cos n\psi_{\text{east}} \cos n\psi_{\text{west}} + \sin n\psi_{\text{east}} \sin n\psi_{\text{west}} \rangle}} \end{aligned} \tag{6.20}$$

where ψ_{sub} stands for either ψ_{east} or ψ_{west}. Since the ZDC-SMD has a rectangular shape, we must treat separately the x- and y- directions, represented by the cos- and sin-terms, respectively, in Eq. 6.20. Thus assuming that the sin- and cos-terms are symmetric, we break down Eq. 6.20 into 4 terms:

$$\begin{aligned} v_{n_\text{east}_\cos} &= \frac{2\langle \cos n\varphi \, \cos n\psi_{\text{east}} \rangle}{\sqrt{2\langle \cos n\psi_{\text{east}} \cos n\psi_{\text{west}} \rangle}} \\ v_{n_\text{east}_\sin} &= \frac{2\langle \sin n\varphi \, \sin n\psi_{\text{east}} \rangle}{\sqrt{2\langle \sin n\psi_{\text{east}} \sin n\psi_{\text{west}} \rangle}} \\ v_{n_\text{west}_\cos} &= \frac{2\langle \cos n\varphi \, \cos n\psi_{\text{west}} \rangle}{\sqrt{2\langle \cos n\psi_{\text{east}} \cos n\psi_{\text{west}} \rangle}} \\ v_{n_\text{west}_\sin} &= \frac{2\langle \sin n\varphi \, \sin n\psi_{\text{west}} \rangle}{\sqrt{2\langle \sin n\psi_{\text{east}} \sin n\psi_{\text{west}} \rangle}} \end{aligned} \tag{6.21}$$

The average of the 4 terms gives the final result for v_n. There are several assumptions underlying the definitions of the 4 terms in Eq. 6.21. In reality, we need to apply some corrections to compensate for ideal-case assumptions. The advantage of using the 4 terms with the sub-event planes over the standard approach with the full event plane is that we can apply corrections to each of the 4 terms separately according to the detector performance and lessen the systematic errors.

6.2.2 Correction to sub-event plane resolution

In Eq. 6.17, we assume that the two sub-event planes have the same resolution, which is not completely true. The two ZDC-SMDs are identical in design and construction, but in practice, there are differences due to PMT characteristics and the different tune of the two beams at RHIC. To compensate for the difference between east and west ZDC-SMDs, we can separate the sub-event plane resolution for the east and west SMD by introducing a third event plane from the TPC or FTPC(ψ^*):

$$
\begin{aligned}
& \langle \cos[n(\psi_{\text{east}} - \psi_r)] \rangle \\
= & \sqrt{\frac{\langle \cos[n(\psi_{\text{east}} - \psi_r)] \cdot \cos[n(\psi_{\text{west}} - \psi_r)] \rangle \cdot \langle \cos[n(\psi_{\text{east}} - \psi_r)] \cdot \cos[n(\psi^* - \psi_r)] \rangle}{\langle \cos[n(\psi_{\text{west}} - \psi_r)] \cdot \cos[n(\psi^* - \psi_r)] \rangle}} \\
= & \sqrt{\frac{\langle \cos[n(\psi_{\text{east}} - \psi_{\text{west}})] \rangle \cdot \langle \cos[n(\psi_{\text{east}} - \psi^*)] \rangle}{\langle \cos[n(\psi_{\text{west}} - \psi^*)] \rangle}} \\
= & \sqrt{\frac{2\langle \cos n\psi_{\text{east}} \cos n\psi_{\text{west}} \rangle \cdot \langle \cos n\psi_{\text{east}} \cos n\psi^* \rangle}{\langle \cos n\psi_{\text{west}} \cos n\psi^* \rangle}} \qquad (6.22) \\
= & \sqrt{\frac{2\langle \sin n\psi_{\text{east}} \sin n\psi_{\text{west}} \rangle \cdot \langle \sin n\psi_{\text{east}} \sin n\psi^* \rangle}{\langle \sin n\psi_{\text{west}} \sin n\psi^* \rangle}} \qquad (6.23)
\end{aligned}
$$

In the same way,

$$
\begin{aligned}
& \langle \cos[n(\psi_{\text{west}} - \psi_r)] \rangle \\
= & \sqrt{\frac{2\langle \cos n\psi_{\text{east}} \cos n\psi_{\text{west}} \rangle \cdot \langle \cos n\psi_{\text{west}} \cos n\psi^* \rangle}{\langle \cos n\psi_{\text{east}} \cos n\psi^* \rangle}} \qquad (6.24) \\
= & \sqrt{\frac{2\langle \sin n\psi_{\text{east}} \sin n\psi_{\text{west}} \rangle \cdot \langle \sin n\psi_{\text{west}} \sin n\psi^* \rangle}{\langle \sin n\psi_{\text{east}} \sin n\psi^* \rangle}} \qquad (6.25)
\end{aligned}
$$

Then the 4 corrected terms become:

$$
\begin{aligned}
v_{n_\text{east}_\cos} &= \frac{2\langle\cos n\varphi\cos n\psi_{\text{east}}\rangle}{\sqrt{2\langle\cos n\psi_{\text{east}}\cos n\psi_{\text{west}}\rangle}}\cdot\sqrt{\frac{\langle\cos n\psi_{\text{west}}\cos n\psi^{*}\rangle}{\langle\cos n\psi_{\text{east}}\cos n\psi^{*}\rangle}} \\
v_{n_\text{east}_\sin} &= \frac{2\langle\sin n\varphi\sin n\psi_{\text{east}}\rangle}{\sqrt{2\langle\sin n\psi_{\text{east}}\sin n\psi_{\text{west}}\rangle}}\cdot\sqrt{\frac{\langle\sin n\psi_{\text{west}}\sin n\psi^{*}\rangle}{\langle\sin n\psi_{\text{east}}\sin n\psi^{*}\rangle}} \\
v_{n_\text{west}_\cos} &= \frac{2\langle\cos n\varphi\cos n\psi_{\text{west}}\rangle}{\sqrt{2\langle\cos n\psi_{\text{east}}\cos n\psi_{\text{west}}\rangle}}\cdot\sqrt{\frac{\langle\cos n\psi_{\text{east}}\cos n\psi^{*}\rangle}{\langle\cos n\psi_{\text{west}}\cos n\psi^{*}\rangle}} \\
v_{n_\text{west}_\sin} &= \frac{2\langle\sin n\varphi\sin n\psi_{\text{west}}\rangle}{\sqrt{2\langle\sin n\psi_{\text{east}}\sin n\psi_{\text{west}}\rangle}}\cdot\sqrt{\frac{\langle\sin n\psi_{\text{east}}\sin n\psi^{*}\rangle}{\langle\sin n\psi_{\text{west}}\sin n\psi^{*}\rangle}}
\end{aligned}
\tag{6.26}
$$

Note that the correction terms for $v_{n_\text{east}_\cos(\sin)}$ and $v_{n_\text{west}_\cos(\sin)}$ are just the inverse of each other. So the effect of this correction is to make one term bigger and make its counterpart smaller, so that they are closer to each other since all the 4 terms should ideally give the same physical result.

6.2.3 Acceptance correction

In Eq. 6.21, we assume that the φ distribution is isotropic (the ψ_{sub} distribution is already flattened) so that $\cos n\varphi\cos n\psi_{\text{sub}}$ and $\sin n\varphi\sin n\psi_{\text{sub}}$ have the same contribution to v_n. In general, from Eq. 2.1 we have

$$
\frac{d^2N}{d\varphi\cdot d\psi_r}\sim 1+\sum_{k=1}^{\infty}2v_k\cos[k(\varphi-\psi_r)] \tag{6.27}
$$

Then

$$
\begin{aligned}
\langle \cos n\varphi \cos n\psi_r \rangle &= \frac{\int \cos n\varphi \cos n\psi_r \cdot dN}{N} \\
&= \frac{\int\int \cos n\varphi \cos n\psi_r \cdot \dfrac{d^2N}{d\varphi \cdot d\psi_r} \cdot d\varphi \cdot d\psi_r}{\int \dfrac{d^2N}{d\varphi \cdot d\psi_r} \cdot d\varphi \cdot d\psi_r} \\
&= \int\limits_{\text{acc}} \cos n\varphi \cos n\psi_r \cdot \frac{d\varphi}{2\pi} \int\limits_{2\pi} [1 + \sum_{k=1}^{\infty} 2v_k \cos[k(\varphi - \psi_r)] \cdot \frac{d\psi_r}{2\pi} \\
&= \int\limits_{\text{acc}} \cos n\varphi \cos n\psi_r \cdot \frac{d\varphi}{2\pi} \int\limits_{2\pi} \sum_{k=1}^{\infty} 2v_k (\cos k\varphi \cos k\psi_r + \sin k\varphi \sin k\psi_r) \cdot \frac{d\psi_r}{2\pi} \\
&= 2v_n \int\limits_{\text{acc}} \cos^2 n\varphi \cdot \frac{d\varphi}{2\pi} \int\limits_{2\pi} \cos^2 n\psi_r \cdot \frac{d\psi_r}{2\pi} \\
&= v_n \int\limits_{\text{acc}} \cos^2 n\varphi \cdot \frac{d\varphi}{2\pi} \\
&= v_n \langle \cos^2 n\varphi \rangle \qquad (6.28)
\end{aligned}
$$

where $\int\limits_{\text{acc}}$ represents the integral over the acceptance of a detector. In the same way, we have

$$\langle \sin n\varphi \sin n\psi_r \rangle = v_n \langle \sin^2 n\varphi \rangle \qquad (6.29)$$

If a detector has perfect acceptance, then the averages in the r.h.s. of Eq. 6.28 and 6.29 become $1/2$, and Eq. 6.21 will hold. However, as shown in Fig. 6.3, the averages of the sin- and cos-terms can differ from $1/2$, especially at the pseudorapidities covered by the FTPCs. Thus the 4 terms need

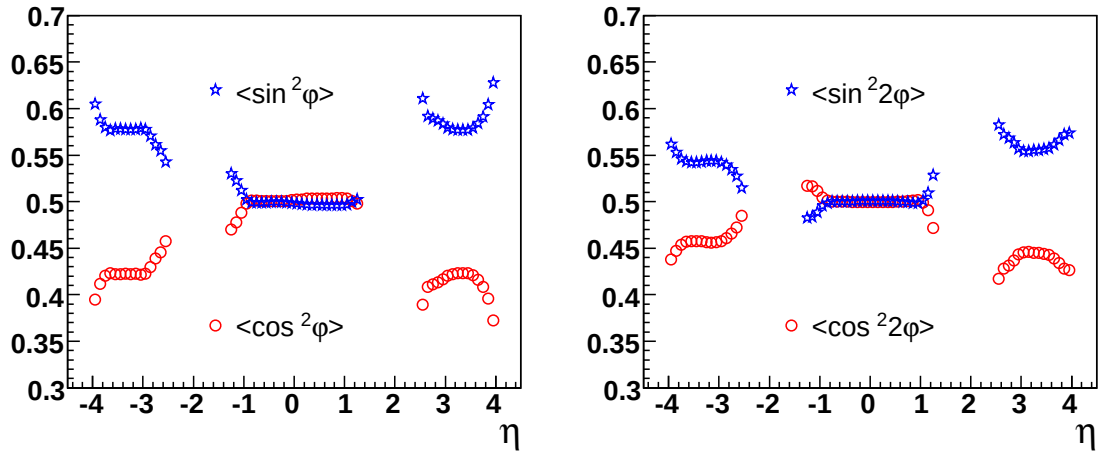

Figure 6.3: Acceptance correction terms for directed flow (left panel) and elliptic flow (right panel) in the TPC and FTPCs.

to be further corrected:

$$
\begin{aligned}
v_{n_\text{east}_\cos} &= \frac{1}{\langle \cos^2 n\varphi \rangle} \cdot \frac{\langle \cos n\varphi \cos n\psi_{\text{east}} \rangle}{\sqrt{2\langle \cos n\psi_{\text{east}} \cos n\psi_{\text{west}} \rangle}} \cdot \sqrt{\frac{\langle \cos n\psi_{\text{west}} \cos n\psi^* \rangle}{\langle \cos n\psi_{\text{east}} \cos n\psi^* \rangle}} \\
v_{n_\text{east}_\sin} &= \frac{1}{\langle \sin^2 n\varphi \rangle} \cdot \frac{\langle \sin n\varphi \sin n\psi_{\text{east}} \rangle}{\sqrt{2\langle \sin n\psi_{\text{east}} \sin n\psi_{\text{west}} \rangle}} \cdot \sqrt{\frac{\langle \sin n\psi_{\text{west}} \sin n\psi^* \rangle}{\langle \sin n\psi_{\text{east}} \sin n\psi^* \rangle}} \\
v_{n_\text{west}_\cos} &= \frac{1}{\langle \cos^2 n\varphi \rangle} \cdot \frac{\langle \cos n\varphi \cos n\psi_{\text{west}} \rangle}{\sqrt{2\langle \cos n\psi_{\text{east}} \cos n\psi_{\text{west}} \rangle}} \cdot \sqrt{\frac{\langle \cos n\psi_{\text{east}} \cos n\psi^* \rangle}{\langle \cos n\psi_{\text{west}} \cos n\psi^* \rangle}} \\
v_{n_\text{west}_\sin} &= \frac{1}{\langle \sin^2 n\varphi \rangle} \cdot \frac{\langle \sin n\varphi \sin n\psi_{\text{west}} \rangle}{\sqrt{2\langle \sin n\psi_{\text{east}} \sin n\psi_{\text{west}} \rangle}} \cdot \sqrt{\frac{\langle \sin n\psi_{\text{east}} \sin n\psi^* \rangle}{\langle \sin n\psi_{\text{west}} \sin n\psi^* \rangle}}
\end{aligned}
\tag{6.30}
$$

The above corrections apply to both track-based detectors and hit-based detectors, except that in hit-based detectors like CTB, the φ angle is fixed for each slat, and the average is weighted with the slat signals.

6.2.4 Granularity correction in hit-based detectors

Since hit-based detectors are made of elements with finite azimuthal width, we have to study the relationship between the measured flow value and the real flow value. Suppose we have a small

detector element (for example, a slat of the CTB) with azimuthal angle coverage from φ_{low} to φ_{high}, then nominally the signal in the detector is

$$\begin{aligned} N &\sim \int_{\varphi_{\text{low}}}^{\varphi_{\text{high}}} \{1 + \sum_{n=1}^{\infty} 2v_n \cos[n(\varphi - \psi_r)]\} \cdot d\varphi \\ &= \varphi_{\text{high}} - \varphi_{\text{low}} + \sum_{n=1}^{\infty} \frac{2v_n}{n} \{\sin[n(\varphi_{\text{high}} - \psi_r)] - \sin[n(\varphi_{\text{low}} - \psi_r)]\} \\ &= \varphi_{\text{high}} - \varphi_{\text{low}} + \sum_{n=1}^{\infty} \frac{2v_n}{n} \cdot 2 \sin \frac{n(\varphi_{\text{high}} - \varphi_{\text{low}})}{2} \cdot \cos[n(\frac{\varphi_{\text{high}} + \varphi_{\text{low}}}{2} - \psi_r)] \end{aligned} \quad (6.31)$$

On the other hand, experimentally we measure $\widetilde{v}_n$ with $\frac{\varphi_{\text{high}} + \varphi_{\text{low}}}{2}$ representing the azimuthal angle of the whole detector, and the signal in the detector is

$$\begin{aligned} N &\sim \{1 + \sum_{n=1}^{\infty} 2\widetilde{v}_n \cos[n(\frac{\varphi_{\text{high}} + \varphi_{\text{low}}}{2} - \psi_r)]\} \cdot (\varphi_{\text{high}} - \varphi_{\text{low}}) \\ &= \varphi_{\text{high}} - \varphi_{\text{low}} + \sum_{n=1}^{\infty} 2\widetilde{v}_n \cdot (\varphi_{\text{high}} - \varphi_{\text{low}}) \cdot \cos[n(\frac{\varphi_{\text{high}} + \varphi_{\text{low}}}{2} - \psi_r)] \end{aligned} \quad (6.32)$$

Comparing Eq. 6.31 and 6.32, we have

$$\frac{2v_n}{n} \cdot 2 \cdot \sin \frac{n(\varphi_{\text{high}} - \varphi_{\text{low}})}{2} = 2\widetilde{v}_n \cdot (\varphi_{\text{high}} - \varphi_{\text{low}})$$

or

$$v_n = \frac{\frac{n}{2}\Delta\varphi}{\sin(\frac{n}{2}\Delta\varphi)} \cdot \widetilde{v}_n \quad (6.33)$$

where $\Delta\varphi = \varphi_{\text{high}} - \varphi_{\text{low}}$ can be used to denote the granularity of a hit-based detector. The correction term $\frac{n}{2}\Delta\varphi / \sin(\frac{n}{2}\Delta\varphi)$ is always bigger than 1, so the effect of the granularity correction is to increase the flow value. The granularity effect is more prominent for larger n (higher harmonics). When we have a perfect hit-based detector where $\Delta\varphi$ goes to 0, the limit of the correction term becomes 1 and no granularity correction is needed, just like in the case of track-based detectors.

6.2.5 Before and after corrections

Since the 4 terms measure the same physical quantity, they should give very close results, if not exactly the same. Compared in Fig. 6.4 are the directed flow results of 4 terms in a small sample of

data from the TPC and FTPCs before and after corrections. It is clear that after corrections, the 4 terms have much closer results than before corrections.

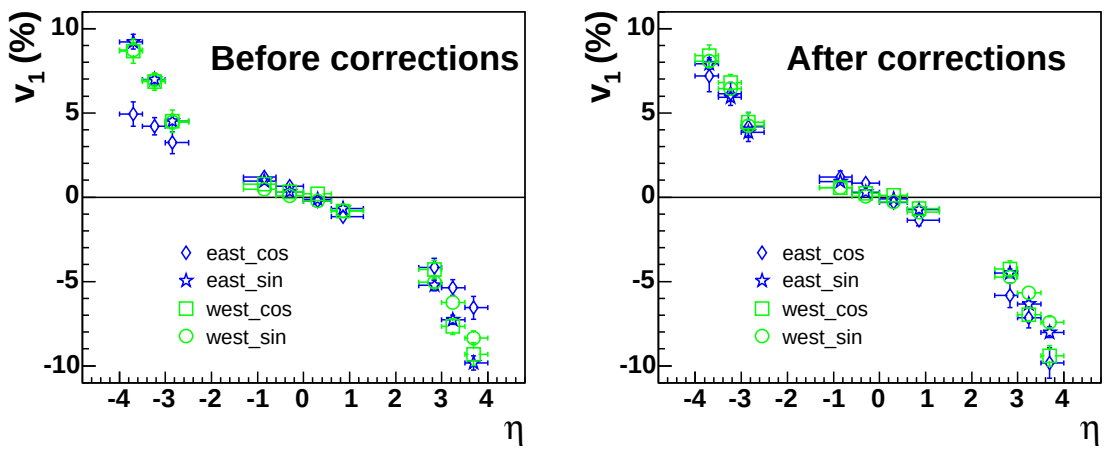

Figure 6.4: The directed flow results of 4 terms versus η in a small sample data from the TPC and FTPCs before (left panel) and after (right panel) corrections.

6.2.6 Robust test of flow analysis with the ZDC-SMD

Shown in Fig. 6.5 is the comparison between the directed flow results of the 4-term average and the full event plane approach on a small sample of data from the TPC and FTPCs. Within the statistical errors, the two results are consistent with each other.

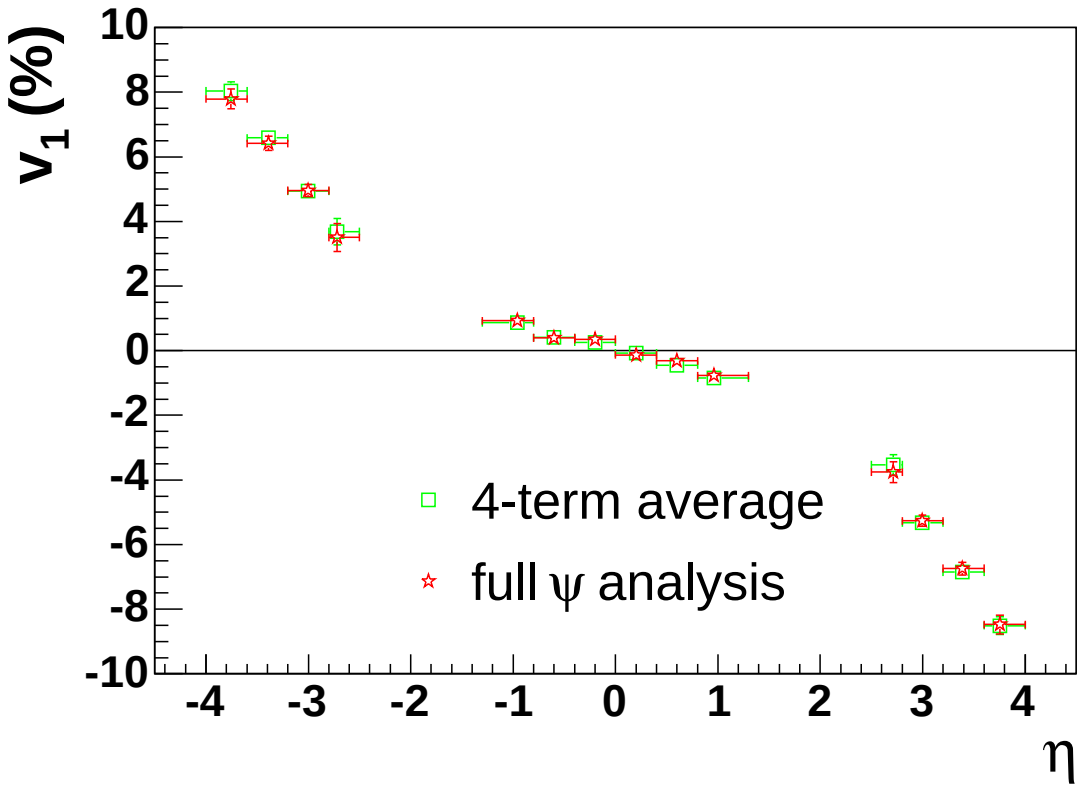

Figure 6.5: $v_1(\eta)$ comparison between the 4-term average and the full ψ analysis on a small sample of data from the TPC and FTPCs.

Chapter 7

Flow Results I: Directed Flow

In this chapter, I present the directed flow results in Au +Au collisions at $\sqrt{s_{NN}} = 62$ GeV and 200 GeV, and in Cu +Cu collisions at $\sqrt{s_{NN}} = 200$ GeV, especially using the 1st-order event plane reconstructed from spectator neutrons detected by the ZDC-SMDs at the STAR detector.

7.1 Introduction of transport models

7.1.1 RQMD

RQMD [79] (relativistic quantum molecular dynamics) is a semiclassical microscopic transport model, that combines classical propagation with stochastic interactions. In RQMD, strings and resonances are excited in elementary collisions of nucleons, and overlapping strings may fuse into "color ropes". Subsequently, the fragmentation products from rope, string, and resonance decays interact with each other and the original nucleons, mostly via binary collisions. [80] These interactions drive the system towards equilibration [81] and are responsible for the collective flow development, even in the preequilibrium stage.

The RQMD code contains an option to vary the pressure in the high-density state. In the medium, baryons may acquire effective masses, generated by introducing Lorentz-invariant quasipotentials into the mass-shell constraints which simulate the effect of "mean fields" [82]. There are no potential-type interactions in the so-called cascade mode of RQMD, where the equilibrium pressure is simply that of an ideal gas of hadrons and resonances. Its equation of state is very similar to the one calculated in Ref. [83], because the spectrum of included resonance states is nearly the same.

7.1.2 UrQMD

UrQMD [84] (Ultra-relativistic quantum molecular dynamics) is another relativistic hadronic transport model describing the phenomenology of nuclear collisions, and grew out of an effort to improve RQMD and adapt it for higher beam energies. The collision term is roughly the same as that of RQMD, though some implementation details are different. For example, UrQMD handles more types of particles, and employs more detailed cross sections parametrized according to the experimental data. In the early versions of UrQMD such as used in this dissertation, hard processes are not included.

7.1.3 AMPT

The AMPT model (a multiphase transport model) [85] is a hybrid model that uses minijet partons from hard processes and strings from soft processes in the heavy ion jet interaction generator (HIJING) model [86] as the initial conditions. Time evolution of resulting minijet partons is then described by Zhang's parton cascade (ZPC) [87] model. After minijet partons stop interacting, they are combined with their parent strings, as in the HIJING model with jet quenching, to fragment into hadrons using the Lund string fragmentation model as implemented in the PYTHIA program [88]. The final-state hadronic scatterings are then modelled by a relativistic transport (ART) model [89].

The AMPT model has a "string melting" option to convert the initial excited strings into partons. Interactions among these partons are again described by the ZPC parton cascade model. Since there are no inelastic scatterings, only quarks and antiquarks from the melted strings are present in the partonic matter. The transition from the partonic matter to the hadronic matter is achieved using a simple coalescence model, where adjacent quark-antiquark pairs are combined into mesons and likewise, adjacent quark/antiquark triplets with appropriate invariant masses are combined into baryons/antibaryons.

7.2 Model calculations and previous measurements

Directed flow in heavy-ion collisions is quantified by the first harmonic (v_1) in the Fourier expansion of the azimuthal distribution of produced particles with respect to the reaction plane [28]. It describes collective sideward motion of produced particles and nuclear fragments and carries information on the very early stages of the collision [80]. The shape of $v_1(y)$ in the central rapidity region is of special interest because it might reveal a signature of a possible Quark-Gluon Plasma (QGP) phase [40, 90, 91].

At AGS and SPS energies, v_1 versus rapidity is an almost linear function of rapidity [26, 27, 78, 92]. Often, just the slope of $v_1(y)$ at midrapidity is used to define the strength of directed flow. The sign of v_1 is by convention defined as positive for nucleons in the projectile fragmentation region. At AGS and SPS energies, the slope of $v_1(y)$ at midrapidity is observed to be positive for protons, and significantly smaller in magnitude and negative for pions [78, 92, 93] . The opposite directed flow of pions is usually explained in terms of shadowing by nucleons. At RHIC energies, directed flow is predicted to be smaller near midrapidity with a weaker dependence on pseudorapidity [42, 94]. It may exhibit a characteristic wiggle as discussed in section 2.2.1 [40, 42, 90, 94], whereby directed flow changes sign three times outside the beam fragmentation regions, in contrast to the observed sideward deflection pattern at lower energies where the sign of $v_1(y)$ changes only once, at midrapidity. The observation of the slope of v_1 at midrapidity being negative for nucleons or positive for pions would constitute such a wiggle.

In one-fluid dynamical calculations [40, 90], the wiggle structure appears only under the assumption of a QGP equation of state, thus becoming a signature of the QGP phase transition. Then the wiggle structure is interpreted to be a consequence of the expansion of the highly compressed, disk-shaped system, with the plane of the disk initially tilted with respect to the beam direction. [90] The subsequent system expansion leads to the so-called anti-flow [90] or third flow component [40]. Such flow can reverse the normal pattern of sideward deflection as seen at lower energies, and hence

can result in either a flatness of v_1, or a wiggle structure if the expansion is strong enough.

A similar wiggle structure in nucleon $v_1(y)$ is predicted if one assumes strong but incomplete baryon stopping together with strong space-momentum correlations caused by transverse radial expansion [42]. While the predictions for baryon directed flow are unambiguous in both hydrodynamical and transport models, the situation for pion directed flow is less clear. RQMD model calculations [42] for Au +Au collisions at $\sqrt{s_{NN}}$ = 200 GeV indicate that shadowing by protons causes the pions to flow mostly with opposite sign to the protons, but somewhat diffused due to higher thermal velocities for pions. Similar UrQMD calculations [94] predict no wiggle for pions in the central rapidity region with a negative slope at midrapidity as observed at lower collision energies.

At RHIC, most of the detectors cover the central rapidity region where the directed flow signal is small and the analysis procedures easily can be confused by azimuthal correlations not related to the reaction plane orientation, the so-called non-flow effects. Only recently have the first v_1 results been reported by the STAR Collaboration [68] and preliminary results by the PHOBOS Collaboration [95]. In Ref. [68], the shape of v_1 in the region on either side of midrapidity is poorly resolved due to large statistical errors. This shortcoming arose from having only about 70,000 events from the FTPCs during their commissioning in the RHIC run II period (2002).

In early 2004, STAR installed Shower Maximum Detectors (SMDs) sandwiched between the first and second modules of each existing STAR ZDC at $|\eta| > 6.3$. The $v_1\{\text{ZDC-SMD}\}$ should have minimal contribution from non-flow effects due to the large rapidity gap between the spectator neutrons used to establish the reaction plane and the rapidity region where the measurements were performed.

7.3 62 GeV Au +Au

In this section, I present directed flow measurements in Au +Au collisions at $\sqrt{s_{NN}}$ = 62 GeV. Results are obtained by three different methods, namely, the three-particle cumulant method

($v_1\{3\}$), the event plane method with mixed harmonics ($v_1\{$EP1,EP2$\}$), and the standard method [28] with the first-order event plane reconstructed from neutral fragments of the incident beams ($v_1\{$ZDC-SMD$\}$). The first and the second method are described in Ref. [55] and Refs. [28, 57], respectively. Both offer enhanced suppression of non-flow effects, including correlations due to momentum conservation, compared with the standard method (in which the event plane is reconstructed from the same harmonics and in the same rapidity region where the event anisotropy is measured). In the present study, the procedures to obtain $v_1\{3\}$ and $v_1\{$EP1,EP2$\}$ are essentially the same as in Ref. [68]. The third method is the ZDC-SMD-based approach that is the main focus of this dissertation. This is the first report from RHIC of flow results with the event plane reconstructed from spectator fragments. Five million minimum-bias events were used in this study for each of the three analyses, and all the errors presented are statistical. Cuts used in the TPC analysis are listed in Table 7.1, except for the upper p_t cutoff which often goes higher as shown in the graphs. The 2 GeV$/c$ in Table 7.1 means the upper limit of the integral for p_t-integrated v_1. For the FTPC ($2.5 < |\eta| < 4.0$), only 5 hits are required. These cuts will be the same for 200 GeV Au +Au collisions and Cu +Cu collisions, unless otherwise specified. The centrality definition is based on the raw charged particle TPC multiplicity with $|\eta| < 0.5$ (reference multiplicity). Listed in Table 7.2 are the reference multiplicity and the estimated impact parameter [97] for each centrality bin for 62 GeV Au +Au collisions.

The centrality ranges of Au +Au collisions at $\sqrt{s_{NN}}$ = 62 GeV where the three v_1 methods are usable are slightly different: $v_1\{3\}$ fails at centralities less than 5% and centralities greater than 70%, because the four particle cumulant $v_2\{4\}$, which is a necessary ingredient for measuring $v_1\{3\}$, is not measurable in those regions possibly due to large v_2 fluctuations; $v_1\{$ZDC-SMD$\}$ fails for centrality less than 10% because of insufficient event plane resolution in central collisions. Fig. 7.1 shows charged-particle v_1 as a function of pseudorapidity, η, for centrality $10\%-70\%$ where all three methods work, from Au +Au collisions at $\sqrt{s_{NN}}$ = 62 GeV. The arrows in the upper panel

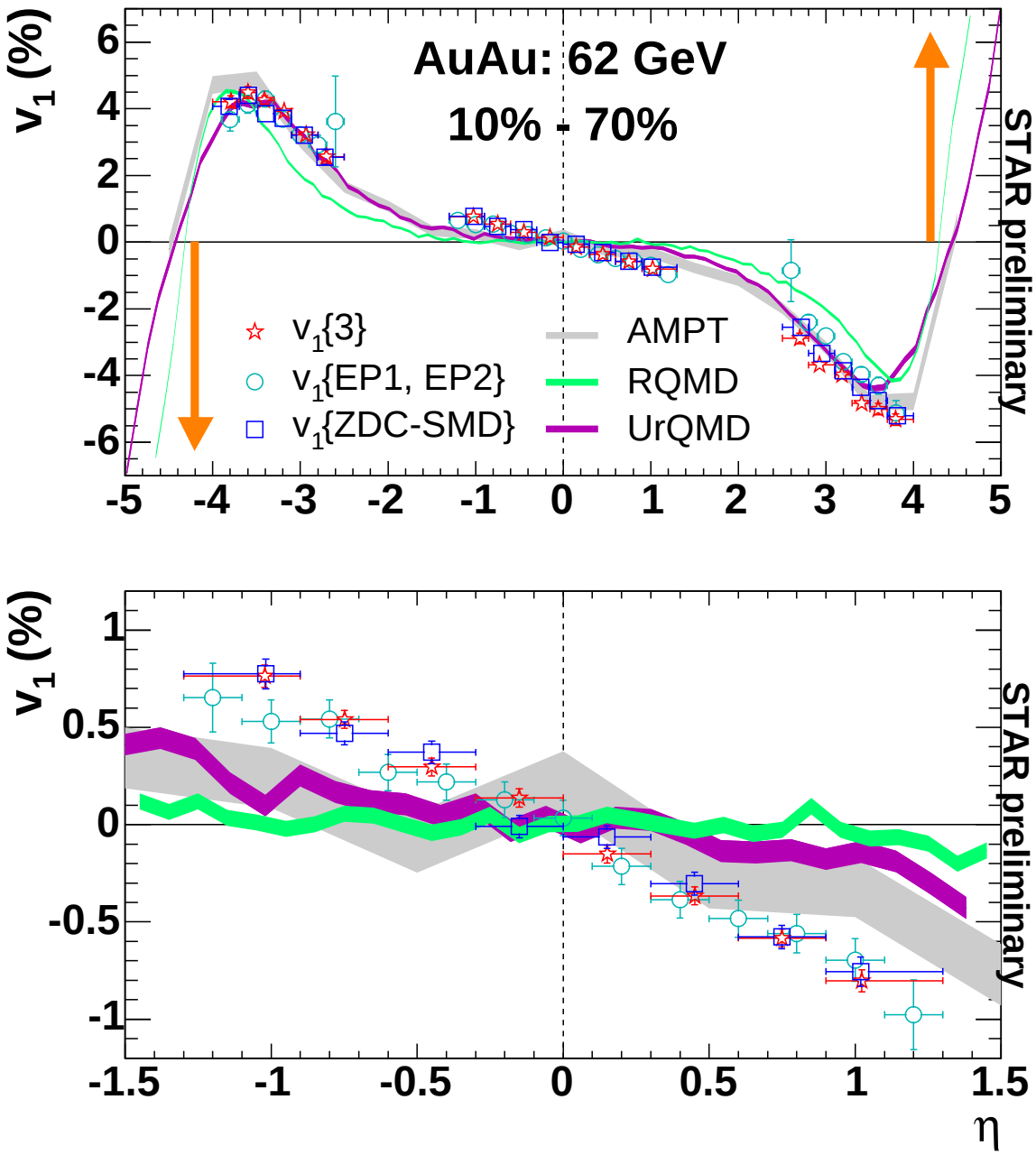

Figure 7.1: Directed flow for charged particles as a function of pseudorapidity, for centrality 10%–70%. The arrows in the upper panel indicate the direction of flow for spectator neutrons. The arrow positions on the pseudorapidity axis corresponds to where the incident ions would lie on a rapidity scale. The lower panel shows the mid-pseudorapidity region in more detail.

cut	value
p_t	0.15 to 2.0 GeV$/c$
η	–1.3 to 1.3
multiplicity	> 10
vertex z	–30. to 30. cm
vertex x, y	–1.0 to 1.0 cm
fit points	> 15
fit pts / max. pts	> 0.52
dca	< 2.0 cm
trigger	min. bias

Table 7.1: Cuts used in the TPC analysis of 62 GeV Au +Au collisions. Vertex refers to the event vertex, fit points are the space points on a track, and dca is the distance of closest approach of the track to the event vertex.

indicate the direction of flow for spectator neutrons as determined from the ZDC-SMDs. The lower panel shows, on expanded scales, the mid-pseudorapidity region measured in the STAR TPC. The results from the three different methods agree with each other very well. In Ref. [68], the relative systematic uncertainty in $v_1\{3\}$ and $v_1\{$EP1,EP2$\}$ was estimated to be about 20%. That error estimate was obtained under the assumption that the directed flow measurements using two-particle correlations were totally dominated by non-flow effects. Such an assumption provides an upper limit on the systematic errors. Ref. [57] provides further discussion on the systematic uncertainties. The comparison of $v_1\{$ZDC-SMD$\}$ and $v_1\{3\}$ indeed shows that the relative difference is no more than 20% around mid-pseudorapidity (where the directed flow itself is less than 0.005) and the difference is only about 5% in the forward pseudorapidity region. $v_1\{$ZDC-SMD$\}$ was also calculated using the information from the east and west ZDCs separately as well as separately from correlations in the vertical and horizontal directions (note that the ZDC-SMDs have a rectangular shape); all the results agree within 15% (see Fig. 6.5). In another systematic study of $v_1\{$ZDC-SMD$\}$, a tighter distance of closest approach (dca) cut was applied to reduce the number of weak decay tracks or secondary interactions. The ratio of v_1 obtained with dca < 1 cm to the v_1 result with the default cut (dca < 2 cm) was measured to be $v_1^{\text{dca} < 1\text{ cm}}/v_1^{\text{dca} < 2\text{ cm}} = 1.00 \pm 0.07$ for charged particles (see

Centrality	RefMult	Impact parameter (fm)
$80\% - 100\%$	< 9	$14.25 + 0.66 - 0.84$
$70\% - 80\%$	$9 - 20$	$12.77 + 0.73 - 0.57$
$60\% - 70\%$	$20 - 38$	$11.89 + 0.67 - 0.52$
$50\% - 60\%$	$38 - 65$	$10.95 + 0.58 - 0.52$
$40\% - 50\%$	$65 - 102$	$9.91 + 0.47 - 0.42$
$30\% - 40\%$	$102 - 154$	$8.71 + 0.52 - 0.31$
$20\% - 30\%$	$154 - 222$	$7.36 + 0.47 - 0.26$
$10\% - 20\%$	$222 - 313$	$5.72 + 0.32 - 0.21$
$5\% - 10\%$	$313 - 373$	$4.08 + 0.16 - 0.21$
$0 - 5\%$	> 373	$2.24 + 0.07 - 0.14$

Table 7.2: The reference multiplicity and the estimated impact parameter in each centrality bin for 62 GeV Au +Au collisions.

Fig. 7.2).

AMPT [85], RQMD [80], and UrQMD [84] model calculations for the same centrality of Au +Au collisions at $\sqrt{s_{NN}}$ = 62 GeV are also shown in Fig. 7.1. Most transport models, including AMPT, RQMD and UrQMD, underpredict elliptic flow (v_2) at RHIC energies, and we now report that they also underpredict the charged-particle $v_1(\eta)$ within a unit or so of mid-pseudorapidity, but then come into good agreement with the data over the region $2.5 < |\eta| < 4.0$. While the magnitude of v_1 for charged particles increases with the magnitude of pseudorapidity below $|\eta| \sim 3.8$ for centralities between 10% and 70%, our results are compatible with the peak in $|v_1|$ lying in the $|\eta|$ region predicted by all three models, namely, 3.5 to 4.0.

No apparent wiggle structure, as discussed above, is observed within our acceptance. Throughout our pseudorapidity acceptance, charged particles on a given side of $\eta = 0$ flow in the opposite direction to the fragmentation neutrons on that side. This is consistent with the direction expected in the ”anti-flow” scenario [90] but it is also the same direction as measured for pions at lower energies that is usually related to the pion shadowing by nucleons. Assuming that the charged-particle flow at beam rapidity is dominated by protons, one would conclude that over the entire pseudorapidity range $v_1(\eta)$ changes sign three times. However, this does not prove the existence of the wiggle

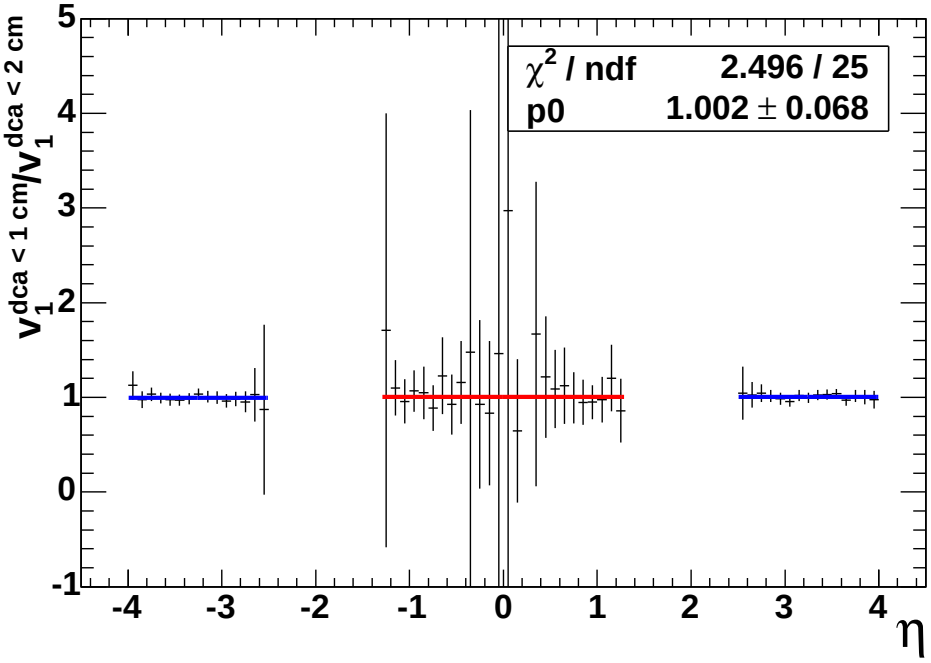

Figure 7.2: $v_1^{\text{dca} < 1\text{ cm}}/v_1^{\text{dca} < 2\text{ cm}}$ as a function of η on a small sample of data from the TPC and FTPCs, fitted by a constant.

structure for protons and pions separately. Measurements of directed flow of identified particles could be more informative in this respect.

In STAR, particle identification is feasible only in the main TPC, which covers the pseudorapidity region $|\eta| < 1.3$. In this region, the RQMD model predicts very flat $v_1(\eta)$ for pions and a clear wiggle structure, with negative slope $dv_1/d\eta$ at mid-pseudorapidity for protons at $\sqrt{s_{NN}}$ = 62 GeV. (The relatively strong wiggle for pions reported in Ref. [42] is developed only at higher collision energies.) To maximize the magnitude of the possible slope, we select the centrality interval 40% to 70%, where flow anisotropies normally are at their peak. The result is shown in Fig. 7.3. With the current statistics, we observe that pion flow is very similar to that for charged particles, with the slope at midrapidity dv_1/dy about 0.0074 ± 0.0010, obtained from a linear fit over the region $|y| < 1.3$ (dashed line). For protons, the slope dv_1/dy is 0.025 ± 0.011 from a linear fit in $|y| < 0.6$ (solid line). If this 2.3σ effect is confirmed with better statistics, it will be the first observation of

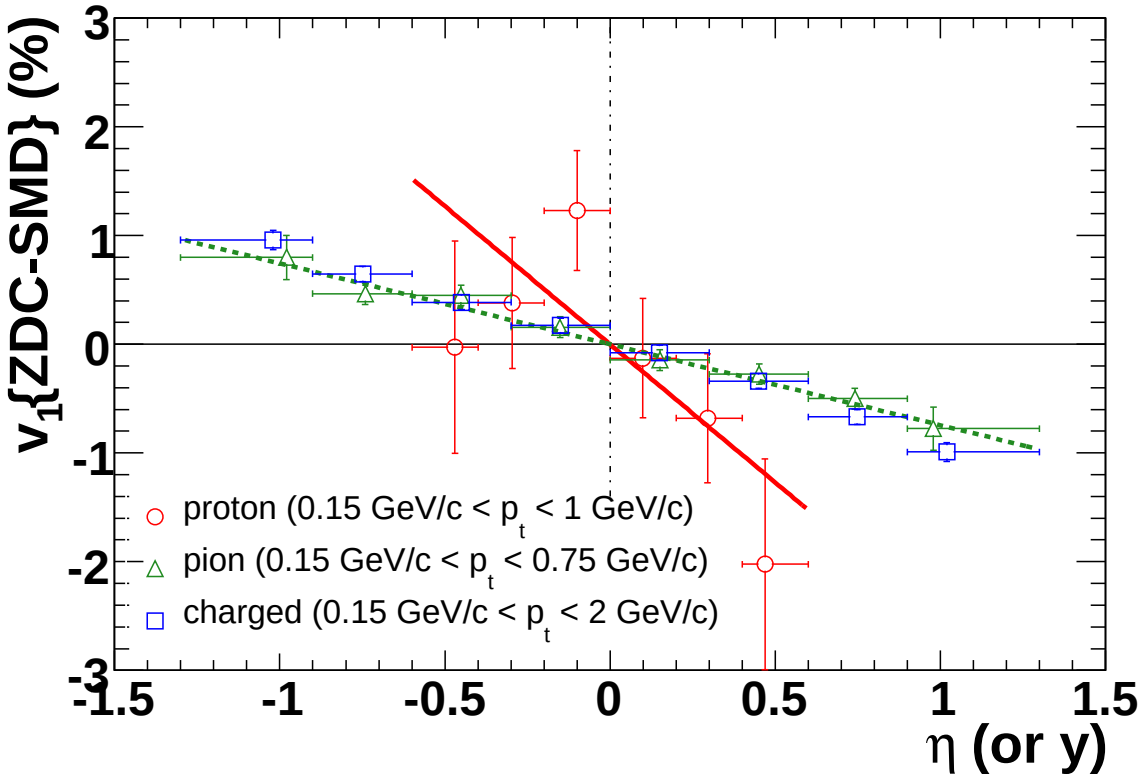

Figure 7.3: v_1 versus rapidity for protons and pions in 62 GeV AuAu. The charged-particle $v_1(\eta)$ is plotted as a reference. The different upper end of the p_t range for protons and pions is due to different limits of the dE/dx identification method. The solid and dashed lines are results from linear fits described in the text. All results are from analyses using the reaction plane reconstructed by the ZDC-SMD, $v_1\{\text{ZDC-SMD}\}$.

the wiggle effect, that has been searched for since the 1990s.

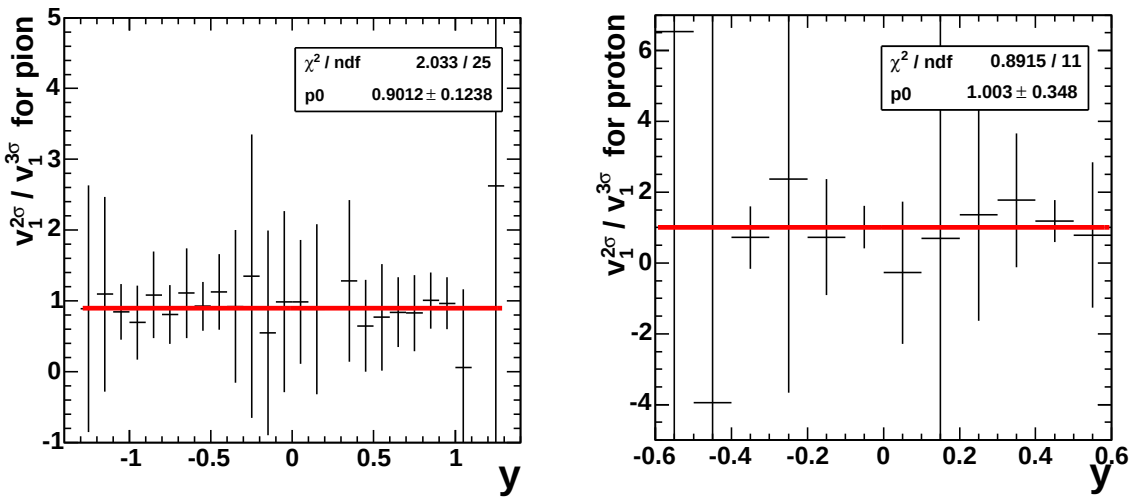

Figure 7.4: $v_1^{2\sigma}/v_1^{3\sigma}$ as a function of rapidity on a small sample of data from the TPC for pions and protons, fitted by a constant.

At present, STAR's statistics for baryons are rather small compared with the statistics for all charged particles, and our best estimates of the fitted slope are such that a negative baryon slope with comparable magnitude to the RQMD prediction is not decisively ruled out. For the identified particles, the influence of the particle identification procedures on the flow values for pions and protons may be a source of errors. By default we eliminate particles 3σ away from the expected TPC energy loss for the relevant particle type. When we tightened the cut to 2σ instead of 3σ, we found that for $40\% - 70\%$ most central events, the $v_1\{\text{ZDC-SMD}\}$ for pions is reduced by less than 10% while the proton $v_1\{\text{ZDC-SMD}\}$ stays constant within errors (See Fig. 7.4).

Fig. 7.5 shows v_1 for charged particles as a function of η for different centralities. We do not observe an onset of any special feature in the pseudorapidity dependence of v_1 at any centrality. Preliminary $v_1(\eta)$ results from PHOBOS [96] for centrality 10% to 50% are consistent with our data at the same centrality (see Fig. 7.6) except that $|v_1(\eta)|$ from PHOBOS has its peak at $|\eta|$ of about 3 to 3.5, while STAR's $|v_1(\eta)|$ peaks at $|\eta|$ about 3.8 or higher. PHOBOS has acceptance

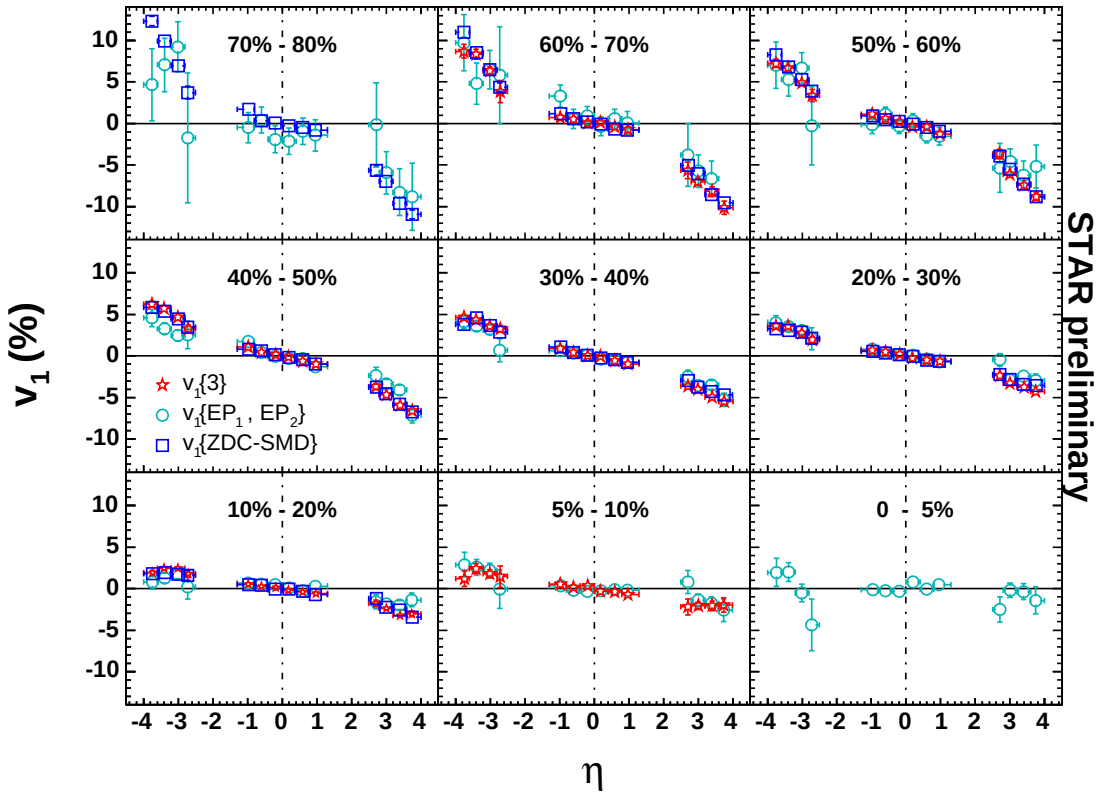

Figure 7.5: Directed flow for charged particles as a function of pseudorapidity for different centralities.

down to lower p_t than STAR, which is the only known difference between the two experiments that might explain the discrepancy. There might be a significant change in particle abundances below STAR's p_t acceptance cut (0.15 GeV$/c$), which could account for some or all of this difference in the $|v_1|$ peak position. If we move our p_t threshold higher than 0.15 GeV$/c$, the discrepancy does not appear to grow. Normally, the best way to investigate the discrepancy would be for PHOBOS to raise their p_t threshold to match STAR's acceptance, but it is not possible for them to do that. Therefore, we have not been able to come to any definite conclusion about the differences at forward η.

The transverse-momentum dependence of v_1 is shown in Fig. 7.7. Since $v_1(\eta, p_t)$ is asymmetric

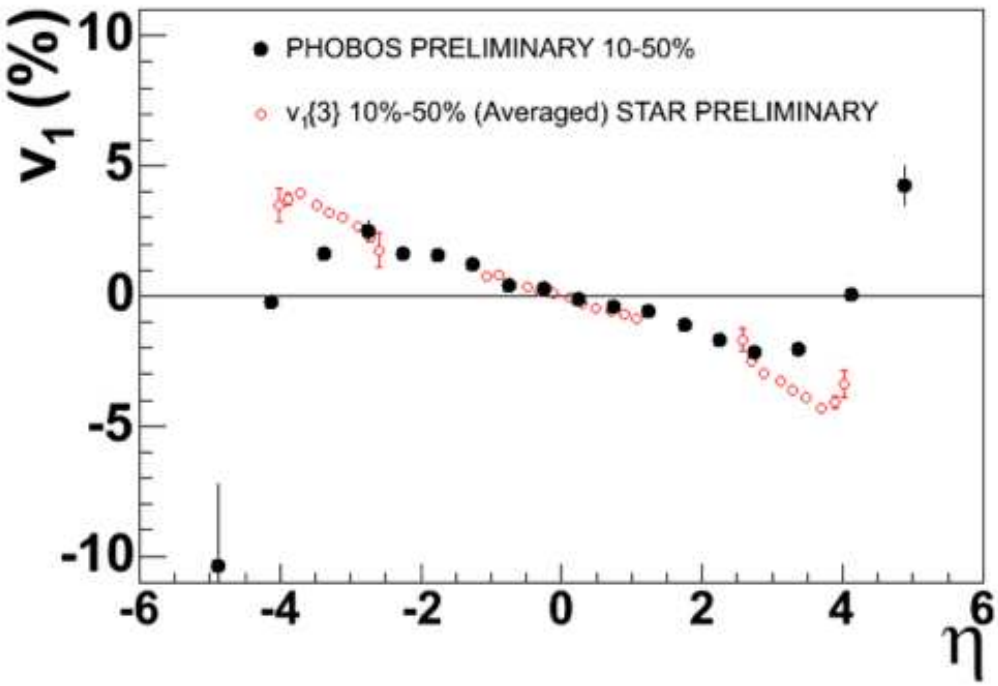

Figure 7.6: $v_1(\eta)$ comparison between STAR and PHOBOS in Au +Au collisions at 62 GeV.

about $\eta = 0$, the integral of $v_1(\eta, p_t)$ over a symmetric η range goes to zero. We change $v_1(\eta, p_t)$ of particles with negative η into $-v_1(-\eta, p_t)$, and integrate over all η. If $v_1(p_t)$ is negative at a specific p_t, that means particles with that p_t have a negative slope in $v_1(\eta)$ like the pion v_1 in the mid-pseudorapidity region, while if $v_1(p_t)$ is positive at a specific p_t, that means particles with that p_t have a positive slope in $v_1(\eta)$, like spectators. Due to the small magnitude of the v_1 signal close to mid-pseudorapidity ($|\eta| < 1.3$), only the averaged $v_1(p_t)$ over centralities $10\% - 70\%$ is shown. For $2.5 < |\eta| < 4.0$, the v_1 signal is large enough to be resolved for different centrality regions. The poor p_t resolution for higher p_t in the FTPCs limits the p_t range to below 1 GeV$/c$ for $2.5 < |\eta| < 4.0$. For all centralities, the magnitude of v_1 is observed to reach its maximum at $p_t \approx 1$ GeV$/c$ for $|\eta| < 1.3$ and at $p_t \approx 0.5$ GeV$/c$ for $2.5 < |\eta| < 4.0$. Note that from its definition, $v_1(p_t)$ must approach zero as p_t approaches zero.

The centrality dependence of p_t-integrated v_1 is shown in Fig. 7.8. In principle, integrated v_1

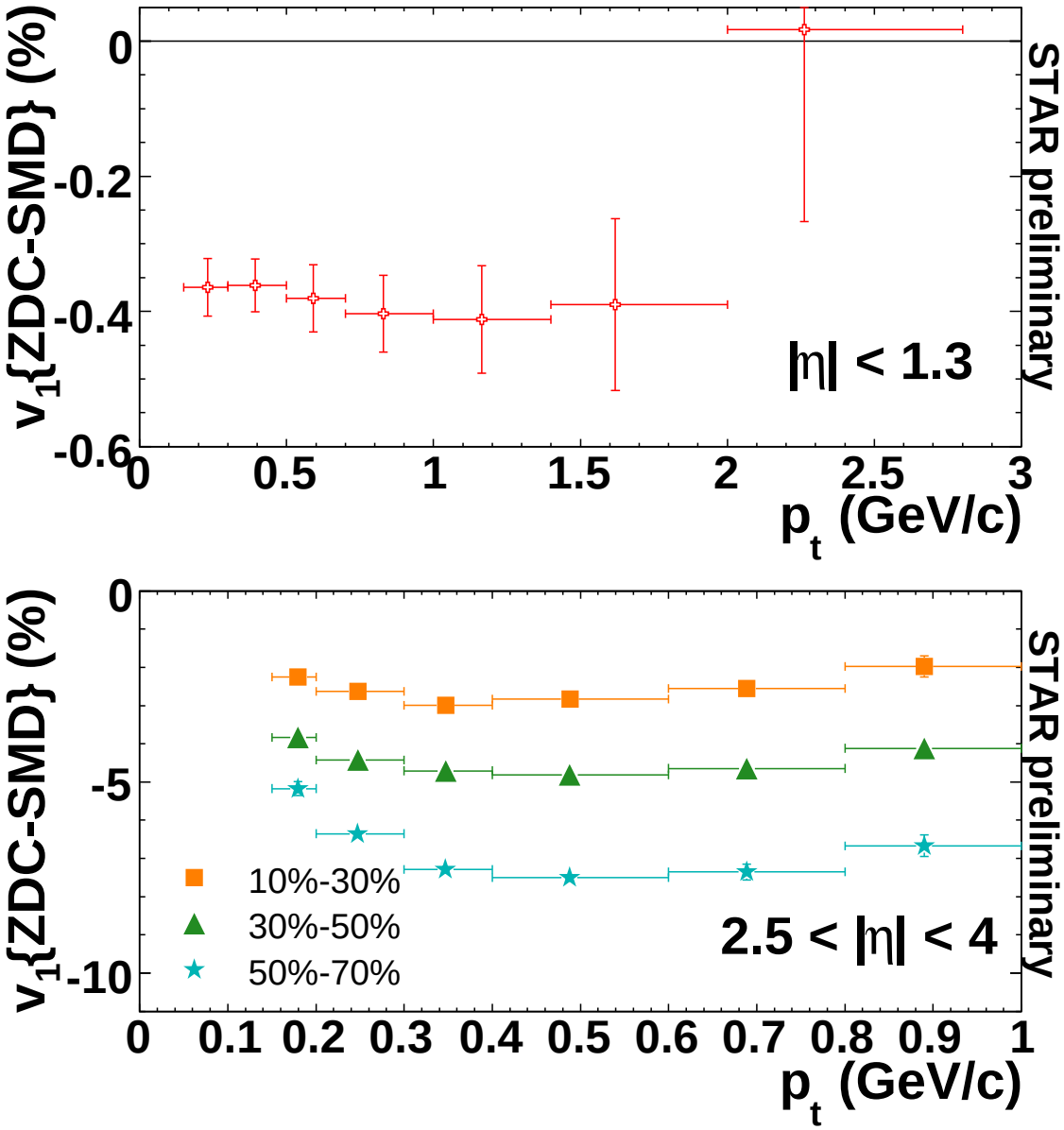

Figure 7.7: The upper panel shows $v_1\{\text{ZDC-SMD}\}$ versus p_t measured in the main TPC ($|\eta| < 1.3$), for centrality 10%–70% in 62 GeV AuAu. The lower panel shows $v_1\{\text{ZDC-SMD}\}$ versus p_t measured in the Forward TPCs ($2.5 < |\eta| < 4.0$), for different centralities in 62 GeV AuAu. The differential directed flow of particles with negative η has been changed in sign as stated in the text. Note the different scales on both axes for the two panels.

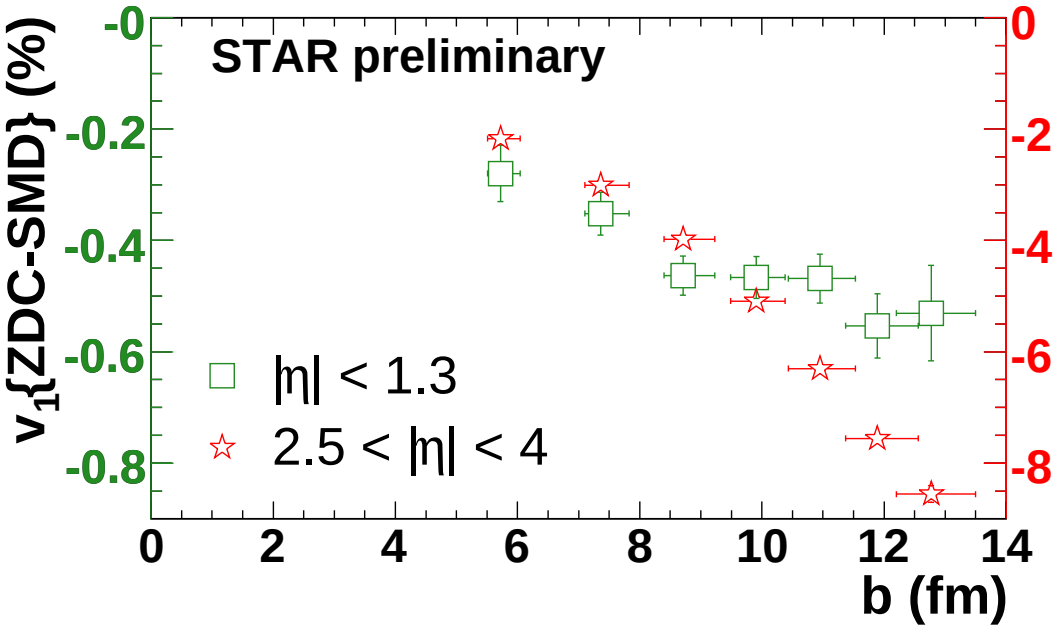

Figure 7.8: Directed flow for charged particles as a function of impact parameter in 62 GeV AuAu for the mid-pseudorapidity region ($|\eta| < 1.3$, with the left vertical scale) and the forward pseudorapidity region ($2.5 < |\eta| < 4.0$, with the right vertical scale.) The differential directed flow of particles with negative η has been changed in sign as stated in the text.

could also be both positive and negative for the same reason as $v_1(p_t)$. The values of the impact parameter were obtained using a Monte Carlo Glauber calculation [97], listed in Table 7.2. As expected, the magnitude of v_1 decreases as collisions become more central. It is seen that v_1 in the more forward pseudorapidity region $2.5 < |\eta| < 4.0$ varies more strongly with centrality than in the region closer to mid-pseudorapidity $(|\eta| < 1.3)$.

7.4 200 GeV Au +Au

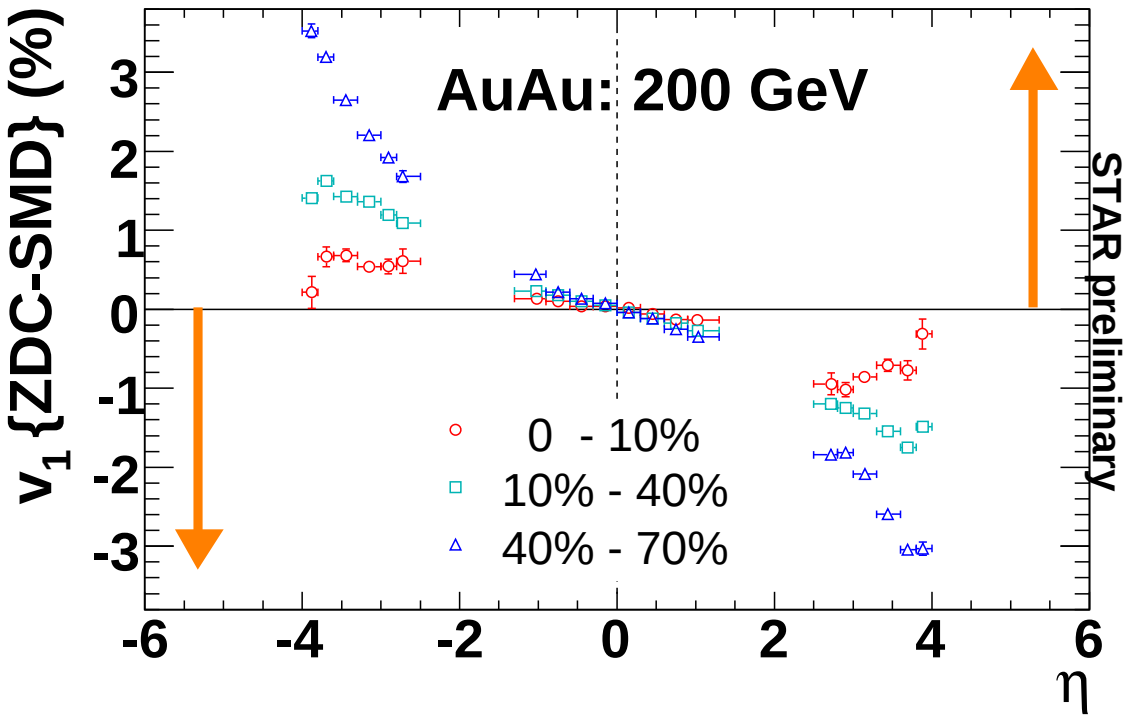

Figure 7.9: Directed flow for charged particles as a function of pseudorapidity for 3 centrality bins in 200 GeV AuAu.

Fig. 7.9 presents charged-particle $v_1(\eta)$ in three centrality bins in Au +Au collisions at $\sqrt{s_{NN}}$ = 200 GeV. The arrows have the same meaning as in Fig. 7.1. Six million minimum-bias events were used in the $v_1\{\text{ZDC-SMD}\}$ analysis. The magnitude of $v_1(\eta)$ is smaller compared with the case in 62 GeV AuAu in Fig. 7.5. The centrality dependence is qualitatively similar to the trend seen at SPS by NA49 in Fig. 7.10 [92], but STAR's rapidity coverage is a larger fraction of the available

range. For peripheral collisions, the directed flow is a monotonic function of η; for mid-periperal collisions, the curve is mostly monotonic with the only outermost points turning back; for central collisions, STAR's coverage is such that we can probe the interesting region $|\eta| \sim 3.5$ to 4 where v_1 approaches zero for centrality 0 to 10%, similiar to the case of $\theta = 6$ in Fig. 2.4. The observed pattern of $v_1(\eta)$ at different centralities may provide insights into the stronger stopping in more central collisions.

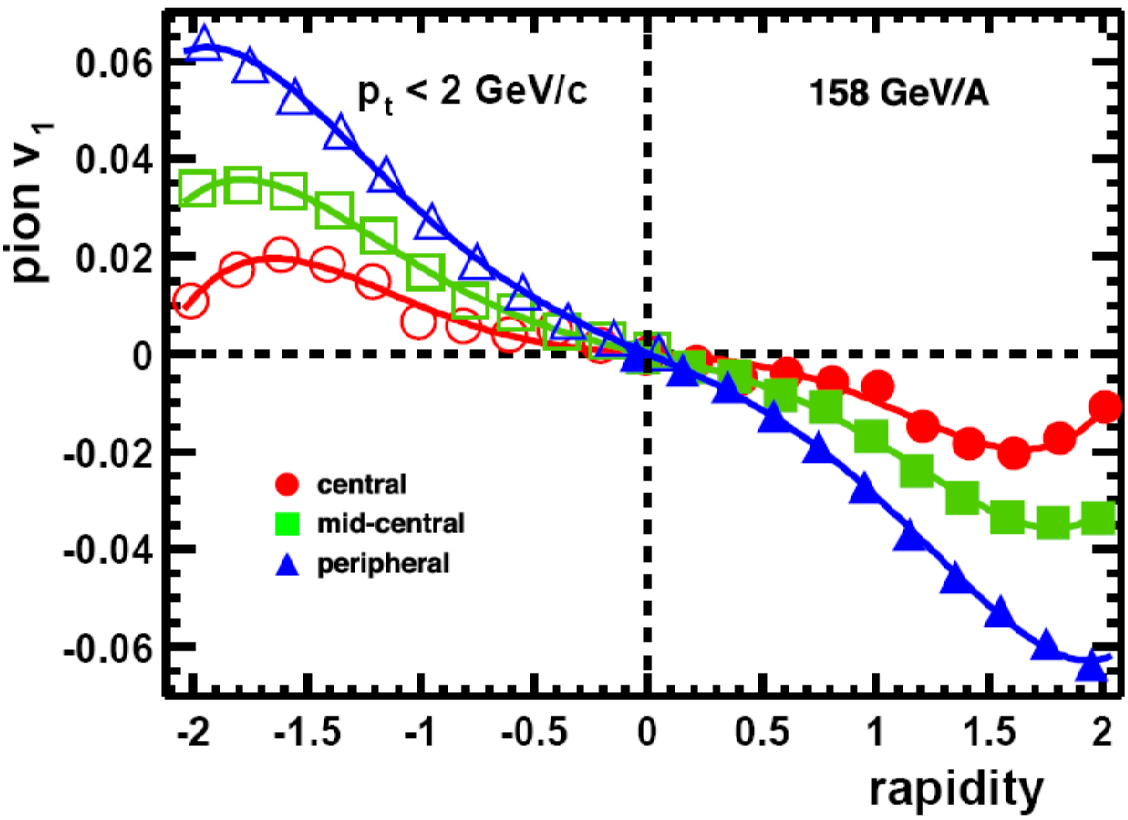

Figure 7.10: Standard directed flow as a function of rapidity for pions from 158A GeV Pb +Pb. [92]

The result of pion $v_1(y)$ for centrality $40\% - 70\%$ is shown in Fig. 7.11. With the current statistics, we observe that pion flow is very similar to that for charged particles, with the slope at midrapidity dv_1/dy about 0.0035 ± 0.0005, obtained from a linear fit over the region $|y| < 1.3$ (dashed line). Due to the low statistics for identified protons, the proton $v_1(y)$ has big statistical

errors and is consistent with zero.

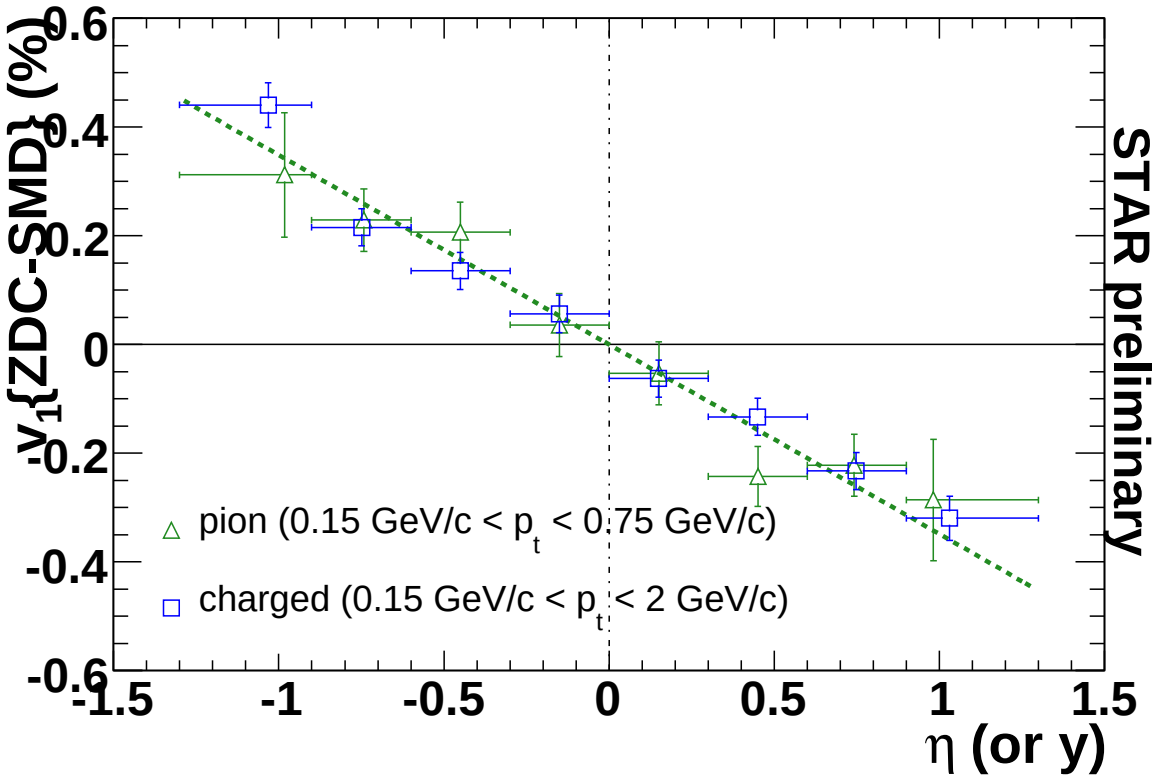

Figure 7.11: v_1 versus rapidity for pions in 200 GeV AuAu. The charged-particle $v_1(\eta)$ is plotted as a reference. The dashed line is the result from a linear fit described in the text. All results are from analyses using the reaction plane reconstructed by the ZDC-SMD, $v_1\{\text{ZDC-SMD}\}$.

The transverse-momentum dependence of v_1 is shown in Fig. 7.12 for 3 centrality bins. The poor p_t resolution for higher p_t in the FTPCs limits the p_t range to below 2 GeV/c for $2.5 < |\eta| < 4.0$. For $2.5 < |\eta| < 4.0$, $v_1(p_t)$ is always negative (up to $p_t = 2$ GeV/c), and the magnitude of $v_1(p_t)$ is observed to reach its maximum at $p_t \approx 1.1$ GeV/c for all centralities. For $|\eta| < 1.3$, $v_1(p_t)$ is always negative (up to $p_t = 4$ GeV/c) in the peripheral collisions (40% - 80%), but crosses zero at $p_t \approx 2$ GeV/c in the mid-central collisions (10% - 40%) and at $p_t \approx 1.5$ GeV/c in the central collisions (0 - 10%).

To study the zero-crossing behavior of $v_1(p_t)$ in the TPC range in 200 GeV AuAu, we investigate central collisions (0 - 10%) in more detail. Fig. 7.13 shows charged-particle $v_1\{\text{ZDC-SMD}\}$

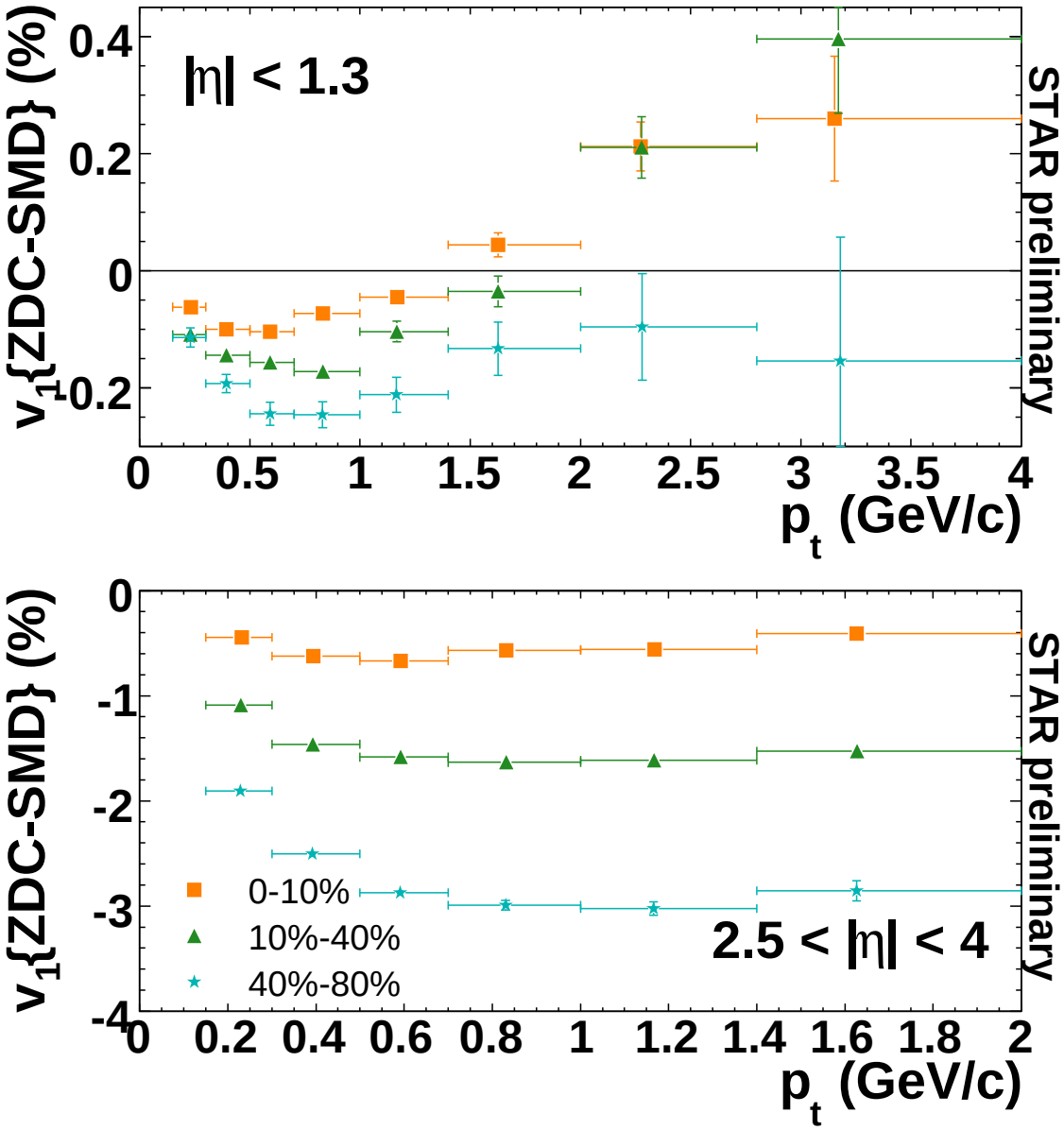

Figure 7.12: The upper panel shows $v_1\{\text{ZDC-SMD}\}$ versus p_t measured in the main TPC ($|\eta| < 1.3$), for centrality 10%–70% in 200 GeV AuAu. The lower panel shows $v_1\{\text{ZDC-SMD}\}$ versus p_t measured in the Forward TPCs ($2.5 < |\eta| < 4.0$), for different centralities in 200 GeV AuAu. The differential directed flow of particles with negative η has been changed in sign as stated in the text. Note the different scales on both axes for the two panels.

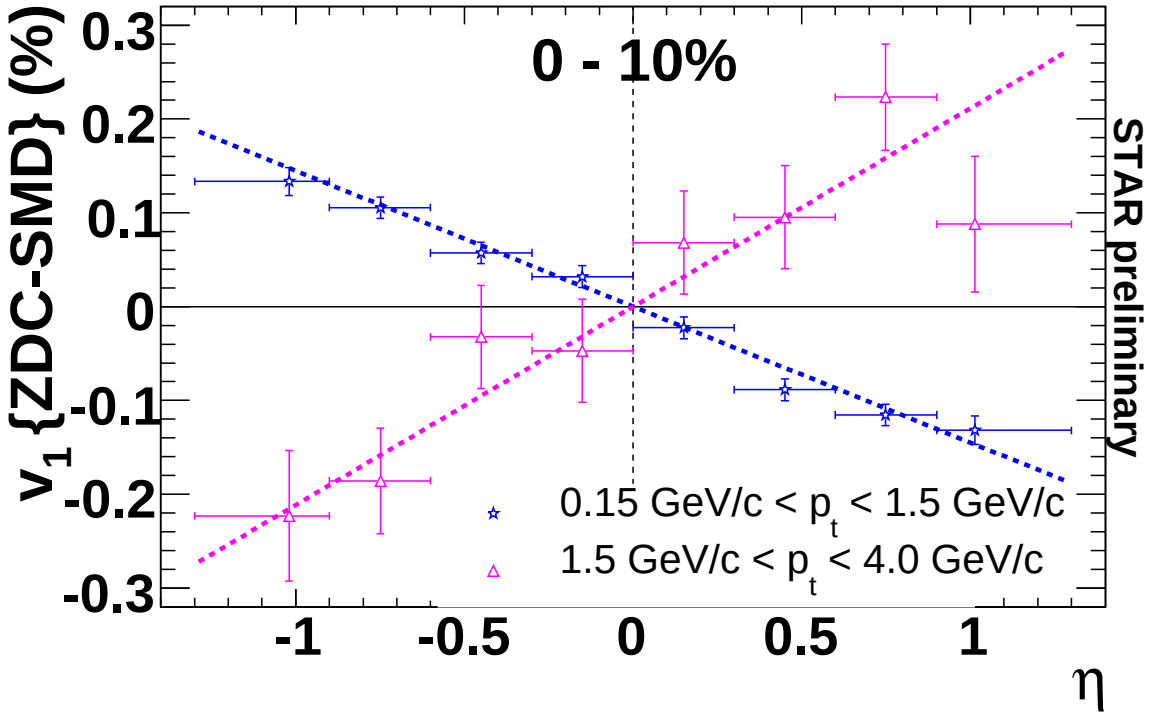

Figure 7.13: Charged-particle $v_1\{\text{ZDC-SMD}\}$ as a function of η measured in the main TPC with different p_t cuts, in 200 GeV AuAu central collisions.

as a function of η measured in the main TPC with different p_t cuts. For 0.15 GeV$/c < p_t <$ 1.5 GeV$/c$, charged-particle $dv_1/d\eta$ is negative, about -0.0014 ± 0.0001, and for 1.5 GeV$/c < p_t <$ 4 GeV$/c$, charged-particle $dv_1/d\eta$ is positive, about 0.0021 ± 0.0004. One possibility is that all types of charged particles have the same behavior in $v_1(p_t)$. That is, $v_1(p_t)$ is negative at low p_t, with the magnitude increasing with p_t, and after some turning point, approaches zero and crosses zero to become positive. Another possibility is that different types of charged particle could have v_1 of opposite sign for all p_t. In this scenario, a change in relative abundances as a function of p_t leads to the sign change of $v_1(p_t)$ of all charged particles. For example, if proton $v_1(p_t)$ is always positive and pion $v_1(p_t)$ is always negative, then the yield-averaged $v_1(p_t)$ of protons and pions could be negative at low p_t, where pions dominate, and could become positive at higher p_t, where the change in the relative abundances favors protons.

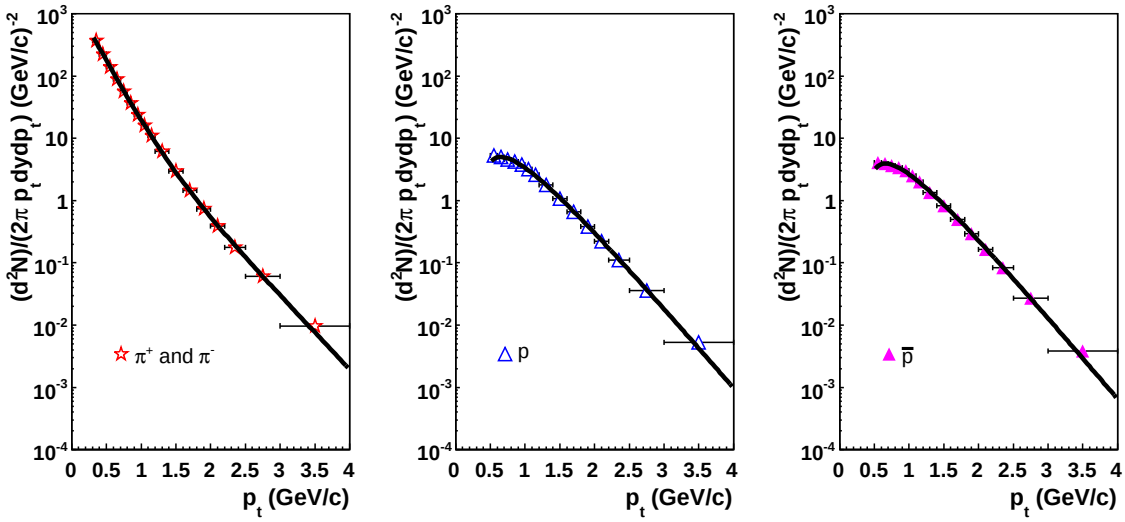

Figure 7.14: Yields of pions, protons and anti-protons versus p_t in 200 GeV AuAu central collisions (0 - 10%), measured in the main TPC. The yields are fit using the sum of two exponential functions.

Fig. 7.14 shows the yields of pions, protons and anti-protons versus p_t in 200 GeV AuAu central collisions (0 - 10%), measured in the main TPC. We can fit the yields using the sum of two exponential functions. With the yield functions, we are able to calculate the yield ratio between

(anti-)protons and pions, and the ratio between anti-protons and protons. The results are displayed in Fig. 7.15. The yield ratio between (anti-)protons and pions increases with p_t and reaches its peak around $p_t \approx 2.5$ GeV$/c$, where the yield ratio is bigger than one, i.e., there are more (anti-)protons than pions. The yield ratio between anti-protons and protons is more stable, between 0.7 and 0.8.

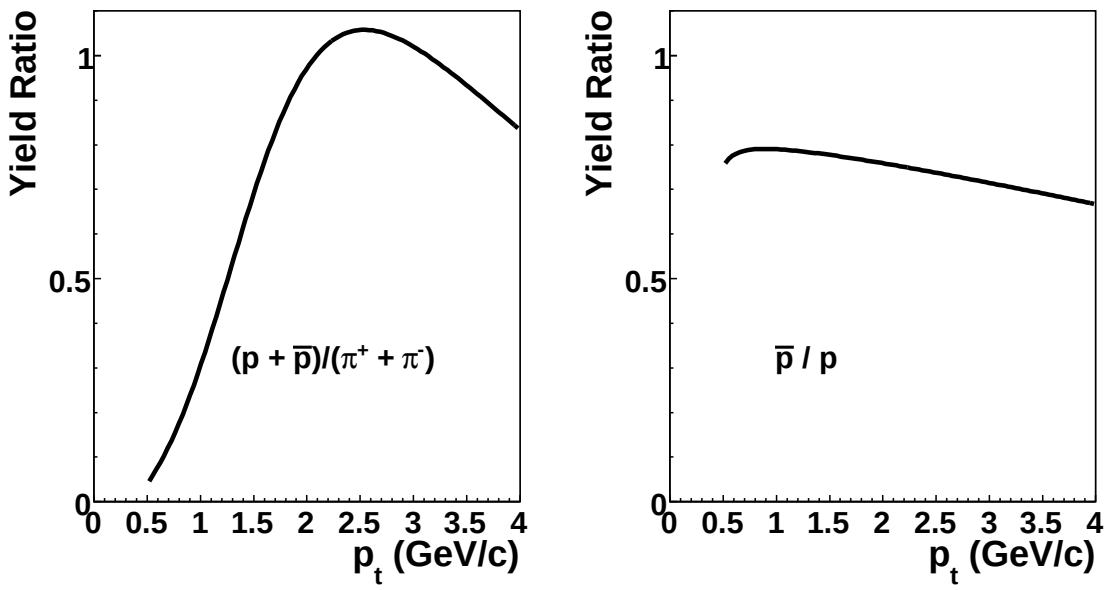

Figure 7.15: Yield ratios between (anti-)protons and pions (left panel), and between anti-protons and protons (right panel) versus p_t in 200 GeV AuAu central collisions (0- 10%), measured in the main TPC.

In the following analysis, we consider only pions, protons and anti-protons, and assume that all other types of particles can be neglected. We assume that $v_1(p_t)$ for pions, protons and anti-protons are all linear functions of p_t (straight lines) starting from the original point, so each function is governed by only one parameter, its slope. We expect this assumption to be valid up to some intermediate value of p_t. Then charged-particle $v_1(p_t)$ is the yield-weighted average of $v_1(p_t)$ for pions, protons and anti-protons, with three unknown parameters. If we assume that anti-protons flow with protons, that is, they have the same slope in $v_1(p_t)$, then only two unknown parameters are left in charged-particle $v_1(p_t)$. Thus we can fit the data points of charged-particle $v_1(p_t)$ with

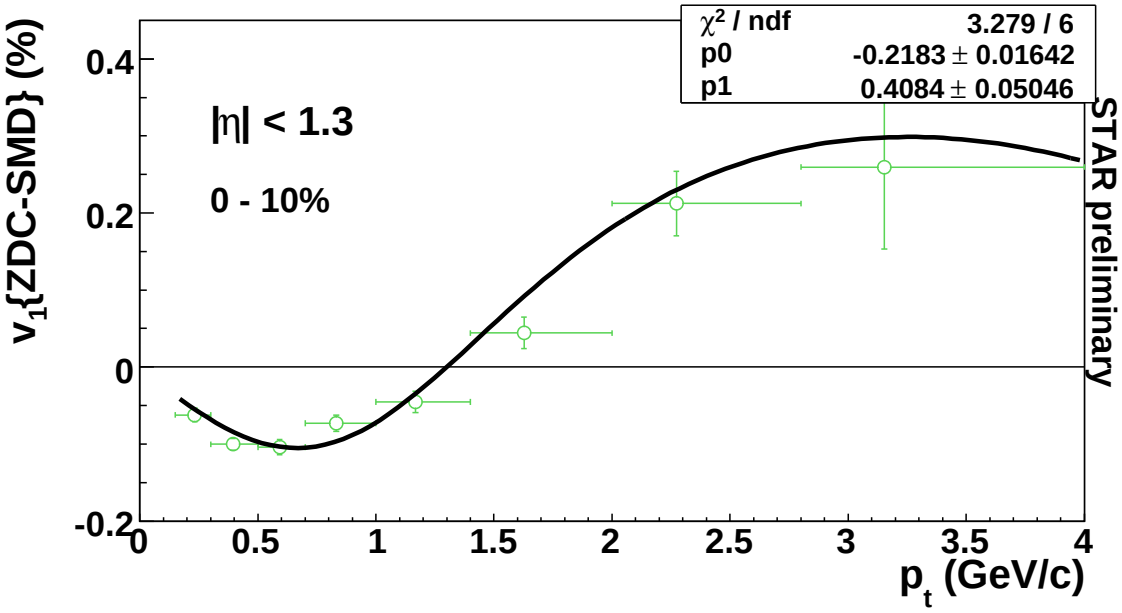

Figure 7.16: Charged-particle $v_1\{\text{ZDC-SMD}\}$ as a function of p_t in 200 GeV AuAu central collisions (0 - 10%), measured in the main TPC, can be fit using yields of pions and (anti-)protons, assuming anti-protons flow with protons, as discussed in the text.

the function described above.

Centrality	dv_1/dp_t (%) ($\overline{p}$ with p)	dv_1/dp_t (%) ($\overline{p}$ with π)
$0-10\%$	-0.218 ± 0.016	-0.216 ± 0.016
$10\% - 40\%$	-0.348 ± 0.022	-0.346 ± 0.022
$40\% - 80\%$	-0.444 ± 0.031	-0.442 ± 0.031

Table 7.3: The fitting parameters of pion dv_1/dp_t versus centrality in 200 GeV Au +Au collisions.

Fig. 7.16 shows one example of such fitting for charged-particle $v_1\{\text{ZDC-SMD}\}$ as a function of p_t in 200 GeV AuAu central collisions (0 - 10%), measured in the main TPC. In this case, the slope of pion $v_1(p_t)$ is negative, about -0.0022 ± 0.0002, and that of (anti-)proton $v_1(p_t)$ is positive, about 0.0041 ± 0.0005. In this way, the zero-crossing behavior of charged-particle $v_1(p_t)$ can be explained by the change in the yield ratio between (anti-)protons and pions.

Centrality	dv_1/dp_t (%) ($\overline{p}$ with p)	dv_1/dp_t (%) ($\overline{p}$ with π)
$0-10\%$	0.408 ± 0.050	0.871 ± 0.100
$10\% - 40\%$	0.541 ± 0.066	1.194 ± 0.125
$40\% - 80\%$	0.380 ± 0.077	1.003 ± 0.156

Table 7.4: The fitting parameters of proton dv_1/dp_t versus centrality in 200 GeV Au +Au collisions.

We can also assume that anti-protons flow with pions, and run through the same analysis. Table 7.3 and 7.4 show the fitting results for the two cases, and for three centrality bins. To know the exact values and shapes of proton $v_1(p_t)$ and pion $v_1(p_t)$, we need more investigation of well-separated particle species, and more statistics to reduce the errors. Currently, the fitting results give us a preliminary indication. Pion dv_1/dp_t varies very slightly from one case to the other, and increases in magnitude from central to peripheral collisions. Proton dv_1/dp_t is positive, and is more influenced by anti-proton dv_1/dp_t, due to the fact that the $\overline{p}/p$ ratio is comparable to 1. For both cases, proton dv_1/dp_t is biggest in mid-central collisions ($10\% - 40\%$).

Centrality	RefMult	Impact parameter (fm)
$80\% - 100\%$	< 14	$14.34 + 0.59 - 0.77$
$70\% - 80\%$	$14 - 30$	$12.87 + 0.62 - 0.52$
$60\% - 70\%$	$30 - 56$	$11.99 + 0.52 - 0.53$
$50\% - 60\%$	$56 - 94$	$11.05 + 0.47 - 0.52$
$40\% - 50\%$	$94 - 146$	$10.01 + 0.42 - 0.47$
$30\% - 40\%$	$146 - 217$	$8.81 + 0.42 - 0.42$
$20\% - 30\%$	$217 - 312$	$7.46 + 0.32 - 0.42$
$10\% - 20\%$	$312 - 431$	$5.77 + 0.31 - 0.32$
$5\% - 10\%$	$431 - 510$	$4.08 + 0.21 - 0.21$
$0 - 5\%$	> 510	$2.24 + 0.14 - 0.14$

Table 7.5: The reference multiplicity and the estimated impact parameter in each centrality bin for 200 GeV Au +Au collisions.

The centrality dependence of p_t-integrated v_1 is shown in Fig. 7.17. The values of the impact parameter were obtained using a Monte Carlo Glauber calculation [97], listed in Table 7.5. As expected, the magnitude of v_1 decreases with centrality. It is seen that v_1 in the more forward

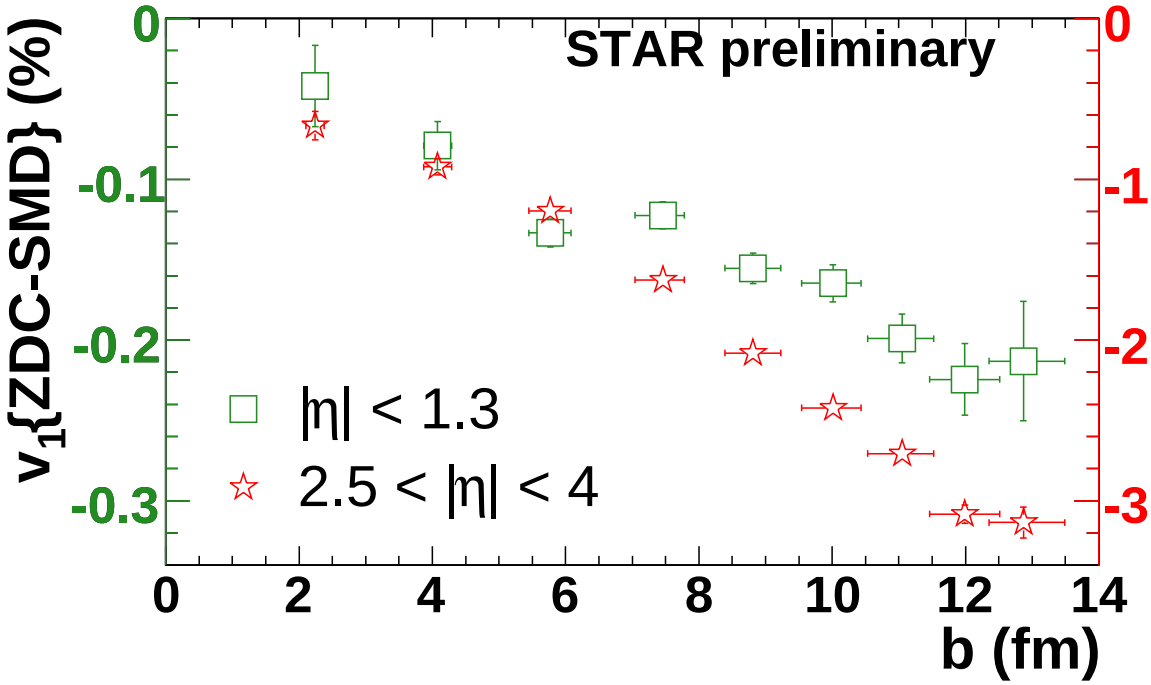

Figure 7.17: Directed flow for charged particles as a function of impact parameter in 200 GeV AuAu for the mid-pseudorapidity region ($|\eta| < 1.3$, with the left vertical scale) and the forward pseudorapidity region ($2.5 < |\eta| < 4.0$, with the right vertical scale). The differential directed flow of particles with negative η has been changed in sign as stated in the text.

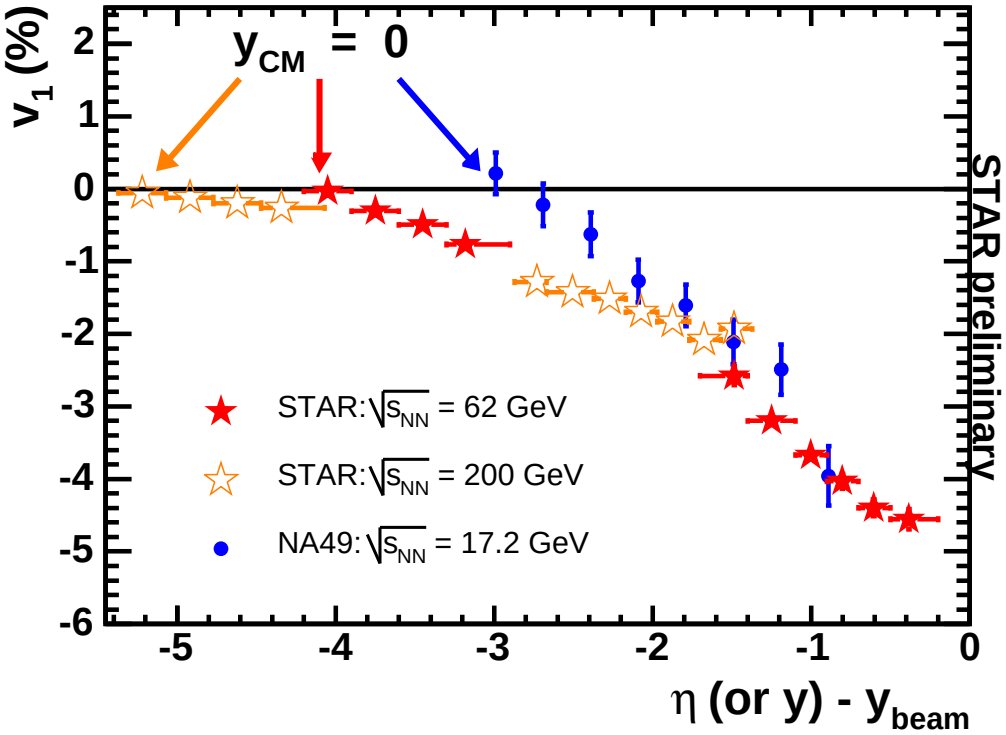

Figure 7.18: Charged-particle $v_1\{\text{ZDC-SMD}\}$ for Au +Au collisions $(10\% - 70\%)$ at 200 GeV [68] (open stars) and 62 GeV (solid stars), as a function of $\eta - y_{\text{beam}}$. Also shown are results from NA49 [92] (circles) for pions from 158A GeV midcentral $(12.5\% - 33.5\%)$ Pb +Pb collisions as a function of $y - y_{\text{beam}}$. The 62 GeV and 200 GeV points are averaged over the positive and negative rapidity regions.

pseudorapidity region $2.5 < |\eta| < 4.0$ varies more strongly with centrality than in the region closer to mid-pseudorapidity $(|\eta| < 1.3)$.

It has been observed that particle emission (both spectra and flow) as a function of rapidity difference with respect to beam rapidity appears unchanged over a wide range of beam energies [68, 98, 99], a pattern known as limiting fragmentation [69]. Fig. 7.18 presents v_1 results in the projectile frame for three beam energies. In this frame, zero on the horizontal axis corresponds to beam rapidity for each of the three beam energies. The data support the limiting fragmentation hypothesis in the region $-2 < (y - y_{\text{beam}}) < -1$. The three curves differ from each other at larger values of $|y - y_{\text{beam}}|$, but this is an unavoidable break-down of the limiting fragmentation hypothesis, because v_1 is constrained to cross zero at the $y_{\text{CM}} = 0$ points indicated by arrows in Fig. 7.18.

7.5 200 GeV Cu +Cu

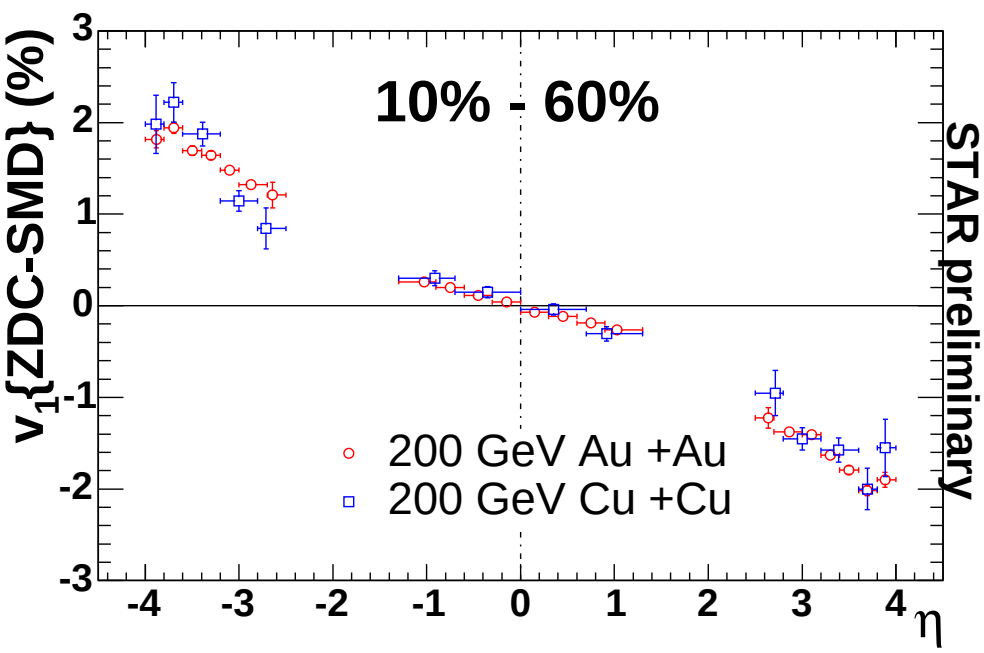

Figure 7.19: Charged-particle $v_1\{\text{ZDC-SMD}\}$ versus η for Cu +Cu collisions $(10\% - 60\%)$ at 200 GeV. The result for Au +Au collisions $(10\% - 60\%)$ at 200 GeV is shown for reference.

In RHIC run V (2005), a lighter collision system (Cu +Cu) was investigated at 200 GeV and 62

GeV. Since Cu and Au have different sizes, comparisons between these two collision systems probes a new type of scaling, and provides new constraints on models. In particular, we can investigate what happens when we consider a fixed shape of the initial overlap "almond" in coordinate space, and reduce the number of participant nucleons in it. Fig. 7.19 presents charged-particle $v_1\{\text{ZDC-SMD}\}$ versus η for Cu +Cu collisions ($10\% - 60\%$) at 200 GeV. Two million minimum-bias events were used in the analysis. Since Cu is much smaller than Au, more peripheral events (higher than 60% centrality) have relatively low multiplicity, leading to too much fluctuation in the analysis. In very central collisions (lower than 10% centrality), the event plane resolution from the ZDC-SMD fails like in the case of Au +Au at 62 GeV. The result for Au +Au collisions with the same centrality range at the same collision energy is included on Fig. 7.19. Within the statistical errors, the two results are consistent with each other. In the TPC range, $v_1\{\text{ZDC-SMD}\}$ is a monotonic function of η for both cases, and in the FTPC range, the two curves turn back at the same η position. This result suggests that when the initial range of shapes of the participant almond is fixed, the directed flow does not change when the number of participants is reduced. There are various other possibilities for studying how flow changes between CuCu and AuAu, but the systematic investigation of CuCu collisions in STAR is still in a very early stage, and further work in this direction is not part of this dissertation.

Due to the low statistics we currently have, directed flow results for identified particles suffer from extensive statistical errors, and are not presented in this dissertation.

The transverse-momentum dependence of v_1 is shown in Fig. 7.20 for Cu +Cu collisions ($10\%-60\%$) at 200 GeV. The upper panel shows the result measured in the main TPC ($|\eta| < 1.3$), and the lower panel shows the result measured in the Forward TPCs ($2.5 < |\eta| < 4.0$). The results for Au +Au collisions ($10\% - 60\%$) at 200 GeV are shown as a reference. Again, $v_1\{\text{ZDC-SMD}\}$ for 200 GeV CuCu agrees with that for 200 GeV AuAu. The good agreement is especially striking in the FTPC range, where the errors are relatively small.

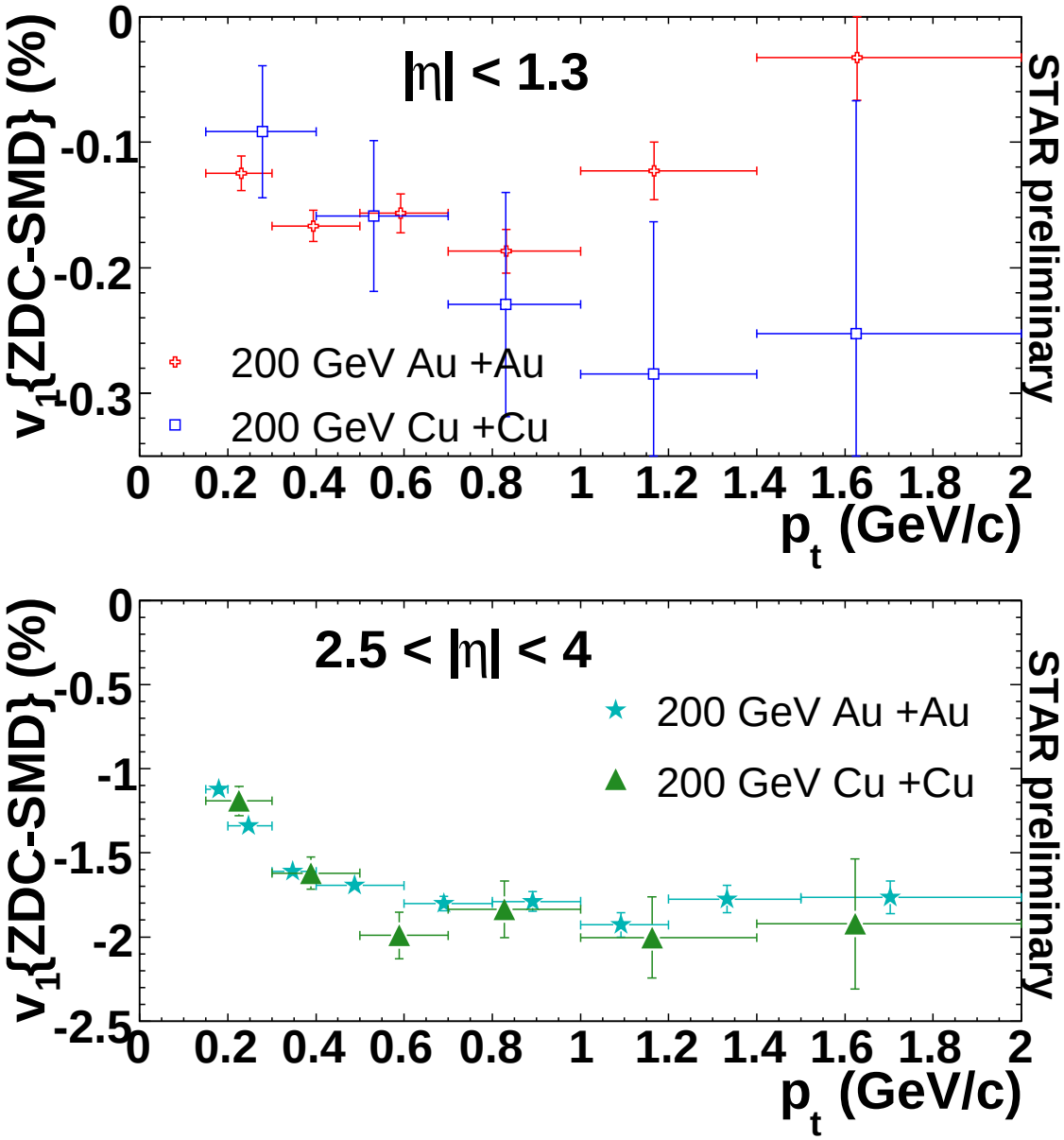

Figure 7.20: Charged-particle $v_1\{\text{ZDC-SMD}\}$ versus p_t for Cu +Cu collisions ($10\% - 60\%$ centrality) at 200 GeV. The upper panel shows the result measured in the main TPC ($|\eta| < 1.3$), and the lower panel shows the result measured in the Forward TPCs ($2.5 < |\eta| < 4.0$). The differential directed flow of particles with negative η has been changed in sign as stated in the text. The results for Au +Au collisions ($10\% - 60\%$ centrality) at 200 GeV are shown for reference.

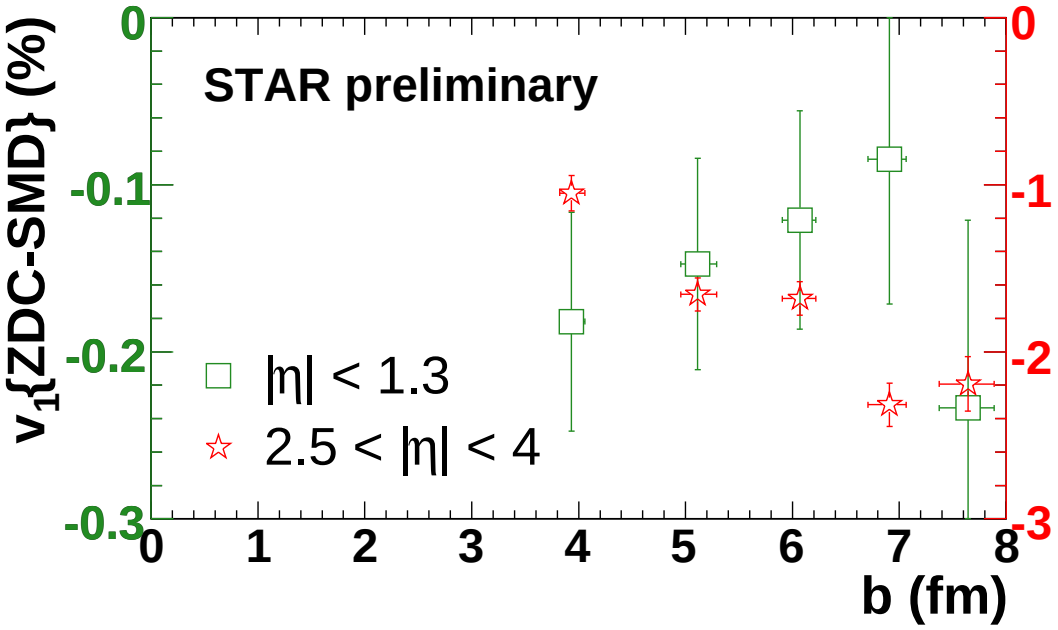

Figure 7.21: Directed flow for charged particles as a function of impact parameter in 200 GeV CuCu for the mid-pseudorapidity region ($|\eta| < 1.3$, with the left vertical scale) and the forward pseudorapidity region ($2.5 < |\eta| < 4.0$, with the right vertical scale). The differential directed flow of particles with negative η has been changed in sign as stated in the text.

The dependence of p_t-integrated v_1 on the impact parameter is shown in Fig. 7.21. The values of the impact parameter were obtained using a Monte Carlo Glauber calculation [97], listed in Table 7.6. It is seen that v_1 in the more forward pseudorapidity region $2.5 < |\eta| < 4.0$ varies more strongly with centrality (decreasing for more central collisions) than in the region closer to mid-pseudorapidity $(|\eta| < 1.3)$.

Fig. 7.22 plots p_t-integrated $v_1\{$ZDC-SMD$\}$ for charged particles as a function of centrality in 200 GeV CuCu in the forward pseudorapidity region ($2.5 < |\eta| < 4.0$). The result for 200 GeV AuAu is shown as a reference. For all the centralities where $v_1\{$ZDC-SMD$\}$ works for both collision systems, the results for CuCu and AuAu are very close to each other.

Centrality	RefMult	Impact parameter (fm)
$60\% - 100\%$	< 17	$8.71 + 0.25 - 0.27$
$50\% - 60\%$	$17 - 30$	$7.64 + 0.24 - 0.27$
$40\% - 50\%$	$30 - 47$	$6.91 + 0.16 - 0.20$
$30\% - 40\%$	$47 - 69$	$6.07 + 0.15 - 0.17$
$20\% - 30\%$	$69 - 98$	$5.11 + 0.18 - 0.16$
$10\% - 20\%$	$98 - 138$	$3.93 + 0.13 - 0.11$
$0\% - 10\%$	> 138	$2.40 + 0.05 - 0.05$

Table 7.6: The reference multiplicity and the estimated impact parameter in each centrality bin for 200 GeV Cu +Cu collisions.

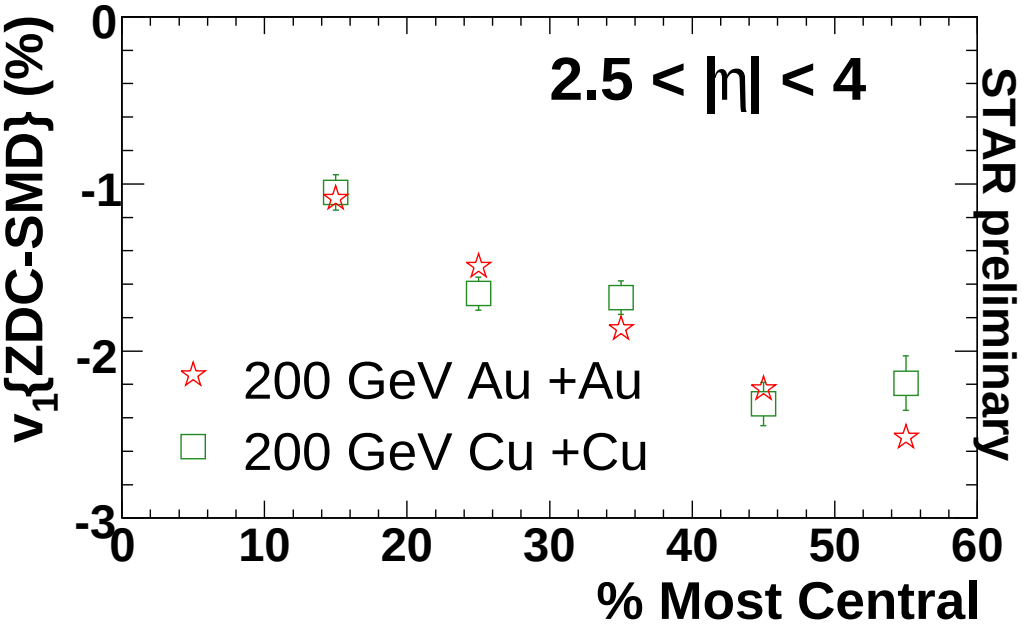

Figure 7.22: Directed flow for charged particles as a function of centrality in 200 GeV CuCu for the forward pseudorapidity region ($2.5 < |\eta| < 4.0$). The differential directed flow of particles with negative η has been changed in sign as stated in the text. The result for 200 GeV AuAu is shown for reference.

Chapter 8

Flow Results II: Elliptic Flow

The 1st-order event plane from the ZDC-SMD can also be utilized in elliptic flow analysis. However, the event plane resolution for v_2 calculation (R_{12}) is worse than that for v_1 calculation (R_{11}), with the 1st-order event plane. R_{12} is roughly equal to $\frac{2}{\pi}R_{11}^2$. Further details can be found in Ref. [28]. For this reason, we focus on Au +Au collisions at 200 GeV in this chapter, and v_2 for Au +Au at lower energies and for Cu +Cu are not considered.

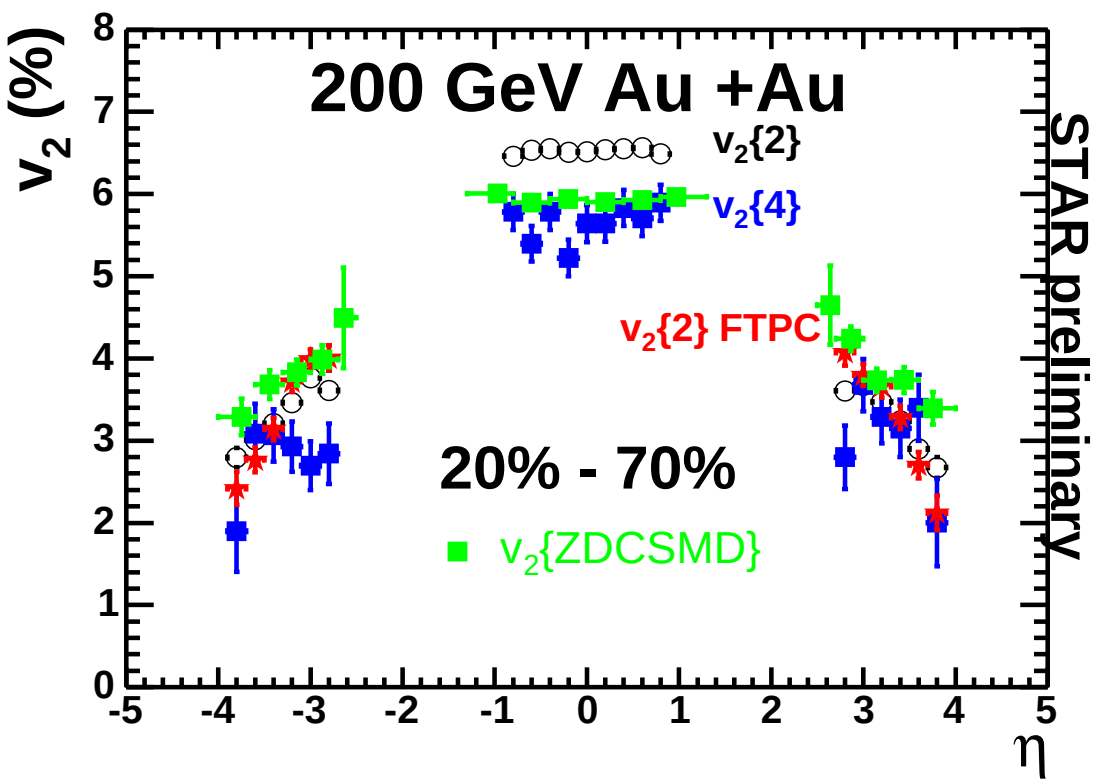

Figure 8.1: Elliptic flow for charged particles as a function of pseudorapidity, for centrality $20\% - 70\%$ in 200 GeV AuAu. The results from methods other than $v_2\{\text{ZDC-SMD}\}$ are from Ref. [57].

Fig. 8.1 shows elliptic flow for charged particles as a function of pseudorapidity, for centrality $20\% - 70\%$. The results from methods other than $v_2\{\text{ZDC-SMD}\}$ are from Ref. [57]. $v_2\{2\}$ is the two-particle cumulant method, equivalent to the standard reaction plane method [57, 100]. $v_2\{4\}$ in elliptic flow is the counterpart of $v_1\{3\}$ in directed flow, and is believed to greatly suppress non-flow effects. $v_2(\eta)$ is almost constant in the TPC range, and decreases with the magnitude of η in the FTPC range. The difference between $v_2\{2\}$ and $v_2\{4\}$ is likely due to non-flow effects and flow fluctuations [100]. According to our current understanding of these two systematic effects, the true v_2 probably lies between $v_2\{4\}$ and approximately the average of $v_2\{2\}$ and $v_2\{4\}$ [101], and that's where the points of $v_2\{\text{ZDC-SMD}\}$ are in the main TPC range. In the FTPC range, $v_2\{\text{ZDC-SMD}\}$ is more consistent with "$v_2\{2\}$ FTPC", which uses only FTPC particles.

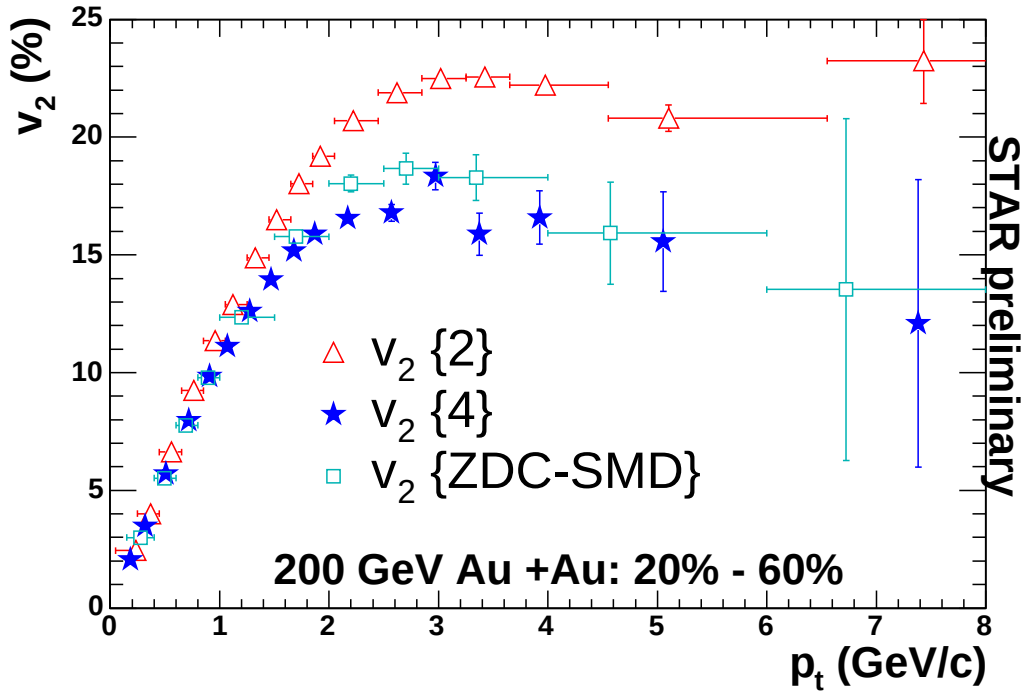

Figure 8.2: Elliptic flow for charged particles as a function of transverse momentum measured in the main TPC, for centrality $20\% - 60\%$ in 200 GeV AuAu. The results from methods other than $v_2\{\text{ZDC-SMD}\}$ are from Ref. [101].

Fig. 8.2 shows elliptic flow for charged particles as a function of transverse momentum measured in the main TPC, for centrality $20\% - 60\%$. The results from methods other than $v_2\{$ZDC-SMD$\}$ are from Ref. [101]. For all three results, $v_2(p_t)$ increases with p_t until 3 GeV$/c$. The gap between $v_2\{2\}$ and $v_2\{4\}$ increases with p_t, and $v_2\{$ZDC-SMD$\}$ is between them, closer to $v_2\{4\}$.

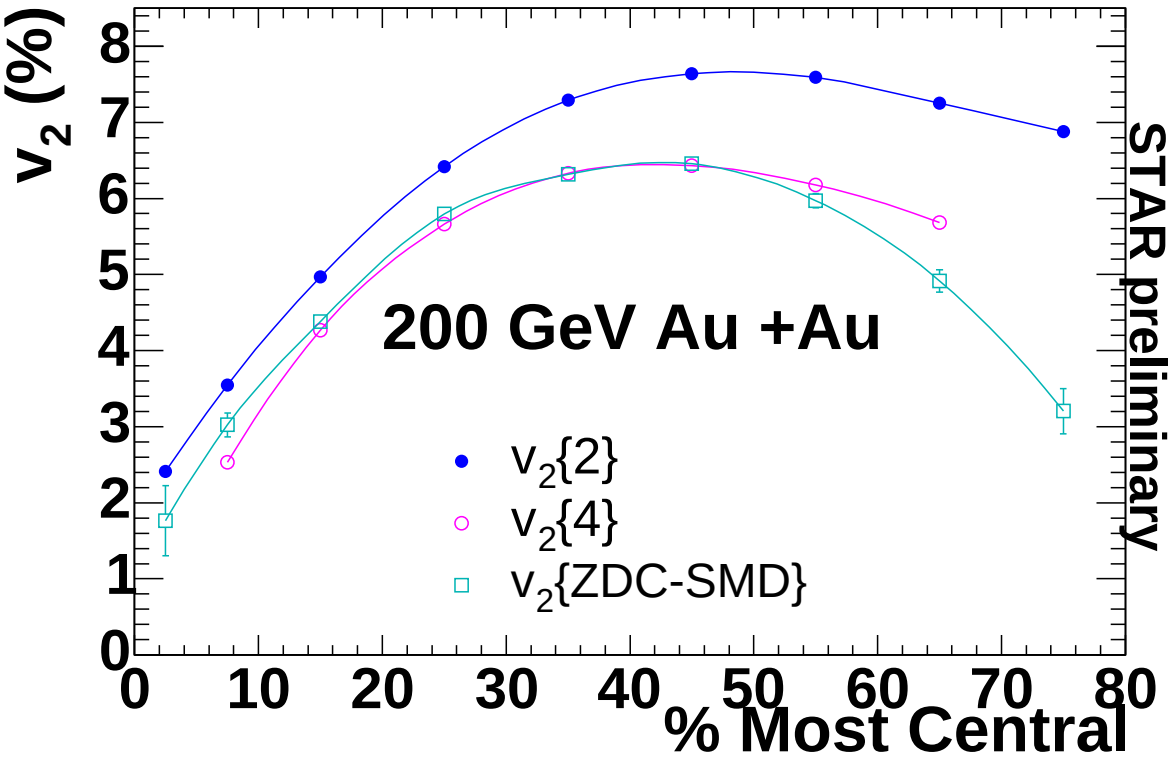

Figure 8.3: Charged particle v_2 integrated over p_t and η versus centrality measured in the main TPC in 200 GeV AuAu. The results from methods other than $v_2\{$ZDC-SMD$\}$ are from Ref. [57].

Fig. 8.3 shows charged-particle v_2, integrated over p_t and η, versus centrality measured in the main TPC in 200 GeV AuAu. The results from methods other than $v_2\{$ZDC-SMD$\}$ are from Ref. [57]. For all three methods, the integrated v_2 is higher in mid-peripheral collisions, and lower in central and peripheral collisions. The difference between $v_2\{2\}$ and $v_2\{4\}$ becomes bigger for more peripheral collisions. $v_2\{$ZDC-SMD$\}$ is consistent with $v_2\{4\}$ for mid-peripheral collisions, but in central and peripheral collisions, where $v_2\{4\}$ might be affected by bigger flow fluctuation,

they have significant differences.

Chapter 9

Summary and Outlook

Anisotropic flow sheds light on the early partonic stage in high-energy heavy-ion collisions. To minimize various systematic effects that in practice set a limit on how accurately flow can be measured, we have built a new detector subsystem called ZDC-SMD and developed a new method to reconstruct the reaction plane from the sideward deflection of spectator neutrons.

In early 2004, we installed two ZDC-SMDs in STAR, and since then, they have added significant capability to STAR in four areas of physics: anisotropic flow, strangelet searching, ultra-peripheral collisions, and spin physics. After calibrations such as pedestal subtraction, gain correction and location of the $p_t = 0$ point, the ZDC-SMD has performed reliably, with an energy resolution of about 29% and a beam position sensitivity on the order of 100 μm.

This work focuses on the contribution of the ZDC-SMD to the estimation of the 1st-order event plane used in anisotropic flow analysis. The 1st-order event plane resolution (a "quality factor" such that 100% represents perfect reaction plane determination) is between $30\% - 40\%$ for AuAu collisions at 200 GeV, and is just under 20% for AuAu collisions at 62 GeV and for CuCu collisions. Since the east and west ZDC-SMDs are rectangular hit-based detectors, the event plane information from them (after a flattening technique) can be utilized in 4 separate flow terms, with various corrections applied to each term independently. The new method $v_n\{\text{ZDC-SMD}\}$ has proven itself to be reliable as evidenced by internal consistencies, and by agreement with independent methods.

In the directed flow analysis, we studied all charged particles and two types of identified particles (pions and protons) in:

- 62 GeV AuAu: Three methods were used to measure charged-particle v_1 in 62 GeV AuAu

collisions, and the results agree very well with each other. Charged particles in the pseudorapidity region covered by the STAR TPC and FTPCs (up to $|\eta| = 4.0$) flow in the opposite direction to the fragmentation nucleons with the same sign of η. Over the pseudorapidity range studied, no sign change in the slope of charged-particle v_1 versus pseudorapidity is observed at any centrality. Transport models underpredict the charged-particle $v_1(\eta)$ within a unit or so of mid-pseudorapidity, but then come into good agreement with the data over the region 2.5 $< |\eta| <$ 4.0. The p_t-dependence of v_1 saturates above $p_t \approx$ 1 GeV$/c$ in the mid-pseudorapidity region and above $p_t \approx$ 0.5 GeV$/c$ in the forward pseudorapidity region. The centrality dependence of v_1 in the region of 2.5 $< |\eta| <$ 4.0 is found to be stronger than what is observed closer to mid-pseudorapidity.

Pion v_1 is found to follow the pattern of charged-particles v_1 at mid-rapidities in Au +Au collisions. The slope of proton v_1 has the same sign as that of pion v_1 at mid-rapidities in intermediate-centrality Au+Au collisions at 62 GeV, which if confirmed with better statistical significance, could be evidence of a "wiggle" structure, similar to what is shown in the left panel of Fig. 2.5. As discussed previously, certain models under certain conditions predict a wiggle, but not all wiggle predictions are attributed to a QGP. One-fluid hydrodynamic calculations have been used to argue that the observation of v_1 having the same sign for protons and pions near midrapidity would be a signature of a first-order phase transition. Details of the wiggle systematics will likely give us the ability to distinguish among the competing predictions and hence arrive at a conclusion that is relevant to QGP.

- 200 GeV AuAu: charged-particle $v_1\{$ZDC-SMD$\}$ in 200 GeV AuAu collisions has a smaller magnitude than in 62 GeV AuAu collisions, and approaches zero within the pseudorapidity region studied in central collisions. The pattern of v_1 approaching zero at $|\eta| \approx 3.8$ show some of the expected characteristics of the wiggle signature, but a definite interpretation must wait for further investigation. If v_1 approaches zero close to the spectator rapidities, this is

an unremarkable effect predicted by all models, and could be due to a change in the relative abundances of protons and pions at forward pseudorapidities, where proton v_1 and pion v_1 likely have opposite signs, but neither might have a wiggle shape. A separate measurement for pions and for protons or another baryon species would be very informative. In addition to needing experimental clarifications as mentioned above, we also need further input from models.

The p_t-dependence of v_1 saturates above $p_t \approx$ 1.1 GeV$/c$ in the forward pseudorapidity region. In the mid-pseudorapidity region, we observe charged-particle $v_1(p_t)$ crosses zero at $p_t \approx 1.5$ GeV$/c$ for centrality $0 - 10\%$, and at $p_t \approx 2$ GeV$/c$ for centrality $10\% - 40\%$. A fitting method using yields of pions and (anti-)protons gives us some indication that pions and protons could flow in opposite directions, and the change in their relative abundances leads to the sign change in charged-particle $v_1(p_t)$. The rapidity dependence of v_1 provides further support for the limiting fragmentation picture.

- 200 GeV CuCu: $v_1\{$ZDC-SMD$\}$ in 200 GeV CuCu collisions is consistent with that in 200 GeV AuAu collisions as a function of both η and p_t. The two systems are very close in integrated v_1 values versus centrality. This "scaling" behavior will be further tested between AuAu and CuCu collisions at 62 GeV in the future.

In elliptic flow analysis, we concentrated on 200 GeV AuAu collisions. $v_2\{$ZDC-SMD$\}$ falls between $v_2\{2\}$ and $v_2\{4\}$, and closer to $v_2\{4\}$ as a function of both η and p_t. The integrated $v_2\{$ZDC-SMD$\}$ is consistent with $v_2\{4\}$ in mid-peripheral collisions, and differs from $v_2\{4\}$ in central and peripheral collisions, where $v_2\{4\}$ might be affected by flow fluctuations.

In future RHIC runs, much larger event samples will be collected, and subsystem upgrades to the STAR detector will greatly improve particle identification. Then both v_1 and v_2 for more species of identified particles with excellent statistics can be studied, for different ion pairs at different beam energies. For example, the evidence for partonic collectivity (Fig. 2.6) can be revisited

using $v_2\{\text{ZDC-SMD}\}$ and possibly also $v_1\{\text{ZDC-SMD}\}$, to probe the scaling picture with non-flow effects fully suppressed.

There is general agreement in the heavy-ion collision community that a new form of matter is being produced at RHIC, and that it has many of the characteristics expected of a strongly-interacting Quark-Gluon Plasma (sQGP). Several prominent theorists argue that the sQGP is therefore already discovered, and that we are now in the follow-on stage of studying the properties of this new phase of matter. However, in the STAR collaboration, there is broad agreement that the present measurements by themselves do not yet offer sufficiently strong evidence for QGP. We remain optimistic that fully convincing evidence will be gathered during the next round of data-taking. A similar position has been taken by the other three experimental collaborations at RHIC.

The partonic flow argument outlined in Section 2.2 is considered one of the highlights from RHIC to date, namely that the scaling behavior of $v_2(p_t)$ for different particle types according to their respective number of constituent quarks at intermediate p_t ("NCQ scaling") indicates that there must have been a partonic stage early in the collision. Furthermore, the hydro-like scaling of $v_2(p_t)$ with particle mass observed at lower p_t also has been used to argue that we are observing an sQGP. These critically important measurements came to light two to three years after the initial elliptic flow studies in the year 2000 [102]. Now we are just beginning to study directed flow at RHIC — the main topic of this dissertation — and the situation for this more challenging type of anisotropy is quite similar to elliptic flow five years ago, when that measurement was first carried out for charged particles and the results for identified species still had very poor statistics. Therefore, we believe that it is too early to expect this work to have well-understood consequences for the "big picture" at RHIC, and in the meantime, we make the argument that the analysis in this dissertation has paved the way for the next round of v_1 measurements.

References

[1] T D Lee, *Particle Physics and Introduction to Field Theory.* Harwood Academic Publisher, Chur, Switzerland (1981)

[2] For reviews and recent developments, see Quark Matter 2004 proceedings. (2004).

[3] K. Geiger, Thermalization in ultrarelativistic nuclear collisions. I. Parton kinetics and quark-gluon plasma formation. *Phys. Rev.* **D46**, 4965 (1992).

[4] A Dumitru, U. Katscher, J. A. Maruhn, H. Stöcker, W. Greiner and D. H. Rischke, Thermal photons as a measure for the rapidity dependence of the temperature. *Z. Phys.* **A353**, 187 (1995)

[5] J. Alam, D. K.Srivastava, B. Sinha and D.N. Basu, Transverse flow effects on high-energy photons emitted by expanding quark-gluon plasma. *Phys. Rev.* **D48**, 1117 (1993)

[6] T. Matsui and H. Satz, J/ψ suppression by Quark - Gluon Plasma formation. *Phys. Lett.* **B178**, 416 (1986)

[7] F. Karsch, M. T. Mehr and H. Satz, Color screening and deconfinement for bound states of heavy quarks. *Z Phys.***C37**, 617 (1988)

[8] J. P. Bailly *et al.*, Strangeness and diquark suppression factors in 360-Gev/c p p interactions. *Phys. Lett* **B195**, 609 (1987)

[9] P. K. Malhotra and R. Orava, Measurement of strange quark suppression in hadronic vacuum. *Z. Phys.* **C17**, 85 (1983)

[10] T. Alberet *et al.*, Two pion Bose-Einstein correlations in nuclear collisions at 200-GeV per nucleon. *Z.Phys.* **C66**, 77 (1995)

[11] A. N. Makhlin and Y. M. Sinyukov, Hydrodynamics of hadron matter under pion interferometric microscope. *Z.Phys.* **C39**, 69 (1988)

[12] R. Hanbury-Brown and R. Q. Twiss, A New Type of Interferometer for Use in Radio Astronomy. *Phil. Mag.* **45**, 663 (1954)

[13] S. E. Koonin, Proton pictures of high-energy nuclear collisions. *Phys. Lett.* **B70**, 43 (1977)

[14] F. B. Yano and S. E. Koonin, Determining pion source parameters in relativistic heavy ion collisions. *Phys. Lett.* **B78**, 556 (1978)

[15] S. Pratt, Pion Interferometry for Exploding Sources. *Phys. Rev. Lett.* **53**, 1219 (1984)

[16] S. Pratt, Pion interferometry of Quark-Gluon Plasma. *Phys. Rev.* **D33**, 1314 (1986)

[17] U. Heinz, How to extract physics from HBT radius parameters. *Nucl.Phys.* **A610**, 264c (1996)

[18] M. H. Thoma and M. Gyulassy, High P(t) probes of nuclear collisions. *Nucl. Phys.***A538**, 37c (1991)

[19] S. Mrowczynski, Energy loss of a high-energy parton in the Quark - Gluon Plasma. *Phys.Lett.***B269**, 383 (1991)

[20] Y. Koike and T. Matsui, Passage of high-energy partons through a Quark-Gluon Plasma. *Phys. Rev.* **D45**, 3237 (1992)

[21] M. Gyulassy and M. Plumer, Jet quenching in dense matter. *Phy. Lett.* **B243**, 432 (1990).

[22] M. Gyulassy, I. Vitev, and X. N. Wang, High p_t Azimuthal Asymmetry in Noncentral A + A at RHIC. *Phy. Rev. Lett.* **86**, 2537 (2001).

[23] D. A. Appel, Jets as a probe of quark-gluon plasmas. *Phys. Rev.***D33**, 717 (1986)

[24] J. -Y. Ollitrault, Anisotropy as a signature of transverse collective flow. *Phys. Rev.* **D46**, 229 (1992).

[25] S. Voloshin and Y. Zhang, Flow study in relativistic nuclear collisions by fourier expansion of azimuthal particle distributions. *Z. Phys.* **C70**, 665 (1996).

[26] W. Reisdorf, and H. G. Ritter, Collective flow in heavy-ion collisions. *Annu. Rev. Nucl. Part. Sci.* **47**, 663 (1997).

[27] N. Herrmann, J. P. Wessels, and T. Wienold, Collective flow in heavy ion collisions. *Annu. Rev. Nucl. Part. Sci.* **49**, 581 (1999).

[28] A. M. Poskanzer and S. A. Voloshin, Methods for analyzing anisotropic flow in relativistic nuclear collisions. *Phys. Rev.* **C58**, 1671 (1998).

[29] J. -Y. Ollitrault, Flow systematics from SIS to SPS energies. *Nucl. Phys.* **A638**, 195c (1998).

[30] M. B. Tsang *et al.*, Deflection of nonequilibrium light particles by the nuclear mean field. *Phys. Rev Lett.***57**, 559 (1986)

[31] W. K. Wilson *et al.*, Azimuthal asymmetry in Ar+V collisions from E/A=35 to 85 MeV. *Phys. Rev.* **C41**, R1881 (1990)

[32] M.B. Tsang *et al.*, Measurement of complex fragments and clues to the entropy production from 42-MeV/nucleon - 137-MeV/nucleon Ar + Au. *Phys. Rev. Lett* **51**, 1846 (1983)

[33] C. B. Chitwood *et al.*, Light particle emission in 16 induced reactions on ^{12}C, ^{27}Al, and ^{197}Au at E/A=25 MeV. *Phys. Rev.* **C34**, 858 (1986)

[34] H. H. Gutbrod *et al.*, A new component of the collective flow in relativistic heavy ion collisions. *Phys. Lett.* **B216**, 267 (1989)

[35] M. M. Agarwal *et al.*, WA98 collaboration, Recent results on Pb+Pb collisions at 158 AGeV from the WA98 experimen t at CERN. *Nucl. Phys.* **A638**, 147c (1998)

[36] H. Appelshauser *et al.*, NA49 collaboration, Recent results on central Pb+pb collisions from experiment NA49. *Nucl. Phys.* **A638**, 91c (1998)

[37] F. Ceretto *et al.*, CERES collaboration, Hadron physics with ceres: spectra and collective flow. *Nucl. Phys.* **A638**, 467c (1998)

[38] C. M. Hung and E. V. Shuryak, Hydrodynamics near the QCD Phase Transition: Looking for the Longest-Lived Fireball. *Phys. Rev. Lett.* **75**, 4003 (1995).

[39] D.H. Rischke, Y. Pursun, J.A. Maruhn, H. Stöcker, and W. Greiner, The phase transition to the Quark - Gluon Plasma and its effects on hydrodynamic flow. *Heavy Ion Phys.* **1**, 309 (1995)

[40] L. P. Csernai and D. Rohrich, Third flow component as QGP signal. *Phys. Lett.* **B458**, 454 (1999)

[41] A. Nyiri *et al.*, Collective phenomena in heavy-ion collisions. *J. Phys.* **G31**, S1045 (2005).

[42] R.J. Snelling, H.Sorge, S.A. Voloshin, F.Q. Wang, N. Xu, Novel rapidity dependence of directed flow in high energy heavy ion collisions. *Phys. Rev. lett.* **84**, 2803 (2000)

[43] P. F. Kolb, J. Sollfrank, and U. Heinz, Anisotropic flow from AGS to LHC energies. *Phys. Lett.* **B459**, 667 (1999)

[44] P. F. Kolb, J. Sollfrank, P. V. Ruuskanen, and U. Heinz, Hydrodynamic simulation of elliptic flow. *Nucl. Phys.* **A661**, 349c (1999)

[45] S. A. Voloshin and A. M. Poskanzer, The physics of the centrality dependence of elliptic flow. *Phys. Lett. B* **474**, 27-32 2000

[46] H. Sorge, Highly Sensitive Centrality Dependence of Elliptic Flow: A Novel Signature of the Phase Transition in QCD. *Phys. Rev. Lett.* **82**, 2048 (1999)

[47] H. Heiselberg and A. -M. Levy, Elliptic flow and Hanbury-Brown-Twiss correlations in non-central nuclear collisions. *Phys. Rev.* **C59**, 2716 (1999).

[48] A. Bialas, M. Bleszynski, and W. Czyz, Multiplicity distributions in nucleus-nucleus collisions at high-energies. *Nucl. Phys.* **B111**, 461 (1976)

[49] STAR Collaboration, J. Adams *et al.*, Multi-strange baryon elliptic flow in Au+Au collisions at $\sqrt{s_{NN}}$ = 200 GeV. *e-print* nucl-ex/0504022 (2005).

[50] PHENIX Collaboration, S. S. Adler *et al.*, Elliptic Flow of Identified Hadrons in Au + Au Collisions at $\sqrt{s_{NN}}$ = 200 GeV. *Phys. Rev. Lett.* **91**, 182301 (2003)

[51] STAR Collaboration, J. Adams *et al.*, Particle-Type Dependence of Azimuthal Anisotropy and Nuclear Modification of Particle Production in Au + Au Collisions at $\sqrt{s_{NN}}$ = 200 GeV. *Phys. Rev. Lett.* **92**, 052302 (2004)

[52] X. Dong, S. Esumi, P. Sorensen, N. Xu, Z. Xu, Resonance decay effects on anisotropy parameters. *Phys. Lett.* **B597**, 328 (2004)

[53] P. Danielewicz and G. Odyniec, Transverse momentum analysis of collective motion in relativistic nuclear collisions. *Phys. Lett.* **B157**, 146 (1985)

[54] N. Borghini, P. M. Dinh, and J.-Y. Ollitrault Flow analysis from multiparticle azimuthal correlations. *Phys. Rev.* **C64**, 054901 (2001)

[55] N. Borghini, P. M. Dinh, and J.-Y. Ollitrault Analysis of directed flow from elliptic flow. *Phys. Rev.* **C66**, 014905 (2002)

[56] STAR Collaboration, J. Adams *et al.*, Anisotropic flow in the forward directions at $\sqrt{s_{NN}}$ = 200 GeV. *e-print* nucl-ex/0403007 (2004).

[57] STAR Collaboration, J. Adams *et al.*, Azimuthal anisotropy in Au+Au collisions at $\sqrt{s_{NN}}$ = 200 GeV. *Phys. Rev.* **C72** 014904 (2005).

[58] J. Harris *et al.*, STAR Detector Overview. *Nucl. Instr. Meth.* **A499**, 624 (2003).

[59] F. Bergsma *et al.*, The STAR Detector Magenet Subsystem. *Nucl. Instr. Meth.* **A499**, 629 (2003).

[60] M. Anderson *et al.*, The STAR Time Projection Chamber: A Unique Tool for Studying High Multiplicity Events at RHIC. *Nucl. Instr. Meth.* **A499**, 659 (2003).

[61] K.H. Ackerman *et al.*, The Forward Time Projection Chamber in STAR. *Nucl. Instr. Meth.* **A499**, 709 (2003).

[62] R. Bellwied *et al.*, The STAR Silicon Vertex Tracker. *Nucl. Instr. Meth.* **A499**, 636 (2003).

[63] F.S. Bieser *et al.*, The STAR Trigger. *Nucl. Instr. Meth.* **A499**, 766 (2003).

[64] C. Alder *et al.*, The RHIC Zero Degree Calorimeter. *Nucl. Instr. Meth.* **A470**, 488 (2001).

[65] STAR collaboration, K.H. Ackermann *et al.*, The STAR Time Projection Chamber. *Nucl. Phys.* **A661**, 681c (1999).

[66] The STAR Collaboration, J. W. Harris *et al.*, The STAR experiment at the relativistic heavy ion collider. *Nucl. Phys.* **A566**, 277c (1994).

[67] WA98, conference presentations and private communication.

[68] The STAR Collaboration, J. Adams *et al.*, Azimuthal anisotropy at the Relativistic Heavy Ion Collider: the first and fourth harmonics. *Phys. Rev. Lett.* **92**, 062301 (2004).

[69] J. Benecke *et al.*, Hypothesis of limiting fragmentation in high-energy collisions. *Phys. Rev.* **188**, 2159 (1969).

[70] E. Witten, Cosmic separation of phases. *Phys. Rev.* **D30**, 272 (1984).
E. Farhi and R.L. Jaffe, Perhaps a stable Dihyperon. *Phys. Rev. Lett.* **38**, 195 (1977).
S.A. Chin and A.K. Kerman, Possible long-lived hyperstrange multiquark droplets. *Phys. Rev. Lett.* **43**, 1292 (1979).
J. Schaffner *et al.*, Separation of strangeness from antistrangeness in the phase transition from quark to hadron matter: Possible formation of strange quark matter in heavy-ion collisions. *Phys. Rev. Lett.* **58**, 1825 (1992).

[71] R. Klingenberg, Strange quark matter searches. *J. Phys.* **G25**, R273 (1999).

[72] G. Baur *et al.*, Multiphoton exchange processes in ultraperipheral relativistic heavy ion collisions. *Nucl. Phys.* **A729** 787 (2003).

[73] D. W. Duke and J. F. Owens, Linearly-polarized-photon asymmetry predictions for inelastic J/psi photoproduction. *Phys. Rev.* **D24**, 1403 (1981).

[74] G. Bunce *et al.*, Prospects for spin physics at RHIC. *Ann. Rev. Nucl. Part. Sci.* **50**, 525 (2000). L.C. Bland, Spin Physics at RHIC. 15th International Spin Physics Symposium SPIN2002, AIP Conference Proceedings.

[75] B. Christie, S. White, P. Gorodetzky, D. Lazic, Calorimetry at zero degrees in RHIC: some issues in the choice of detector technology. STAR Note SN0175.

[76] http://usa.hamamatsu.com/hcpdf/parts_H/H6568_series.pdf
http://www.phenix.bnl.gov/phenix/WWW/publish/togawa/localpol/smd/H6568.pdf

[77] P. Danielewicz, Effects of compression and collective expansion on particle emission from central heavy-ion reactions. *Phys. Rev.* **C51**, 716 (1995).

[78] J. Barrette *et al.*, E877 Collaboration, Proton and pion production relative to the reaction plane in Au + Au collisions at 11A GeV/c. *Phys. Rev.* **C56**, 3254 (1997).

[79] H. Sorge, Flavor production in Pb(160A FeV) on Pb collisions: effect of color raopes and hadronic rescattering. *Phys. Rev.* **C52**, 3291 (1995).

[80] H. Sorge, Elliptical flow: a signature for early pressure in ultrarelativistic nucleus-nucleus collisions. *Phys. Rev. Lett* **78**, 2309 (1997).

[81] H. Sorge, Temperatures and non-ideal expansion in ultrarelativistic nucleus-nucleus collisions. *Phys. Lett* **B373**, 16 (1996).

[82] H. Sorge, H. Stocker, and W. Greiner, Poincar'e invariant hamiltonian dynamics: modelling multi-hadronic inter-actions in a phase space approach. *Ann. Phys. (N.Y.)* **192**, 266 (1989).

[83] H. Bebie, P. Gerber, J. L. Goity, and H. Leutwyler, The role of the entropy in an expanding hadronic gas. *Nucl. Phys.* **B378**, 95 (1992).

[84] S.A. Bass *et al.*, Microscopic models for ultrarelativistic heavy ion collisions. *Prog. Part. Nucl. Phys.* **41**, 225 (1998); M. Bleicher *et al.*, Relativistic hadron-hadron collisions in the ultra-relativistic quantum molecular dynamics model (UrQMD). *J. Phys.* **G25**, 1859 (1999); X.-L. Zhu, private communication (2005).

[85] Z.W. Lin and C.M. Ko, Partonic effects on the elliptic flow at relativistic heavy ion collisions. *Phys. Rev.* **C65**, 034904 (2002); L.-W. Chen and C.-M. Ko, Partonic effects on anisotropic flows at RHIC. *J. Phys.* **G31**, S49 (2005); L.-W. Chen, private communication (2005).

[86] X. N. Wang and M. Gyulassy, HIJING: A Monte Carlo model for multiple jet production in pp, pA, and AA collisions. *Phys. Rev.* **D44**, 3501 (1991).

[87] B. Zhang, ZPC 1.0.1: a parton cascade for ultrarelativistic heavy ion collisions. *Comput. Phys. Commun.* **109**, 193 (1998).

[88] T. Sjostrand, High-energy physics event generation with PYTHIA 5.7 and JETSET 7.4. *Comput. Phys. Commun.* **82**, 74 (1994).

[89] B. A. Li and C.M. Ko, Formation of superdense hadronic matter in high energy heavy-ion collisions. *Phys. Rev.* **C52**, 2037 (1995).

[90] J. Brachmann *et al.*, Antiflow of nucleons at the softest point of the equation of state. *Phys. Rev.* **C61**, 024909 (2000).

[91] H. Stoker, Collective flow signals the Quark Gluon Plasma. *Nucl. Phys.* **A750** 121 (2005).

[92] NA49 Collaboration, C. Alt *et al.*, Directed and elliptic flow of charged pions and protons in Pb+Pb collisions at 40A and 158A GeV. *Phys. Rev.* **C68**, 034903 (2003).

[93] WA98 Collaboration, M.M. Aggarwal *et al.*, Directed Flow in 158 A GeV Pb + Pb Collisions. *e-print* nucl-ex/9807004 (1998).

[94] M. Bleicher and H. Stoker, Anisotropic flow in ultra-relativistic heavy ion collisions. *Phys. Lett.* **B526** 309 (2002).

[95] PHOBOS Collaboration, B.B. Back *et al.*, Flow in Au+Au collisions at RHIC. *J. Phys.* **G30** S1243 (2004).

[96] PHOBOS Collaboration, B. Alver *et al.*, Systematic study of directed flow at RHIC energies. *e-print* nucl-ex/0510030.

[97] B.B. Back *et al.*, Centrality dependence of charged particle multiplicity at midrapidity in Au+Au collisions at $\sqrt{s_{NN}}$ = 130 GeV. *Phys. Rev.* **C65**, 031901(R) (2002); K. Adcox *et al.*, Centrality Dependence of Charged Particle Multiplicity in Au-Au Collisions at $\sqrt{s_{NN}}$ = 130 GeV. *Phys. Rev. Lett* **86**, 3500 (2001); I.G. Bearden *et al.*, Charged particle densities from Au+Au collisions at $\sqrt{s_{NN}}$ = 130 GeV. *Phys. Lett.* **B523**, 227 (2001); STAR Collaboration, J. Adams *et al.*, Production of Charged Pions and Hadrons in Au+Au Collisions at $\sqrt{s_{NN}}$ = 130 GeV. *e-print* nucl-ex/0311017.

[98] PHOBOS Collaboration, B.B. Back *et al.*, Significance of the fragmentation region in ultrarelativistic heavy-ion collisions. *Phys. Rev. Lett* **91**, 052303 (2003); Energy dependence of elliptic flow over a large pseudorapidity range in Au+Au collisions at the BNL relativistic heavy ion collider. ibid. **94**, 122303 (2005).

[99] STAR Collaboration, J. Adams *et al.*, Multiplicity and pseudorapidity distributions of photons in Au+Au collisions at $\sqrt{s_{NN}}$ = 62.4 GeV. *Phys. Rev. Lett* **95**, 062301 (2005).

[100] STAR Collaboration, C. Adler *et al.*, Elliptic flow from two- and four-particle correlations in Au+Au collisions at $\sqrt{s_{NN}}$ = 130 GeV. *Phys. Rev.* **C66**, 034904 (2002).

[101] STAR Collaboration, J. Adams *et al.*, Azimuthal anisotropy and correlations at transverse momenta in p + p and Au+Au collisions at $\sqrt{s_{NN}}$ = 200 GeV. *Phys. Rev. Lett.* **93** 252301 (2004).

[102] STAR collaboration, K.H. Ackermann *et al.*, Elliptic Flow in Au + Au Collisions at $\sqrt{s_{NN}}$ = 130 GeV. *Phys. Rev. Lett.* **86**, 402 (2001).

Appendix A

The Quark Model

The quark model describes nucleons and other hadrons as consisting of quarks. Baryons, of which the nucleons are two examples, are made up of three quarks whereas mesons, such as pions, consist of a quark and an anti-quark. All hadrons, particles which are affected by the strong force, are thought to be combinations of three quarks, three anti-quarks or a quark with an anti-quark. The hadron spectrum can be accounted for by six flavors of quarks, which are listed in table A.1 with their quantum numbers.

Quarks can be created in quark-anti-quark pairs of the same flavour. Flavour is conserved in the strong interaction but not in weak decays which occur on a much longer time-scale. Some mesons and baryons with their quark content are shown in figures A.1 & A.2.

Even after taking into account the spin of the quarks, it would appear that some hadronic states, such as the Δ^{++}, violate the Pauli exclusion principle. This resonance consists of three u quarks and has a spin of $\frac{3}{2}$ so all three quarks appear to be in identical quantum states. This leads to the introduction of a further quantum number which can take on three values for quarks (plus three opposite values for anti-quarks). This quantum number is labelled color and the values have become

Symbol	Name	Mass	Charge	Quantum no.
u	up	300 MeV	$+\frac{2}{3}$	$I_3 = +\frac{1}{2}$
d	down	300 MeV	$-\frac{2}{3}$	$I_3 = -\frac{1}{2}$
s	strange	500 MeV	$-\frac{2}{3}$	S=-1
c	charm	1.2 GeV	$+\frac{2}{3}$	C=+1
b	bottom	4.2 GeV	$-\frac{2}{3}$	B=-1
t	top	170 GeV	$+\frac{2}{3}$	T=+1

Table A.1: The six quark flavours and their approximate constituent masses.

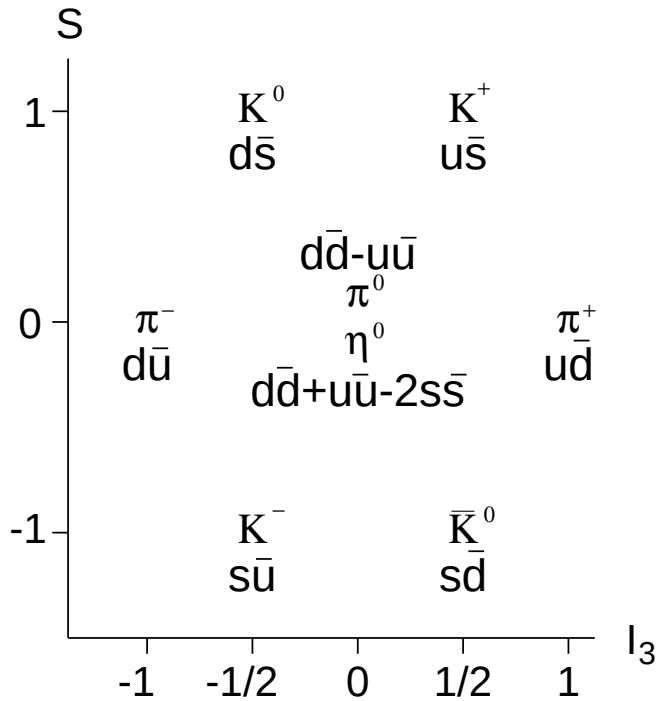

Figure A.1: Meson octet with $J^P = 0^-$

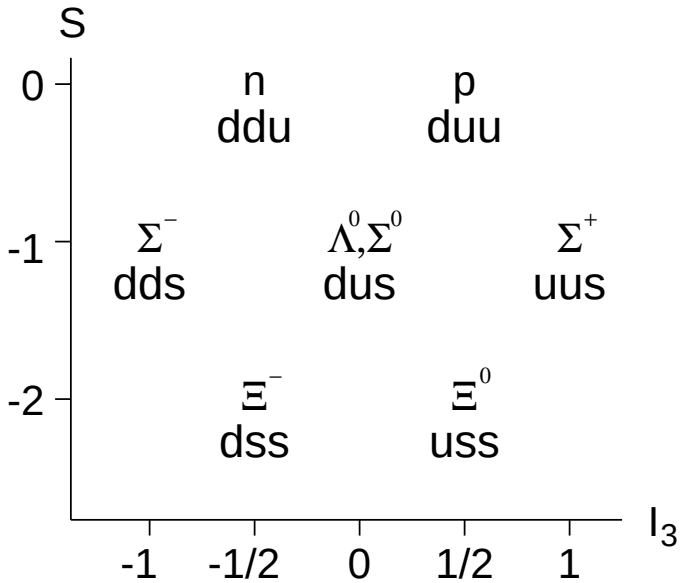

Figure A.2: Baryon octet with $J^P = \frac{1}{2}^+$.

known as red, green and blue. Thus, in the Δ^{++} resonance, the three u quarks each have a different color quantum number. The complete Standard Model also includes the leptons and the bosons which mediate the forces. One of these is the gluon which is exchanged in the strong interaction just as electromagnetic interactions exchange photons. However, unlike the photon, the gluon carries the quanta of the force it is mediating. That is to say gluons have colour charge whereas photons do not possess electromagnetic charge. This property means that the gluons can interact amongst themselves leading to qualitative differences between the strong and electromagnetic forces. There are in fact an octet of gluons carrying the different combinations of the colour charge, $r\bar{b}, r\bar{g}, b\bar{g}, b\bar{r}, g\bar{b}, g\bar{r}$ and the mixtures $(r\bar{r} - g\bar{g})/\sqrt{2}$, and $(r\bar{r} + g\bar{g} - 2b\bar{b})/\sqrt{6}$. This scheme allows a quark of any colour to interact with another by exchanging the appropriate gluon.

Appendix B

The QCD Theory

Quantum Chromodynamics (QCD) describes all phenomena related to strongly interacting particles. QCD can be constructed in analogy to the Quantum Electrodynamics (QED), except for a more complicated gauge group, SU(3) instead of U(1). The standard QCD Lagrangian density reads

$$\mathcal{L} = -\tfrac{1}{4}F^{\alpha}_{\mu\nu}F^{\mu\nu}_{\alpha} - \sum_n \bar{\psi}_n\gamma^{\mu}[\partial_{\mu} - igA^{\alpha}_{\mu}t_{\alpha}]\psi_n - \sum_n m_n\bar{\psi}_n\psi_n \tag{B.1}$$

and it is composed almost of the same elements as the QED Lagrangian density

$$\mathcal{L} = -\tfrac{1}{4}F_{\mu\nu}F^{\mu\nu} - \bar{\psi}_e\gamma^{\mu}[\partial_{\mu} + ieA_{\mu}]\psi_e - m_e\bar{\psi}_e\psi_e. \tag{B.2}$$

Eqs. B.1 and B.2 are expressed within the relativistic formalism that uses space-time four-coordinates numbered by indices μ, ν=0,1,2,3. Moreover, we assume that each pair of repeated indices implies summation over them. The new object in Eq. B.1 is the set of eight SU(3) 3×3 matrices t_{α}, numbered by the gluon-color index α=1,...,8. They fulfill the SU(3) commutation relations

$$[t_{\beta}, t_{\gamma}] = iC^{\alpha}_{\beta\gamma}t_{\alpha} \tag{B.3}$$

where $C^{\alpha}_{\beta\gamma}$ are the SU(3) algebra structure constants. Quarks and gluons are numbered by the indices of the corresponding SU(3) representations: three-dimensional spinor representation for quarks, and eight-dimensional vector representation for gluons.

Dirac four-spinors ψ_n correspond to quark fields. Compared to the electron four-spinors ψ_e in Eq. B.2, they are richer in two aspects. First, each of them appears in three variants, red, blue, and green. These colors are numbered by the quark-color index corresponding to the dimensions 3×3 of the t_{α} matrices. Second, there is not one, but six different quark fields, for n=1,...,6, corresponding to quark flavors.

The first term in the QCD Lagrangian density describes the free gluon fields defined by eight four-potentials A^{α}_{μ}. Instead of one photon of the QED, that transmits the electromagnetic interaction, we have eight gluons that transmit the strong interaction. The gluon field tensors $F^{\alpha}_{\mu\nu}$ are defined as

$$F^{\alpha}_{\mu\nu} = \partial_{\mu} A^{\alpha}_{\nu} - \partial_{\nu} A^{\alpha}_{\mu} + C^{\alpha}_{\beta\gamma} A^{\beta}_{\mu} A^{\gamma}_{\nu}. \tag{B.4}$$

Here comes the really big difference between the QED and QCD, namely, the gluon field tensors contain the third term in Eq. B.4. As a result, gluons interact with one another - they are color-charged, while the photon has no charge.

The last term in Eq. B.1 describes the six free quarks of masses m_n at rest. This does not mean that isolated quarks can exist in nature, be accelerated, and have their masses measured by their inertia with respect to acceleration. Each free quark obeys the Dirac equation just like the electron in QED. The Dirac equation is given by the last term and the ∂_{μ}-term in Eq. B.1.

Quarks couple to gluons through the color currents,

$$J^{\mu}_{\alpha} = -ig \sum_{n} \bar{\psi}_n \gamma^{\mu} A^{\alpha}_{\mu} t_{\alpha} \psi_n. \tag{B.5}$$

Note that all quarks couple to gluons with the same value of the color charge g. The numerical value of this parameter depends on the energy through the mechanism called renormalization.

Consequences of the gluon charges are dramatic. Namely, the force carriers now exert the same force as the force they transmit. Moreover, sources of the electromagnetic field depend on currents

$$J^{\mu} = ie\bar{\psi}_e \gamma^{\mu} \psi_e, \tag{B.6}$$

that involve a small parameter - the electron charge, while gluons constitute sources of the color field without any small parameter. Gluons are not only color-charged, but they also produce very strong color fields.

Let us now consider empty space. In a quantum field theory, we cannot just say that the ground state of the empty space is the state with no quanta - we have to solve the proper field equations,

with proper boundary conditions, and determine what is the state of the field. Such a state may or may not contain quanta. In particular, whenever the space has a boundary, the ground state of the field does contain quanta - this fact is called the vacuum polarization effect.

In QED, this is a very well known, and experimentally verified effect. For example, two conducting parallel plates attract each other, even if they are not charged and placed in otherwise empty space (this is called the Casimir effect). One can understand this attraction very easily. The vacuum fluctuations of the electron field may create in an empty space virtual electron-positron pairs. These charged particles induce virtual polarization charges in the conducting plates (it means virtual photons are created, travel to plates, and reflect from them). Hence, the plates become virtually charged, and attract one another during a short time when the existence of the virtual charges, and virtual photons, is allowed by the Heisenberg principle. All in all, a net attractive force between plates appears.

In QED such effects are extremely weak, because the electron has a small charge and a non-zero rest mass. On the other hand, the QCD gluons are massless, and their strong interaction is not damped by a small parameter. As a result, the QCD vacuum polarization effect is extremely strong, and the empty space is not empty at all - it must contain a soup of spontaneously appearing, interacting, and disappearing gluons. Moreover, in the soup there also must be virtual quark-antiquark pairs that are also color-charged, and emit and absorb more virtual gluons. It turns out that the QCD ground state of an “empty” space is an extremely complicated object. At present, we do not have any glimpse of a possibility to find the vacuum wave function analytically. Some ideas of what happens are provided by the QCD lattice calculations, in which the gluon and quark fields are discretized on a four-dimensional lattice of space-time points, and the differential field equations are transformed into finite-difference equations solvable on a computer.

It is now obvious that one cannot expect other solutions of the QCD fields to be any simpler. In particular, solutions corresponding to isolated quarks simply do not exist. An isolated quark would

create so many gluons around it that the complete wave function can not be normalizable. Solutions for quark-antiquark pairs, and for triples of quarks, do exist, but are even more complicated to obtain, even within the QCD lattice calculations.

Appendix C

Kinematic Variables

In relativistic heavy ion collisions, it is convenient to use kinematic variables that are Lorentz invariant or transform trivially under Lorentz boost.

Given the z axis as the direction of the beam, the p_t (transverse momentum) is defined as:

$$p_t = \sqrt{p_x^2 + p_y^2} \ . \tag{C.1}$$

p_t is a Lorentz invariant variable since both p_x and p_y are unchanged under a Lorentz boost along the z axis.

For identified particles one usually employs the transverse mass

$$m_t = \sqrt{{p_t}^2 + m^2} \ , \tag{C.2}$$

where m is the mass of the particle. The transverse kinetic energy of the particle is given by $m_t - m$.

In place of longitudinal momenta, it is normal to use the rapidity, defined as

$$y = \frac{1}{2} \ln \left(\frac{E + p_z}{E - p_z} \right) \tag{C.3}$$

$$= \ln \left(\frac{E + p_z}{m_t} \right) \tag{C.4}$$

$$= \tanh^{-1} \left(\frac{p_z}{E} \right) \ , \tag{C.5}$$

where E and p_z are the energy and longitudinal momentum of the particle, respectively.

Under a Lorentz transformation from a reference system S to a system S' moving with velocity β_z with respect to S in the longitudinal direction, the rapidity y' in the S' frame is related to y in the S frame only by an additive constant: $y' = y - y_\beta$, where y_β is the rapidity of the moving frame.

$$y_\beta = \frac{1}{2}\ln\left(\frac{1+\beta_z}{1-\beta_z}\right) \quad . \tag{C.6}$$

The additive property of rapidity guarantees that the shape of the corresponding distribution is unchanged under Lorentz boost.

In the limit of $p \gg m$ and $p_z/p \gg 1/\gamma$, the rapidity reduces to

$$y = \frac{1}{2}\ln\left(\frac{E+p_z}{E-p_z}\right) \approx \frac{1}{2}\ln\left(\frac{|\vec{p}|+p_z}{|\vec{p}|-p_z}\right) = \ln\left(\sqrt{\frac{1+\cos\theta}{1-\cos\theta}}\right) = -\ln\left(\tan\theta/2\right) \equiv \eta. \tag{C.7}$$

where η is called pseudorapidity. Note that pseudorapidity, unlike rapidity, can be computed without knowing the mass of the particle.

Appendix D

Author's Contributions to Collaborative Research

In addition to the physics analysis work described in this dissertation, I have completed a number of "community service" tasks within the STAR collaboration, i.e., tasks that are of benefit to part or all of the entire collaboration. I am one of the proposers of the STAR ZDC-SMD, and participated in the construction, testing and installation of the ZDC-SMD. During STAR data-taking in 2004 and 2005, I worked as STAR detector operator and ZDC expert on call. I am responsible for the daily maintenance and calibration of the ZDCs, including their SMDs and forward paddles.

In the area of community service software, I have studied the approach of determining the event vertex from ZDC information, and calibrated the vertex parameters for RHIC run IV (2004). After the installation of the ZDC-SMD, I developed software that uses the pattern of spectator neutrons in the ZDC-SMD to open up multiple new physics opportunities for other members of the STAR collaboration, such as determining the 1st-order event plane, strangelet searching, spin physics, etc. I am among the principal authors of a paper on directed flow in 62.4 GeV AuAu (longer than letter-length, and published by Physical Review C), and another paper on strangelet searching (submitted to Physical Review Letters).

In my early studies, I have carried out a systematic study on the influence of momentum resolution on elliptic flow. The result was incorporated into a long paper recently published in Physical Review C. [57]

I have presented an invited talk on this work at the *School of Collective Dynamics in High-Energy Collisions* (Lawrence Berkeley National Laboratory, May 2005), and at the premier conference in my field — Quark Matter 2005 (QM05) in Budapest, Hungary (August 2005). My QM05 abstract was among the $\sim$ 20% selected for oral presentation, and I am the sole listed author of the

associated paper in the proceedings of QM05. I have also presented a talk at the Annual Meeting of the Division of Nuclear Physics of the American Physical Society in Chicago, IL (October 2004).

My list of publications can be found in Appendix E. STAR policy, following the normal practice of large collaborations in High Energy and Nuclear Physics, lists all authors on refereed publications strictly in alphabetical order. I am among the principal authors for papers marked with “*”.

Appendix E

List of Publications

- **Directed flow in Au+Au collisions at* $\sqrt{s_{NN}} = 62.4$ GeV,

  J. Adams *et al.* (STAR Collaboration), Phys. Rev. C. **73** 034903 (2006).

- **Anisotropic flow in AuAu and CuCu at* 62 GeV *and* 200 GeV,

  Gang Wang (for STAR Collaboration), Quark Matter Meeting 2005 proceedings, accepted by Nucl. Phys. A.

  e-print nucl-ex/0510034 (2005).

- **Strangelet search at RHIC,*

  J. Adams *et al.* (STAR Collaboration), submitted to Phys. Rev. Lett.

  e-print nucl-ex/0511047 (2005).

- **Azimuthal anisotropy in Au+Au collisions at* $\sqrt{s_{NN}} = 200$ GeV,

  J. Adams *et al.* (STAR Collaboration), Phys. Rev. C **72** 014904 (2005).

- *Incident energy dependence of* p_t *correlations at RHIC,*

  J. Adams *et al.* (STAR Collaboration), Phys. Rev. C **72** 044902 (2005).

- *Multi-strange baryon elliptic flow in Au+Au collisions at* $\sqrt{s_{NN}} = 200$ GeV,

  J. Adams *et al.* (STAR Collaboration), Phys. Rev. Lett. **95** 122301 (2005).

- *Multiplicity and pseudorapidity distribution of photons in Au+Au collisions at* $\sqrt{s_{NN}} = 62.4$ GeV,

  J. Adams *et al.* (STAR Collaboration), Phys. Rev. Lett. **95** 062301 (2005).

- *Distributions of charged hadrons associated with high transverse momentum particles in pp and Au+Au collisions at* $\sqrt{s_{NN}} = 200$ GeV,

  J. Adams *et al.* (STAR Collaboration), Phys. Rev. Lett. **95** 152301 (2005).

- *Experimental and theoretical challenges in the search for the Quark Gluon Plasma: the STAR Collaboration's critical assessment of the evidence from RHIC collisions,*

  J. Adams *et al.* (STAR Collaboration), Nucl. Phys. A **757** 102 (2005).

- *K(892)* resonance production in Au+Au and p+p collisions at* $\sqrt{s_{NN}} = 200$ GeV *at STAR,*

  J. Adams *et al.* (STAR Collaboration), Phys. Rev. C **71** 064902 (2005).

- *Azimuthal anisotropy in Au+Au collisions at* $\sqrt{s_{NN}} = 200$ GeV,

  J. Adams *et al.* (STAR Collaboration), Phys. Rev. C **72** 014904 (2005).

- *Transverse-momentum dependent modification of dynamic texture in central Au+Au collisions at at* $\sqrt{s_{NN}} = 200$ GeV,

  J. Adams *et al.* (STAR Collaboration), Phys. Rev. C **71** 031901(R) (2005).

- *Phi meson production in Au+Au and p+p collisions at* $\sqrt{s_{NN}} = 200$ GeV,

  J. Adams *et al.* (STAR Collaboration), Phys. Lett. B **612** 181 (2005).

- *Pion, kaon, proton and anti-proton transverse momentum distributions from p+p and d+Au collisions at* $\sqrt{s_{NN}} = 200$ GeV,

  J. Adams *et al.* (STAR Collaboration), Phys. Lett. B **616** 8 (2005).

- *Event-wise mean-*p_t *fluctuations in Au-Au collisions at* $\sqrt{s_{NN}} = 130$ GeV,

  J. Adams *et al.* (STAR Collaboration), Phys. Rev. C **71** 064906 (2005).

- *Net charge fluctuations in Au+Au collisions at* $\sqrt{s_{NN}} = 130$ GeV,

  J. Adams *et al.* (STAR Collaboration), Phys. Rev. C **68** 044905 (2005).

- *Pion interferometry in Au+Au collisions at* $\sqrt{s_{NN}} = 200\ \mathrm{GeV}$,

  J. Adams *et al.* (STAR Collaboration), Phys. Rev. C **71** 044906 (2004).

- *Azimuthal anisotropy and correlations at large transverse momenta in p+p and Au+Au collisions at* $\sqrt{s_{NN}} = 200\ \mathrm{GeV}$,

  J. Adams *et al.* (STAR Collaboration), Phys. Rev. Lett. **93** 252301 (2004).

- *Pseudorapidity asymmetry and centrality dependence of charged hadron spectra in d+Au collisions at* $\sqrt{s_{NN}} = 200\ \mathrm{GeV}$,

  J. Adams *et al.* (STAR Collaboration), Phys. Rev. C **70** 064907 (2004).

- *Open charm yields in d+Au collisions at* $\sqrt{s_{NN}} = 200\ \mathrm{GeV}$,

  J. Adams *et al.* (STAR Collaboration), Phys. Rev. Lett. **94** 062301 (2004).

- *Measurements of transverse energy distributions in Au+Au collisions at* $\sqrt{s_{NN}} = 200\ \mathrm{GeV}$,

  J. Adams *et al.* (STAR Collaboration), Phys. Rev. C **70** 054907 (2004).

- *Centrality and pseudorapidity dependence of charged hadron production at intermediate* p_t *in Au+Au collisions at* $\sqrt{s_{NN}} = 130\ \mathrm{GeV}$,

  J. Adams *et al.* (STAR Collaboration), Phys. Rev. C **70** 044901 (2004).

- *Production of e+e- pairs accompanied by nuclear dissociation in ultra-peripheral heavy ion collision*,

  J. Adams *et al.* (STAR Collaboration), Phys. Rev. C **70** 031902(R) (2004).

- *Photon and neutral pion production in Au+Au collisions at* $\sqrt{s_{NN}} = 130\ \mathrm{GeV}$,

  J. Adams *et al.* (STAR Collaboration), Phys. Rev. C **70** 044902 (2004).

- *Azimuthally sensitive HBT in Au+Au collisions at* $\sqrt{s_{NN}} = 200\ \mathrm{GeV}$,

  J. Adams *et al.* (STAR Collaboration), Phys. Rev. Lett. **93** 012301 (2004).

- *Azimuthal anisotropy at the Relativistic Heavy Ion Collider: the first and fourth harmonics,*
  J. Adams *et al.* (STAR Collaboration), Phys. Rev. Lett. **92** 062301 (2004).

- *Cross sections and transverse single-spin asymmetries in forward neutral pion production from proton collisions at* $\sqrt{s_{NN}} = 200\ \mathrm{GeV}$,
  J. Adams *et al.* (STAR Collaboration), Phys. Rev. Lett. **92** 171801 (2004).

- *Identified particle distributions in pp and Au+Au collisions at* $\sqrt{s_{NN}} = 200\ \mathrm{GeV}$,
  J. Adams *et al.* (STAR Collaboration), Phys. Rev. Lett. **92** 112301 (2004).

- *Multi-strange baryon production in Au-Au collisions at* $\sqrt{s_{NN}} = 130\ \mathrm{GeV}$,
  J. Adams *et al.* (STAR Collaboration), Phys. Rev. Lett. **92** 182301 (2004).

- ρ^0 *production and possible modification in Au+Au and p+p collisions at* $\sqrt{s_{NN}} = 200\ \mathrm{GeV}$,
  J. Adams *et al.* (STAR Collaboration), Phys. Rev. Lett. **92** 092301 (2004).

- *Rapidity and centrality dependence of proton and anti-proton production from Au+Au collisions at* $\sqrt{s_{NN}} = 130\ \mathrm{GeV}$,
  J. Adams *et al.* (STAR Collaboration), Phys. Rev. C **70** 041901 (2004).

- *Particle-type dependence of azimuthal anisotropy and nuclear modification of particle production in Au+Au collisions at* $\sqrt{s_{NN}} = 200\ \mathrm{GeV}$,
  J. Adams *et al.* (STAR Collaboration), Phys. Rev. Lett. **92** 052302 (2004).

- *Pion-kaon correlations in central Au+Au collisions at* $\sqrt{s_{NN}} = 130\ \mathrm{GeV}$,
  J. Adams *et al.* (STAR Collaboration), Phys. Rev. Lett. **91** 262302 (2003).

- *Evidence from d+Au measurements for final-state suppression of high* p_t *hadrons in Au+Au collisions at RHIC,*
  J. Adams *et al.* (STAR Collaboration), Phys. Rev. Lett. **91** 072304 (2003).

- *Transverse momentum and collision energy dependence of high p_t hadron suppression in Au+Au collisions at ultrarelativistic energies*,

  J. Adams *et al.* (STAR Collaboration), Phys. Rev. Lett. **91** 172302 (2003).

Appendix F

The STAR Collaboration

J. Adams,[3] M.M. Aggarwal,[29] Z. Ahammed,[44] J. Amonett,[20] B.D. Anderson,[20] D. Arkhipkin,[13] G.S. Averichev,[12] S.K. Badyal,[19] Y. Bai,[27] J. Balewski,[17] O. Barannikova,[32] L.S. Barnby,[3] J. Baudot,[18] S. Bekele,[28] V.V. Belaga,[12] A. Bellingeri-Laurikainen,[39] R. Bellwied,[47] J. Berger,[14] B.I. Bezverkhny,[49] S. Bharadwaj,[34] A. Bhasin,[19] A.K. Bhati,[29] V.S. Bhatia,[29] H. Bichsel,[46] J. Bielcik,[49] J. Bielcikova,[49] A. Billmeier,[47] L.C. Bland,[4] C.O. Blyth,[3] S-L. Blyth,[21] B.E. Bonner,[35] M. Botje,[27] A. Boucham,[39] J. Bouchet,[39] A.V. Brandin,[25] A. Bravar,[4] M. Bystersky,[11] R.V. Cadman,[1] X.Z. Cai,[38] H. Caines,[49] M. Calderón de la Barca Sánchez,[17] J. Castillo,[21] O. Catu,[49] D. Cebra,[7] Z. Chajecki,[28] P. Chaloupka,[11] S. Chattopadhyay,[44] H.F. Chen,[37] J.H. Chen,[38] Y. Chen,[8] J. Cheng,[42] M. Cherney,[10] A. Chikanian,[49] H.A. Choi,[33] W. Christie,[4] J.P. Coffin,[18] T.M. Cormier,[47] M.R. Cosentino,[36] J.G. Cramer,[46] H.J. Crawford,[6] D. Das,[44] S. Das,[44] M. Daugherity,[41] M.M. de Moura,[36] T.G. Dedovich,[12] M. DePhillips,[4] A.A. Derevschikov,[31] L. Didenko,[4] T. Dietel,[14] S.M. Dogra,[19] W.J. Dong,[8] X. Dong,[37] J.E. Draper,[7] F. Du,[49] A.K. Dubey,[15] V.B. Dunin,[12] J.C. Dunlop,[4] M.R. Dutta Mazumdar,[44] V. Eckardt,[23] W.R. Edwards,[21] L.G. Efimov,[12] V. Emelianov,[25] J. Engelage,[6] G. Eppley,[35] B. Erazmus,[39] M. Estienne,[39] P. Fachini,[4] J. Faivre,[18] R. Fatemi,[22] J. Fedorisin,[12] K. Filimonov,[21] P. Filip,[11] E. Finch,[49] V. Fine,[4] Y. Fisyak,[4] K.S.F. Fornazier,[36] J. Fu,[42] C.A. Gagliardi,[40] L. Gaillard,[3] J. Gans,[49] M.S. Ganti,[44] F. Geurts,[35] V. Ghazikhanian,[8] P. Ghosh,[44] J.E. Gonzalez,[8] H. Gos,[45] O. Grachov,[47] O. Grebenyuk,[27] D. Grosnick,[43] S.M. Guertin,[8] Y. Guo,[47] A. Gupta,[19] N. Gupta,[19] T.D. Gutierrez,[7] T.J. Hallman,[4] A. Hamed,[47] D. Hardtke,[21] J.W. Harris,[49] M. Heinz,[2] T.W. Henry,[40] S. Hepplemann,[30] B. Hippolyte,[18] A. Hirsch,[32] E. Hjort,[21] G.W. Hoffmann,[41] M.J. Horner,[21] H.Z. Huang,[8] S.L. Huang,[37] E.W. Hughes,[5] T.J. Humanic,[28] G. Igo,[8] A. Ishihara,[41] P. Jacobs,[21] W.W. Jacobs,[17] M Jedynak,[45] H. Jiang,[8] P.G. Jones,[3] E.G. Judd,[6] S. Kabana,[2] K. Kang,[42] M. Kaplan,[9] D. Keane,[20] A. Kechechyan,[12] V.Yu. Khodyrev,[31] B.C. Kim,[33] J. Kiryluk,[22] A. Kisiel,[45] E.M. Kislov,[12] J. Klay,[21] S.R. Klein,[21] D.D. Koetke,[43] T. Kollegger,[14] M. Kopytine,[20] L. Kotchenda,[25] K.L. Kowalik,[21] M. Kramer,[26] P. Kravtsov,[25] V.I. Kravtsov,[31] K. Krueger,[1] C. Kuhn,[18] A.I. Kulikov,[12] A. Kumar,[29] R.Kh. Kutuev,[13] A.A. Kuznetsov,[12] M.A.C. Lamont,[49] J.M. Landgraf,[4] S. Lange,[14] F. Laue,[4] J. Lauret,[4] A. Lebedev,[4] R. Lednicky,[12] C-H. Lee,[33] S. Lehocka,[12] M.J. LeVine,[4] C. Li,[37] Q. Li,[47] Y. Li,[42] G. Lin,[49] S.J. Lindenbaum,[26] M.A. Lisa,[28] F. Liu,[48] H. Liu,[37] J. Liu,[35] L. Liu,[48] Q.J. Liu,[46] Z. Liu,[48] T. Ljubicic,[4] W.J. Llope,[35] H. Long,[8] R.S. Longacre,[4] M. Lopez-Noriega,[28] W.A. Love,[4] Y. Lu,[48] T. Ludlam,[4] D. Lynn,[4] G.L. Ma,[38] J.G. Ma,[8] Y.G. Ma,[38] D. Magestro,[28] S. Mahajan,[19] D.P. Mahapatra,[15] R. Majka,[49] L.K. Mangotra,[19] R. Manweiler,[43] S. Margetis,[20] C. Markert,[20] L. Martin,[39] J.N. Marx,[21] H.S. Matis,[21] Yu.A. Matulenko,[31] C.J. McClain,[1] T.S. McShane,[10] F. Meissner,[21] Yu. Melnick,[31] A. Meschanin,[31] M.L. Miller,[22] N.G. Minaev,[31] C. Mironov,[20] A. Mischke,[27] D.K. Mishra,[15] J. Mitchell,[35] B. Mohanty,[44] L. Molnar,[32] C.F. Moore,[41] D.A. Morozov,[31] M.G. Munhoz,[36] B.K. Nandi,[44] S.K. Nayak,[19] T.K. Nayak,[44] J.M. Nelson,[3] P.K. Netrakanti,[44] V.A. Nikitin,[13] L.V. Nogach,[31] S.B. Nurushev,[31] G. Odyniec,[21] A. Ogawa,[4] V. Okorokov,[25] M. Oldenburg,[21] D. Olson,[21] S.K. Pal,[44] Y. Panebratsev,[12] S.Y. Panitkin,[4] A.I. Pavlinov,[47] T. Pawlak,[45] T. Peitzmann,[27] V. Perevoztchikov,[4] C. Perkins,[6] W. Peryt,[45] V.A. Petrov,[47] S.C. Phatak,[15] R. Picha,[7] M. Planinic,[50] J. Pluta,[45] N. Porile,[32] J. Porter,[46] A.M. Poskanzer,[21] M. Potekhin,[4] E. Potrebenikova,[12] B.V.K.S. Potukuchi,[19] D. Prindle,[46] C. Pruneau,[47] J. Putschke,[21] G. Rakness,[30] R. Raniwala,[34] S. Raniwala,[34] O. Ravel,[39] R.L. Ray,[41] S.V. Razin,[12] D. Reichhold,[32] J.G. Reid,[46] J. Reinnarth,[39] G. Renault,[39] F. Retiere,[21] A. Ridiger,[25] H.G. Ritter,[21] J.B. Roberts,[35] O.V. Rogachevskiy,[12] J.L. Romero,[7] A. Rose,[21] C. Roy,[39] L. Ruan,[37] M.J. Russcher,[27] R. Sahoo,[15] I. Sakrejda,[21] S. Salur,[49] J. Sandweiss,[49] M. Sarsour,[40] I. Savin,[13] P.S. Sazhin,[12] J. Schambach,[41] R.P. Scharenberg,[32] N. Schmitz,[23] K. Schweda,[21] J. Seger,[10] I. Selyuzhenkov,[47] P. Seyboth,[23] E. Shahaliev,[12] M. Shao,[37] W. Shao,[5] M. Sharma,[29] W.Q. Shen,[38] K.E. Shestermanov,[31] S.S. Shimanskiy,[12] E Sichtermann,[21] F. Simon,[22] R.N. Singaraju,[44] N. Smirnov,[49] R. Snellings,[27] G. Sood,[43] P. Sorensen,[21] J. Sowinski,[17] J. Speltz,[18] H.M. Spinka,[1] B. Srivastava,[32] A. Stadnik,[12] T.D.S. Stanislaus,[43] R. Stock,[14] A. Stolpovsky,[47] M. Strikhanov,[25] B. Stringfellow,[32] A.A.P. Suaide,[36] E. Sugarbaker,[28] M. Sumbera,[11] B. Surrow,[22] M. Swanger,[10] T.J.M. Symons,[21] A. Szanto de Toledo,[36] A. Tai,[8] J. Takahashi,[36] A.H. Tang,[27] T. Tarnowsky,[32] D. Thein,[8] J.H. Thomas,[21] A.R. Timmins,[3] S. Timoshenko,[25] M. Tokarev,[12] T.A. Trainor,[46] S. Trentalange,[8] R.E. Tribble,[40] O.D. Tsai,[8] J. Ulery,[32] T. Ullrich,[4] D.G. Underwood,[1] G. Van Buren,[4] N. van der Kolk,[27] M. van Leeuwen,[21] A.M. Vander Molen,[24] R. Varma,[16] I.M. Vasilevski,[13] A.N. Vasiliev,[31] R. Vernet,[18] S.E. Vigdor,[17] Y.P. Viyogi,[44] S. Vokal,[12] S.A. Voloshin,[47] W.T. Waggoner,[10] F. Wang,[32] G. Wang,[20] G. Wang,[5] X.L. Wang,[37] Y. Wang,[41] Y. Wang,[42] Z.M. Wang,[37] H. Ward,[41] J.W. Watson,[20] J.C. Webb,[17] G.D. Westfall,[24] A. Wetzler,[21] C. Whitten Jr.,[8] H. Wieman,[21] S.W. Wissink,[17] R. Witt,[2] J. Wood,[8] J. Wu,[37] N. Xu,[21] Z. Xu,[4] Z.Z. Xu,[37] E. Yamamoto,[21] P. Yepes,[35] I-K. Yoo,[33] V.I. Yurevich,[12] I. Zborovsky,[11] H. Zhang,[4] W.M. Zhang,[20]

Y. Zhang,[37] Z.P. Zhang,[37] C. Zhong,[38] R. Zoulkarneev,[13] Y. Zoulkarneeva,[13] A.N. Zubarev,[12] and J.X. Zuo[38]
(STAR Collaboration)

[1] *Argonne National Laboratory, Argonne, Illinois 60439*
[2] *University of Bern, 3012 Bern, Switzerland*
[3] *University of Birmingham, Birmingham, United Kingdom*
[4] *Brookhaven National Laboratory, Upton, New York 11973*
[5] *California Institute of Technology, Pasadena, California 91125*
[6] *University of California, Berkeley, California 94720*
[7] *University of California, Davis, California 95616*
[8] *University of California, Los Angeles, California 90095*
[9] *Carnegie Mellon University, Pittsburgh, Pennsylvania 15213*
[10] *Creighton University, Omaha, Nebraska 68178*
[11] *Nuclear Physics Institute AS CR, 250 68 Řež/Prague, Czech Republic*
[12] *Laboratory for High Energy (JINR), Dubna, Russia*
[13] *Particle Physics Laboratory (JINR), Dubna, Russia*
[14] *University of Frankfurt, Frankfurt, Germany*
[15] *Institute of Physics, Bhubaneswar 751005, India*
[16] *Indian Institute of Technology, Mumbai, India*
[17] *Indiana University, Bloomington, Indiana 47408*
[18] *Institut de Recherches Subatomiques, Strasbourg, France*
[19] *University of Jammu, Jammu 180001, India*
[20] *Kent State University, Kent, Ohio 44242*
[21] *Lawrence Berkeley National Laboratory, Berkeley, California 94720*
[22] *Massachusetts Institute of Technology, Cambridge, MA 02139-4307*
[23] *Max-Planck-Institut für Physik, Munich, Germany*
[24] *Michigan State University, East Lansing, Michigan 48824*
[25] *Moscow Engineering Physics Institute, Moscow Russia*
[26] *City College of New York, New York City, New York 10031*
[27] *NIKHEF and Utrecht University, Amsterdam, The Netherlands*
[28] *Ohio State University, Columbus, Ohio 43210*
[29] *Panjab University, Chandigarh 160014, India*
[30] *Pennsylvania State University, University Park, Pennsylvania 16802*
[31] *Institute of High Energy Physics, Protvino, Russia*
[32] *Purdue University, West Lafayette, Indiana 47907*
[33] *Pusan National University, Pusan, Republic of Korea*
[34] *University of Rajasthan, Jaipur 302004, India*
[35] *Rice University, Houston, Texas 77251*
[36] *Universidade de Sao Paulo, Sao Paulo, Brazil*
[37] *University of Science & Technology of China, Anhui 230027, China*
[38] *Shanghai Institute of Applied Physics, Shanghai 201800, China*
[39] *SUBATECH, Nantes, France*
[40] *Texas A&M University, College Station, Texas 77843*
[41] *University of Texas, Austin, Texas 78712*
[42] *Tsinghua University, Beijing 100084, China*
[43] *Valparaiso University, Valparaiso, Indiana 46383*
[44] *Variable Energy Cyclotron Centre, Kolkata 700064, India*
[45] *Warsaw University of Technology, Warsaw, Poland*
[46] *University of Washington, Seattle, Washington 98195*
[47] *Wayne State University, Detroit, Michigan 48201*
[48] *Institute of Particle Physics, CCNU (HZNU), Wuhan 430079, China*
[49] *Yale University, New Haven, Connecticut 06520*
[50] *University of Zagreb, Zagreb, HR-10002, Croatia*